Marie Skłodowska Curie Action

SCAVENGE

Sustainable Cellular Network Harvesting Ambient Energy

H2020-MSCA-ITN-ETN

Grant Agreement Number: 675891

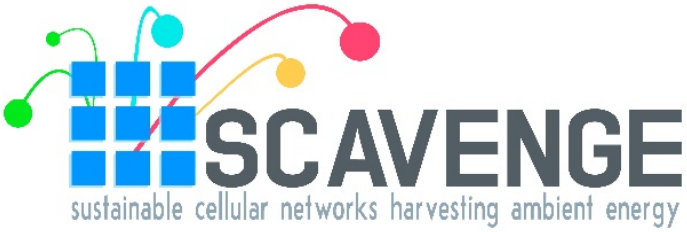

WP2–Energy Models

D2.1–Intermediate Report

Contractual Delivery Date:	January 31, 2018
Actual Delivery Date:	January 30, 2018
Responsible Beneficiary:	CEA
Contributing Beneficiaries:	All
Dissemination Level:	Public
Version:	Draft

Document Information

Document ID:	WP2/D2.1
Version Date:	January 30, 2018
Total Number of Pages:	130
Abstract:	With ICTs forecast to represent more than 50% of the world energy consumption and more than 20% of the humanity carbon footprint by 2030, the inclusion of renewable energy within mobile communication networks is a necessary step against global warming. SCAVENGE project is addressing this issue by proposing a sustainable paradigm for 5G mobile networks, where infrastructures and end-devices are powered with locally harvested energy resources. In the framework of Work Package 2, this document is dedicated to describe the main energy harvesting sources and the storage technologies used in real-life systems, with corresponding models from the literature. Moreover, in order to select the best technology for each network element, the principal energy consuming parts are described while modelling the consumption with respect to relevant network parameters. The report presents mainly a state-of-the-art survey on these topics and gives some perspectives for next period. The work is achieved by all the Early Stage Researchers (ERSs) in SCAVENGE project.
Keywords:	Energy harvesting sources, Energy Harvesting Models, Energy harvesting storage, Power consumption models, 5G networks, Mobile devices, IoT devices, Base stations, sensors

Authors

Full name	**Beneficiary/ Organisation**	**e-mail**	**Role**
Mireille Sarkiss	CEA	mireille.sarkiss@cea.fr	Editor
Ibrahim Fawaz	CEA	ibrahim.fawaz@cea.fr	Editor, Contributor
Filipe Conceicao	CEA	filipe.conceicao@cea.fr	Contributor
Hoang Duy Trinh	CTTC	hdtrinh@cttc.es	Contributor
Dagnachew Temesgene	CTTC	dagnachew.temesgene@cttc.es	Contributor
Nicola Piovesan	CTTC	nicola.piovesan@cttc.es	Contributor
Angel Fernandez Gambin	UniPD	afgambin@dei.unipd.it	Contributor
Elvina Gindullina	UniPD	elvina.gindullina@dei.unipd.it	Contributor
Mehmet Emre Ozfatura	Imperial	m.ozfatura@imperial.ac.uk	Contributor
Nitish Mital	Imperial	n.mital@imperial.ac.uk	Contributor
Vianney Anis	USTRATH	vianney.anis@strath.ac.uk	Editor, Contributor
Thembelihle Dlamini	ATH	thembelihle.dlamini@athonet.com	Contributor
Ioana Suciu	WoS	isuciu@worldsensing.com	Contributor
Soheil Rostami	HWFI	soheil.rostami1@huawei.com	Contributor

Reviewers

Full name	Beneficiary/ Organisation	e-mail	Date
Leonardo Badia	UniPD	leonardo.badia@dei.unipd.it	15/01/2018
Stephan Weiss	USTRATH	stephan.weiss@strath.ac.uk	15/01/2018
Filippo Tosato	TREL	filippo.tosato@toshiba-trel.com	15/01/2018

Version history

Version	Date	Comments
1.0	31/01/2018	

Executive Summary

Information and communication technologies (ICTs) penetrate all parts of the society, where statistics shows an average of 6.8 billion of mobile subscribers and 750 million households connected to the Internet [1]. With ICTs contributing for 10% of the worldwide electricity consumption and forecast to represent more than 50% of the world energy consumption corresponding to 23% of the humanity carbon footprint by 2030, the inclusion of renewable energy within communication network is a necessary step against global warming.

This document presents the work achieved by all ESRs during the first two years of SCAVENGE project in the framework of WP2 on Energy models. The report provides a literature review on the integration of energy harvesting within wireless communication networks. In order to properly design and manage the devices in an energy harvesting communication network, we require both knowledge about the technologies and devices as well as ways to model the power harvesting, storage and consumption of these devices.

In Chapter 2, we identify several harvestable energies, such as solar and wind, but also vibration, heat and electromagnetic radiation (widely present in wireless communications environments). To each of those energies, we associate several harvesting technologies, and extract models for each type of energy and harvester from the literature. Where it is covered in the literature, we also highlight applications and constraints in communication networks.

The intermittent characteristics of most renewable energies make their storage necessary. Therefore in Chapter 3, we describe multiple storage technologies that come with the variety of devices in the networks. We consider three families of storage technologies: mechanical such as flywheel and compressed air, electrical with the description of different types of capacitors, electro-chemical considering both standard batteries and other, often more recent technologies such as flow batteries.

With the introduction of renewable energy in the power supply of communication networks, the understanding of how the power is consumed in such networks becomes critical. Chapter 4 proposes to decompose the network into four device groups: the base stations, the core-network, the mobiles devices, the IoT devices, or sensor nodes.

The document overviews and analyses the various modelling techniques to acquire a better understanding of the design and modelling of an energy harvesting communication network. At this point of our research, we only give a state-of-the-art survey and do not present any new model or full model for SCAVENGE communication networks. However, we believe we possess all the necessary elements to model most of the scenarios that SCAVENGE will explore. We also provide in this report some insights for investigating new models in future work. These models will enable the integration of energy harvesting capabilities in communication networks by accounting for different characteristics and features rarely present in the literature, such as for instance, caching techniques at base stations, virtualised computing platforms in the core network and security measures at IoT devices.

Table of Contents

List of Figures

List of Acronyms and Abbreviations

3G Third Generation Cellular Network

3GPP Third Generation Partnership Project

AC Alternating Current

ADC Analog to Digital Converter

AFC Alkaline Fuel Cell

ANN Artificial Neural Network

BBU Baseband processing Unit

BS Base Station

BT Bluetooth

Btu/lb British thermal units per pound

CA Compressed Air

CM Cache Miss

CN Core Network

CPU Central Processing Unit

CPV Concentrated Photovoltaics

CS Cryogenic System

CSP Concentrated Solar Power

CU Control Unit

DAC Digital to Analog Converter

DC Direct Current

DCH Dedicated Channel

DL Downlink

DOD Depth of Discharge

DOF Degree of Freedom

DP Dynamic Programming

DPP Determinantal Point Process

DSLAM Digital Subscriber Line Access Multiplexer

DSP Digital Signal Processor

DSSC Dye-Sensitized Solar Cell

EDLC Electric Double-Layer Capacitors

EPC Evolved Packet Core

EM Electromagnetic

EMF Electromotive Force

ESI Energy State Information

E-UTRAN Evolved Terrestrial Radio Access Network

FE Finite Element

FESS Flywheel Energy Storage Systems

FPGA Field-Programmable Gate Array

fps Frames per Second

FS Fibre Switches

GCV Higher Heating Value

GES Gigabit Ethernet Switch

GPRS General Packet Radio Service

GPS Global Positioning System

GPU Graphics Processing Unit

GSM Global System for Mobile Communications

HAWT HAWTHorizontal Axis Wind Turbine

HCN HCNHeterogeneous Cellular Networks

HHV Higher Heating Value

HSS Home Subscriber Server

ICT Information and Communication Technology

IEC International Electrotechnical Commission

IF Intermediate Frequency

IoT Internet of Things

IO Input Ouput

IP Internet Protocol

ISM The Industrial, Scientific and Medical

IT Information Technology

KPIs Key Performance Indicators

LHV Lower Heating Value

LIB Lithium-ion Batteries

LIC Lithium-ion Capacitor

LO Local Oscillator

LTE Long Term Evolution

MCFC Molten Carbonate Fuel Cell

MEC Mobile Edge Computing

MEMS Micro-Electro-Mechanical Systems

MJ Multi-Junction

MME Mobility Management Entity

MN Mobile Networks

MTU Maximum Transmission Unit

MW Mega Watts

NaS Sodium Sulphur

NAS Non-Access Stratum

NCV Lower Heating Value

NFC Near Field Communication

NFs Network Functions

NFV Network Function Virtualisation

NIC Network Interface Card

NiCd Nickel Cadmium

NiMH Nickel Metal Hydride

OCV Open Circuit Voltage

OS Operating System

OTC One Time Constant

PA Power Amplifier

PAFC Phosphoric Acid Fuel Cell

PAPR Peak-to-Average-Power-Ratio

PCS Power Conversion System

PCEF Policy Control Enforcement Function

PCH Paging Channel

PCRF Policy and Charging Rules Function

PCS Power Conditioning System

PEFC Polymer Electrolyte Fuel Cell

PGEC Phonon Glass and Electron Crystals

PGW Packet Data Network Gateway

PLMN Public Land Mobile Network

PMU Power Management Unit

PSB Poly-Sulphide Bromide

Pt Platinum

PV Photo-Voltaic

QCI QoS Class Identifier

QoS Quality of Service

RAM Random Access Memory

RAN Radio Access Network

RF Radio Frequency

RFID Radio Frequency IDentification

RPM Revolutions per Minute

RRC Radio Resource Control

RTOS Real-Time Operating System

Ru Ruthenium

Rx Receiver

SC Super-Capacitors

SCM Super-Conductive Magnetic

SD Secure Digital memory card

SFP Small Form-factor Pluggable

SFP+ Enhanced Small Form-factor Pluggable

SGW Serving Gateway

SMES Superconducting Magnetic Energy Storage

SOC State of Charge

SOC System-on-a-Chip

TEG Thermoelectric Generator

TEM Thermoelectric Module

TTC Two Time Constant

Tx Transmitter

UDP User Datagram Protocol

UE User Equipment

UL Uplink

UMTS Universal Mobile Telecommunications System

URA UTRAN Registration Area

USB Universal Serial Bus

UV Ultra-Violet

VAWT VAWTVertical Axis Wind Turbine

VDSL VDSLVery-high-speed Digital Subscriber Line

VEH Vibration Energy Harvester

VM Virtual Machine

VNF Virtualized Network Functions

VR Vanadium Redox

WCDMA Wideband Code Division Multiple Access

WEH Wireless Energy Harvesting

WIFI Wireless Fidelity

WLAN Wireless Local Area Network

WSN Wireless Sensor Network

1. Introduction

Information and communication technologies (ICTs) penetrate all parts of the society, where statistics show an average of 6.8 billion of mobile subscribers and 750 million households connected to the Internet [1]. These unprecedented numbers of connected devices increase the mobile traffic and at the same time, the carbon footprint and the energy requirements of the ICTs. The next generation of mobile technology should be able to support the huge number of devices and reduce the carbon footprint by reducing the energy consumed, while providing good performance in terms of latency and reliability. To this end, SCAVENGE proposes a sustainable paradigm for the next generation 5G mobile networks, where all the network components can harvest renewable energies from the surrounding environment and use it efficiently to meet the performance demands.

The Work Package 2 (WP2) aims at creating a common energy framework to model the characteristics of different types of energy harvesting sources and storage technologies on one hand, and energy consumption of the different network components on the other. WP2 involves all ESRs, as listed in Table 1.1.

Table 1.1: ESRs involved in WP2

ESR	**Full name**	**Beneficiary/ Organisation**	**Main Supervisor**
1	Ibrahim Fawaz	CEA	Mireille Sarkiss
2	Filipe Conceicao	CEA	Nouha Oualha
3	Hoang Duy Trinh	CTTC	Lorenza Giupponi
4	Dagnachew Temesgene	CTTC	Paolo Dini
5	Nicola Piovesan	CTTC	Paolo Dini
6	Angel Fernandez Gambin	UniPD	Michele Rossi
7	Elvina Gindullina	UniPD	Leonardo Badia
8	Mehmet Emre Ozfatura	Imperial	Deniz Gunduz
9	Nitish Mital	Imperial	Cong Ling
10	Vianney Anis	USTRATH	Stephan Weiss
11	Thembelihle Dlamini	ATH	Daniele Munaretto
12	Pavlos Triantaris	TREL	Filippo Tosato
13	Ioana Suciu	WoS	Andrea Bartoli
14	Soheil Rostami	HWFI	Kari Heiska

This Work Package is divided in two tasks:

- Task 2.1 - Energy harvesters and energy storage models: The goal of this task is to analyse suitable sources of energy to power the different network elements, along with appropriate energy storage systems allowing to store the surplus harvested energy for future use. Mathematical models for each type of harvester and storage technology are then surveyed.

- Task 2.2 - Energy consumption models: The goal of this task is to quantify and model the power consumption of each network element.

Following this methodology, this intermediate report provides an overview of the literature on these topics. In particular, Chapter 2 is dedicated to describe harvesters, the technology used to extract energy and the corresponding models found in the literature. Chapter 3 describes different storage technologies along with their respective models. Chapter 4 details the energy consumption for each network element. Finally, Chapter 5 provides some conclusions on the reviewed works and discusses some insights for future proposals in order to cover additional features lacking in the literature and of interest for ESR projects in SCAVENGE.

2. Energy Harvesting Sources

2.1. Introduction

Global warming is one of the biggest threats to the natural world. This is caused primarily by the human use of fossil fuels (oil and coal) to generate electricity, which emits greenhouse gases into the atmosphere and in particular carbon dioxide (CO_2). According to [2], a 2.3% increase in Information and Communication Technology (ICT) global emission is expected by the year 2020. Therefore, in an effort to reduce operational expenses and environmental footprint, pushing for the integration of renewable energy technology to power the communication infrastructure becomes essential.

2.2. Solar

Among the renewable energy sources, solar is the most popular one and is exploited in numerous applications.

2.2.1. Resource

Figure 2.1 [3] shows the distribution of irradiation and thus the availability of solar power across the globe, making the deployment of solar-powered generators, in countries where electric grid is not available, easier and cheaper than conventional sources, reducing thus the dependence on expensive sources like oil. On the other hand, solar power depends on geolocation and weather. The stochastic nature of the latter and thus uncertainty of available energy is a major obstacle to the large-scale use of solar energy in many regions. Besides that, the sunniest areas in many countries do not have the highest demand for electricity [4]. Such geographical mismatches require the use of long transmission lines which are very expensive and difficult to deploy [5].

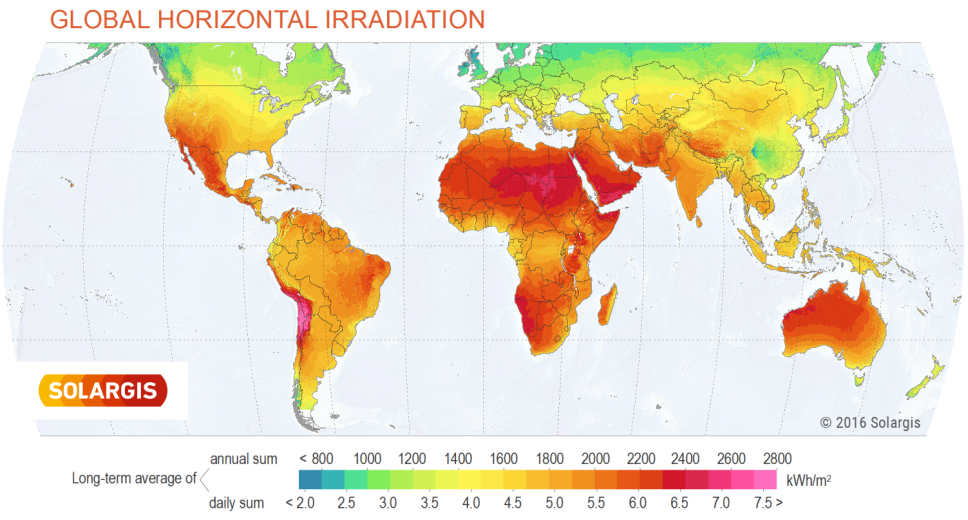

Figure 2.1: Map of average solar irradiation across the globe [3]

2.2.2. Harvesters

Solar energy can be accessed by converting light radiation into electricity through a number of different technologies.

2.2.2.1. Photo-voltaic Technology

Photo-voltaic (PV) technology is the most used worldwide. Figure 2.2 shows an example of PV technology.

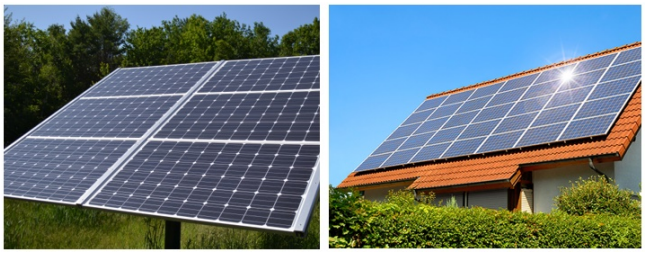

Figure 2.2: Example of PV technology

PV solar cells operate at near ambient temperature with no moving parts and their power efficiency is not affected by scale [5].

2.2.2.1.1 Basics of Solar PV Energy Conversion

A solar PV array consists of one or more electrically connected PV modules, where each module contains many individual cells [6]. Figure 2.3 shows the inside of a PV cell [7].

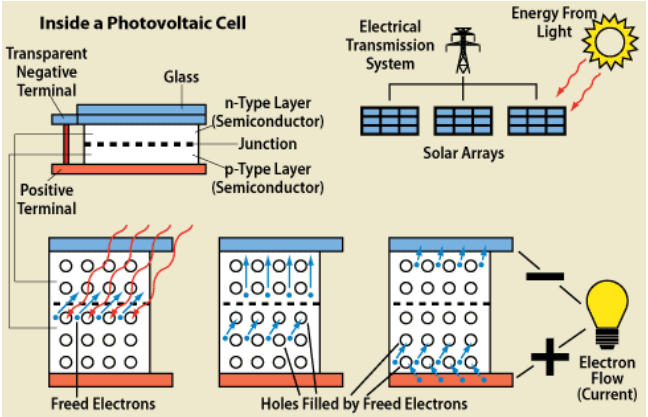

Figure 2.3: Inside a PV cell [7]

When exposed to sunlight, a solar cell connected to an external circuit generates a Direct Current (DC), and using adequate components (combiners, inverters, and transformers), this current can be converted into grid-compatible Alternating Current (AC) if needed. Meanwhile, charge controllers and batteries could be also used to store energy during the day and provide on-demand power during the night.

2.2.2.1.2 PV Technology options

PV solar cells can be divided into two main structures: wafer-based and thin film as shown in Figure 2.4 [8]. Wafer-based cells are made using semiconducting wafers and modules are typically covered with glass for mechanical stability and protection. Thin film cells consist of layers of semiconducting material deposited onto an insulating substrate, such as glass or flexible plastic [8].

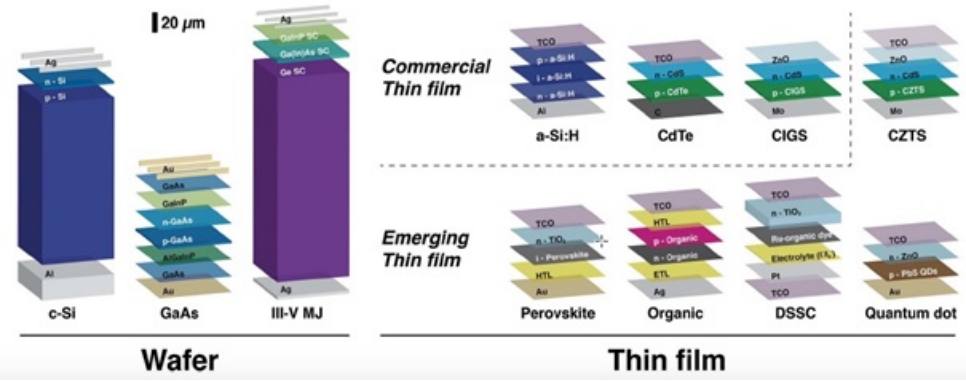

Figure 2.4: PV solar cells structures

2.2.2.2. Concentrated PV Technology

Unlike conventional PV systems, Concentrated Photovoltaic (CPV) technology uses lenses and mirrors to focus sunlight onto small, but highly efficient, multi-junction (MJ) solar cells. Typically, CPV systems can reach more than 35% efficiency, which can be further increased using solar trackers and cooling systems. Trackers are vital to CPV and they need to be extremely precise in how they follow the sun. With a CPV system the alignment of the module towards the sun has to be very accurate, in the range of 0.5 degrees. Tracking accuracy can be affected by temperature changes, wind, condensation, and more subtle events such as ground movement and gradual degradation of mechanical or electrical systems. CPV systems differ in the typology of concentrators, solar cells and cooling modules, which lead to different harvesting capabilities.

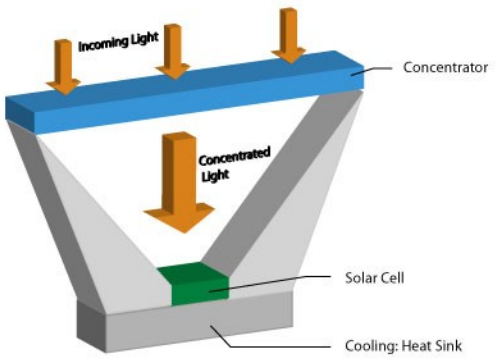

Figure 2.5: Schematic CPV modules with main components

By concentrating sunlight onto a small area, this technology has three competitive advantages:

- requires less photovoltaic material to capture the same amount of solar radiation as non-concentrating PV.
- makes use of highly efficient but expensive multi-junction cells; these are economically viable due to smaller space requirements.
- the optical system comprises standard materials, manufactured in proven processes. Moreover, optics are less expensive than cells.

2.2.2.3. Concentrated Solar Power Technology

Concentrated Solar Power (CSP) is a method to generate electricity from sunlight by converting solar radiation to heat at first and then to electricity [9]. The process involves heating a fluid to create steam capable of driving the turbine of a generator. Due to the involvement of heating, concentrated solar power is also known as solar thermal power.

One of the main engineering challenges in CSP plants is collecting the low density solar radiation. As a result, concentrators are used in these plants. The most widely used concentrators are glass mirrors with high reflectivity. Concentrators can be further classified as point focusing and line focusing [10]. Point focusing systems result in higher temperature (higher concentration factor) than line focusing concentrators but are more complex to handle. For more information on the technical principles behind these concentrators, readers can refer to [10].

The main advantage of CSP plants over PV technology is the relative ease to integrate them with other thermal generation options and high efficiency thermal storage technologies. However, CSPs have limited applications mainly because they exploit only direct solar radiation and are hardly scalable, which results in only reasonable techno-economic feasibility at large scale deployments. In fact, any practically significant CSP plant requires a large land and water resources, thus limiting the available options.

2.2.2.4. Dye Sensitized Solar Cells

Dye-sensitized solar cell (DSSC) is a low-cost technology belonging to the group of thin film solar cells. They present several advantages: they are cheap, simple to make using roll-printing techniques, semi-flexible and semi-transparent. For these reasons, they can be deployed to glass-based systems.

The main characteristic of DSSC is that it collects sunlight by using dye molecules absorbed on a nano-crystalline oxide semiconductor, such as titanium dioxide (TiO_2). These molecules allow to reach high efficiency by absorbing visible light photons. In this way, the light absorption (by dyes) and the charge collection processes (by a semiconductor) are separated, mimicking photosynthesis.

This approach allows to use very cheap wide band-gap oxide semiconductors in the solar cell, reaching much cheaper solar energy at $1 per peak Watt, compared to the today >4$ per peak Watt of crystalline or thin film Silicon solar cells.

The high efficiency of DSSC is primarily due to the employment of porous TiO_2 as the anode material. The advantages of this material are its low costs, high photosensitivity, and high structure stability under solar irradiation and in solution. Since TiO_2 is a wide band-gap semiconductor ($\sim$ 3.2 eV), it only absorbs ultra-violet (UV) light, which comprises only 5% of the solar spectrum. As a solution, dye molecules are employed for visible light capture. Nano-crystalline TiO_2 provides high light capture efficiency with incident photon-to-charge efficiency of 60-90% compared with the <0.13% of the monocrystal form. This fact is due to the high surface-to-volume ratios that can be achieved when dealing with porous nano-crystal materials.

Early DSSC design adopted Ruthenium (Ru) dyes, which are highly effective but also very expensive (>1000$/g). For this reason, new materials have been studied as substitutes. In experiments, organic dyes such as natural pigments (e.g. chlorophyll, carotene, and anthocyanin) have been successfully used to sensitise TiO_2 solar cells to reach good efficiencies and high stability [11]. Synthetic organic dyes are even more promising. They cost one-tenth of Ru dyes and can reach an efficiency of 10% [12], compared to the 11% of Ru dyes [13].

With regard to the electrolyte, currently three different types have been used in DSSC: (i) Iodide/triiodide (I^-/I_3^-) in organic solvents (most common), (ii) inorganic ionic liquids made of salts or salt mixture, and (iii) solid electrolyte.

On the back of DSSC there is a second glass substrate covered with a thin layer of Platinum (Pt) used as catalyst to regenerate I^- and a cathode material. Technically, this is the best material for efficient devices, but due to its high cost, carbon cathode has been considered a valid substitute [14]. Also, polymers have been studied as counter electrode, being inexpensive and non-fragile [15].

2.2.3. Models

When modelling the harvestable solar power a good metric is the average solar radiation arriving at the surface. The monthly radiation must then be multiplied with the solar panel size to get the monthly received radiation. However, only a fraction of the solar radiation can be converted into electrical power for the following reasons:

- each solar panel features a specific efficiency, and a reduction factor must be introduced.
- the radiation angle reduces the harvested energy: while the standard test conditions assume that the solar radiation hits the panel orthogonally, this is unrealistic for real deployments as the sun moves over the day as well as over the year. Hence, the factor that considers the angular deviation from orthogonal radiation must be included.
- if the harvested electric power is passed through a voltage regulator or used for charging a battery, losses will occur here as well.

To maximise the harvesting process, other aspects have to be taken into consideration:

- In most wireless networks, any kind of node typically is capable of operating in power sleep modes. During the sleep phases, it is more likely that the harvested energy will be stored using rechargeable batteries. However, some battery technological aspects, like the operational temperature (for example, lithium-ion batteries can neither be charged below 0 °C nor above 45 °C) need to be considered. As a result, there will be times when solar power is available but cannot be stored resulting in a loss.

- During winter, the sensor node could need more energy than the solar panel can deliver. This deficit can be compensated by energy stored in the battery before. The larger the battery capacity C, the longer the period of insufficient solar power can be sustained.

Many models are used in the literature to describe the solar energy. The most common ones are based on linear and nonlinear models. These models give a correlation between the solar energy on a horizontal surface and some meteorological parameters such as shining hours, ambient temperature and relative humidity. The linear models use simple linear functions while the nonlinear models employ polynomial functions of higher order [16].

2.2.3.1. Linear and non-linear modelling techniques

Solar energy consists of two parts: extraterrestrial solar energy, which is above the atmosphere, and global solar energy, which is under the atmosphere.

2.2.3.1.1 Global solar energy model

The Angstrom model is the most commonly used linear model to describe the solar energy [16–18]:

$$\frac{E_T}{E_{extra}} = a + b\frac{S}{S_0}, \tag{2.1}$$

where E_T is the global solar energy, E_{extra} is the extraterrestrial solar energy, S is the number of shining hours and S_0 is the day length. The parameters models a and b are determined by plotting E_T/E_{extra} versus S/S_0 using real data.
A more accurate model is obtained by adding a nonlinear term to the Angstrom model [16, 19],

$$\frac{E_T}{E_{extra}} = a + b\frac{S}{S_0} + c\left(\frac{S}{S_0}\right)^2. \tag{2.2}$$

2.2.3.1.2 Diffuse solar energy model

The global solar energy incident on a horizontal surface may have direct beam and diffuse components. A linear model describing the relationship between the average daily diffuse and global solar radiation incident on a horizontal surface is given by [16, 19]:

$$\frac{E_d}{E_T} = a + bK_T, \tag{2.3}$$

where E_d is the diffuse solar energy, E_T is the global solar energy, and K_T is the clearness index. The relationship can be extended to a non-linear model:

$$\frac{E_d}{E_T} = a + bK_T + cK_T{}^2 + dK_T{}^3. \tag{2.4}$$

2.2.3.2. Artificial intelligence techniques

In [20–30], an Artificial Neural Network (ANN) is used to estimate the solar radiation based on real-data collected in a specific region.

2.2.3.3. Solar energy model on a tilt surface

The amount of the collected energy by a solar panel is highly affected by its orientation and tilt. Therefore, to maximise the collected solar energy, these two parameters should be adjusted periodically during the day, depending on the surrounding environment. This can be done using an electro-mechanical or purely mechanical device, i.e. active sun tracker. However, the cost of such a device is high and it consumes energy during tracking [16, 19]. An alternative sub-optimal solution is to model the solar energy on a tilt surface in order to find the optimal constant values of the tilt angle and orientation of the solar panel for a specific location.

The components of incident global solar radiation on a tilt surface consider the global, direct (beam), diffuse and reflected solar energy. The solar energy components on a tilt surface are given by:

$$E_{T_{TLT}} = (E_T - E_D)R_B + E_D R_D + \rho ETR_R, \tag{2.5}$$

where R_B is the ratio between global solar energy on a horizontal surface and global solar energy on a tilt surface, R_D is the ratio between diffuse solar energy on a horizontal surface and diffuse solar energy on a tilt surface, R_R is the amount of reflected solar energy on a tilt surface and ρ is ground Aledo. Thus, the key to determine the solar energy components on a tilt surface is to estimate the coefficients R_B, R_D and R_R. These coefficients calculation can be found in [16].

2.2.3.4. Stochastic Markov model for small cells

The work in [31] presents a model to derive accurate stochastic Markov processes for the description of the energy scavenged by PV panels with small form factors, as those exploited by small-cells or embedded devices. The proposed model can be utilised for predicting future energy arrival and the energy consumption that is needed by the system to remain operational when needed. The introduced model has the following parts: Astronomical Model, PV model, Power Processor, and Semi-Markov Model for Stochastic Energy Harvesting. The key building blocks of this model are shown in Figure 2.6.

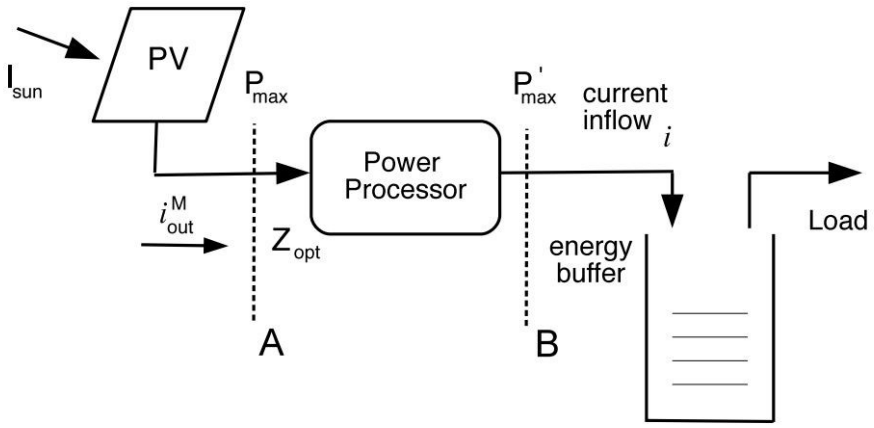

Figure 2.6: The main components of the model [31]

The dynamics of the energy harvested from the environment is captured by a continuous time Markov chain with two states, $x_s(K)$. To model timings, t_k are defined as the time instants when the source transits into a different state. The parameter τ_k is defined as the time elapsed between two subsequent transitions $\tau_k = t_{k+1} - t_k$ with a probability density function of $f(\tau_k|x_s)$. Based on this model, two clustering algorithms are defined: Night-day clustering and Slot-based clustering.

2.2.4. Conclusion

Solar power is proved to be possibly the best-suited source for harvesting energy for outdoor applications. However, the amount of energy that can be scavenged from the sun changes seasonally an daily, and is subject to stochastic influences due to the weather. Consecutively, dimensioning the solar panel is a primary problem regarding this renewable energy process.

The exploitation of solar power has become very attractive in the field of wireless communication, due to the enormous increase in the utilisation of Internet in last few years. For example, in wireless sensor networks, many devices are traditionally powered with primary batteries, which limits their lifetime and leads to high maintenance costs. Adding harvesting capabilities to traditional devices improves the overall energy efficiency of the system but requires a greater attention to dimensioning and modelling the process in Figure 2.6. Therefore, the cost of a solar energy system remains a challenging issue while maintaining reliability and efficiency. Hence, it needs energy storage technologies.

2.3. Thermoelectric

Thermoelectric technology has been used in space missions for a long period by exploiting the radioisotope thermoelectric generator, which converts the heat of the radioactive material into electricity by the Seebeck effects, Peltier effect or Thomson effect [32]. Thermoelectric energy converters are used to convert heat from power plants, factories, motor vehicles, computers or human bodies [33].

2.3.1. Resource

In comparison with other sources of energy, thermoelectric energy source provides relatively low electrical power levels (few dozens of a Watts). Moreover, the main challenge of the thermoelectric power generation is the low heat-to-electricity conversion efficiency, and a number of research efforts have been undertaken to improve the waste heat recovery efficiency, using such heat sources as power plants, automobiles, geothermal energy and other heat-generating industries [33]. In addition, thermoelectric generator (TEG) has many advantages such as no moving parts, no toxic residuals, no chemical reactions, being environmental friendly and deployable in unmaintained situations. These reasons make this source of power attractive in many industrial fields [33], [34].

The effectiveness of the thermoelectric materials is measured by merit (ZT). A high value of ZT requires both a high Seebeck coefficient (a) and high electrical conductivity (σ), while thermal conductivity (K) must be low [35],

$$ZT = (\sigma a^2/K)T, \tag{2.6}$$

where T is absolute temperature. In the Seebeck effect, a temperature difference between the junctions of two different materials (P-type and N-type) produces an electric voltage [36].

Increasing ZT is not a trivial task. The effective value should be $ZT > 4$ [33]. One possibility to improve the conversion efficiency is to further enhance the thermoelectric materials.

2.3.1.1. Thermoelectric Materials

There exists a huge variety of thermoelectric materials divided into different categories: metals-based, semiconductors, ceramics etc, which can have monocristal, polyscristals and nanocomposit structure and bulk, films, wires and clusters dimension [33].

Metal-based thermoelectric materials include Bismuth (Bi), Lead (Pb), Tellurium (Te) and Antimony (Sb). These metals have high electric and thermal conductivity, but are toxic and unstable at high temperatures [33]. In this category, Bismuth Telluride and its alloys are good thermoelectric materials below room temperature. However, the use of Tellurium is limited, since it is scarce, toxic and volatile at high temperatures [37]. Lead Telluride (PbTe) was found to have good thermoelectric properties at temperatures in the range of 300-700 K. It produces a higher Seebeck effect than that produced by Bismuth Telluride. Also, its ZT value increases with the temperature [38]. PbTe with Tin Telluride (SnTe) system (PbTe-SnTe) has been studied since 1961. The band gap goes to zero at $Pb_{0.4}Sn_{0.6}Te$ and therefore lower compositions of tin Telluride are required to ensure adequate band gap leading to ZT values near 1 for N-type alloys at 700 K [38].

From the category of semiconductor-based thermoelectric materials, Silicon-Germanium (SiGe) alloys are considered superior materials for thermoelectric generation [37], suitable for high temperature applications.

Recently, two new Phonon Glass and Electron Crystals (PGEC) materials have been used as a thermoelectric materials: Clathrates (lattices) and filled skutterudites.This group of ma-

terials shows promise for thermoelectric applications above 600 °C [38]. Superlattices have been found as structures which improve ZT by blocking the atomic vibrations that produce heat flow but still letting the electrons to flow as current. They are considered twice as efficient as previous bulk thermoelectric materials, but with difficulties in predicting thermal conductivity [38]. Skutterudites are effective in temperature range 500-700 K and increase the ZT value [33].

Another type of thermoelectric materials is half-Heusler alloys [33], with appropriate electrical properties and a high Seebeck coefficient at room temperature. Unfortunately, non-metallic inclusions in the metal thermoelectric materials reduce the mechanical strength of the material and increase porosity and corrosion.

Ceramics in comparison with the alloy materials are not oxidised and vaporised, therefore can be used in the high temperature conditions [33] and are less toxic. However, the oxide thermo-material fabrication process is not an easy task and requires high temperature. Good performing oxide thermoelectric materials are ZnO with $ZT > 0.6$ and BiCuSeO with $ZT > 1$ at temperatures above 800 K [39]. Materials based on Na_2CoO_4, have been reported as exhibiting an unusually high Seebeck coefficient ($100\mu V/K$) [37] but have been dismissed due to low electron mobility. The general problems with oxide thermoelectric are that they have weak mechanical strength, high contact resistance at interfaces of oxides and electrodes.

In contrast with ceramic materials, thermoelectric polymer materials are easy to manufacture and are flexible and appropriate for room temperature applications [33]. Polymers have low thermal as well as electric conductivity. The most promising polymer thermoelectric materials are ionic polymer materials (3,4-ethylenedi-oxythiophene, styrenesulfonate or PEDOT:PSS). They have high electricity conductivity and low thermal conductivity. In general, ZT for the PEDOT based thermoelectric materials vary from 0.006 to 1.02. The highest ZT value corresponds to PP:PEDOT material, which is PEDOT film prepared with a mixture of pyridine and PEPG (or triblock copolimer: poly(ethylen glycole)-poly(propylene glycol)-poly(ethylen glycole)) [40]. This material has high conductivity and a high ZT value.

2.3.2. Harvesters

The basic construction unit of a thermal harvester is a thermocouple, which is composed of an N-type thermoelectric material electrically in series with a P-type thermoelectric material as shown in Figure 2.7a [41]. When a temperature difference is applied across this material, heat begins to flow from the hotter to the cooler side. To boost the output voltage and get more power, many of these legs are connected electrically in series and thermally in parallel to form a thermopile, as it is demonstrated in Figure 2.7b. In order to create a thermal circuit, the needed elements are: thermoelectric module (TEM), heat source and heat sink. The heat source provides an elevated temperature and represents the hot side, while the heat sink represents the cold side and serves as heat dissipation in order to achieve a lower temperature [33].

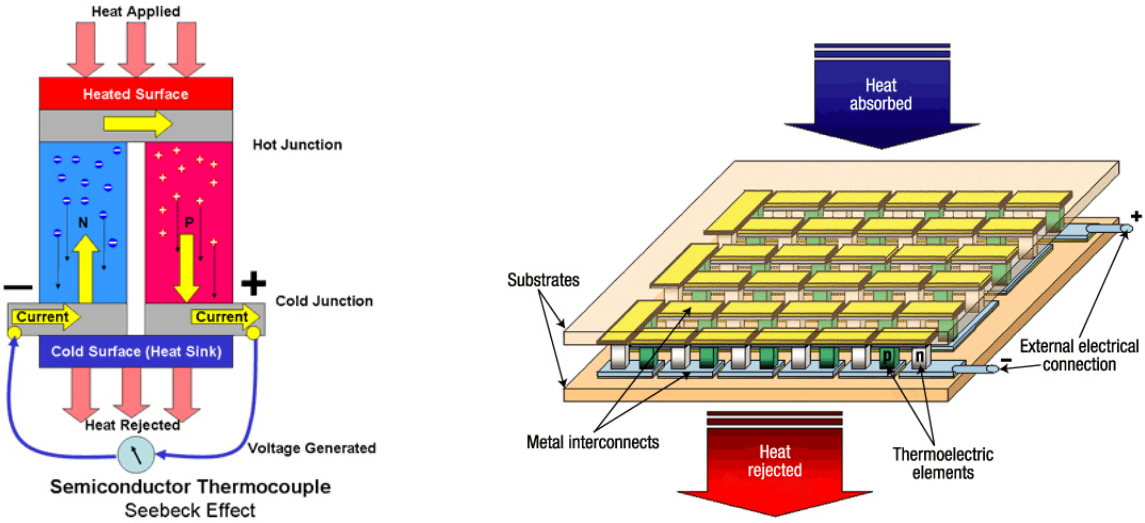

(a) Basic construction of a thermocouple [33]

(b) Diagram of a thermocouple [42]

Figure 2.7: Thermoelectric harvester general scheme

2.3.2.1. High-power generators

There are many prototypes developed for harvesting energy from an exhaust pipe [33]. Harvesting from a pipe could be a promising tool for the future, due to the constant temperature difference between the operating steam and water pipes and the ambient air. Further examples presented in the literature will be described below.

In [43], a prototype is introduced with the aluminium spreader block, that is designed to mount TEM on the exhaust. The module converts 5% of the thermal energy into electrical energy generating 14 W of electrical power. The waste heat recovery system consists of 6 modules. Water-cooled heat sinks provide the required minimum temperature on the cold side of the modules.

In [44], a SiGe module is developed. 72 modules were integrated and yielded a maximum power of 35.6 W. The module was developed to be deployed in gasoline engine vehicles. The maximum electric power of each module is about 1.2 W. The heat into electricity exchange efficiency of the generator was estimated to be 11% of the primary exhaust gas energy flow. The modules are placed between the exhaust pipe (inner shell) and the two pieces of water cooled jacket (outer shell) made of aluminium.

In [35], a similar structure is constructed, which reported a maximum power output of 255.1 W. An automobile exhaust thermoelectric generator prototype was installed in a GMC Sierra pick-up truck in 1999. The system consists of the generator, power conditioning unit and the interfaces to the test truck's engine coolant and exhaust systems. Dell constructed a prototype that can be implemented onto the steam pipe and steam meter robustly. Also, two special heat pipe assisted heat sink are connected to the TEG to further reduce thermal resistance at the cold side of TEG. The approximate power output is 6.9 W with 4 commercial modules as the temperature gradient reaches 63 °C [45].

In [46], an attempt is made to utilise a heat pipe in the design to harvest energy between two pipes with different temperatures. It contains rectangular finned tube heat pipes that are attached with copper blocks. Soldering is used to thermally bond the heat pipes and copper blocks. TEG is then sandwiched between two copper blocks.

2.3.2.2. Low-power generators

Low-power thermoelectric generators can be presented by body-mounted electronic devices such as smartphones, MP3 players or medical devices including e.g. hearing aids and cardiac pacemakers [47]. The power requirements of these body-mounted devices range from 5μW to 1 W. Batteries are widely used for these devices, but because they contain chemical substances that could be harmful, thermoelectric generators appear advantageous. An example of a body-mounted thermoelectric generator is a wristwatch driven by body heat. Two known manufacturers of these TEG wristwatches are Seiko and Citizen. The effectiveness of the device is around 0.1 %. It produces 300 mV voltage with temperature gradient of 1.5 K.

Thermoelectric modules are also used in thermal-energy sensors, such as sensors for power ultrasound effects, cryogenic heat-flux sensors, fluid-flow sensors and infrared sensors. Infrared sensors operate on the principle that any mass radiates heat. For example, in [48], a thermoelectric infra-red sensor (thermopile) using poly-silicon with a patterned Au-black absorber is designed as the vacuum-sealed package, fabricated with two thermopile pairs.

2.3.3. Models

Thermoelectric output is usually characterised by low power. Thus, it is important to identify the input parameters and operation conditions to provide the maximum power output. For example, one of the important parameters to be modelled in the waste heat recovery application is high power density. However, thermoelectric generators do not possess optimal geometry in order to achieve high power density. Hence it is important to maintain an optimal operation condition that will provide the maximum power output [49]. The main parameter to be controlled is the heat energy source. It will be considered below.

2.3.3.1. Thermoelectric harvesters output parameters

The maximum power output of thermoelectric harvesters are determined by two parameters and is calculated as:

$$P_{MAX} = \frac{V_{OC} I_{SC}}{4}. \tag{2.7}$$

The short-circuit current I_{SC} of a thermoelectric module is described by:

$$I_{SC} = \frac{S_b(T_H - T_C)}{R}, \tag{2.8}$$

where R is the is the electrical resistivity of the module, T_H, T_C are temperatures of hot leg and cold leg of the module, respectively, S_b is the Seebeck coefficient of the module.
The temperature difference is calculated by solving the following equations [50]:

$$Q_H = K(T_H - T_C) + S \cdot T \cdot T_H - \frac{1}{2}I^2R = \frac{T_{SOURCE} - T_H}{\psi_H}, \tag{2.9}$$

$$Q_C = K(T_H - T_C) + S \cdot T \cdot T_C - \frac{1}{2}I^2R = \frac{T_C - T_\infty}{\psi_C}, \tag{2.10}$$

where K is the thermal conductance of the module, T_{SOURCE} is the temperature of the heat source, T_∞ is the ambient temperature and ψ_H is the thermal resistance of the heat source.

For thermoelectric energy generation, T_{SOURCE} represents any harvested heat, for instance: fuels or waste heat (industrial processes, electronics, biological, exhaust gases). The analysis of the temperature model of these sources helps to analyse the potential power output.

2.3.3.2. Fuel Heat Model

The amount of energy released upon combustion per unit mass of fuel is described by the heating value of a fuel. Heating values can either be described as higher (gross) heating value or lower (net) heating value. The higher heating value (HHV or GCV) takes into account all water vapors generated during combustion and assumes that it condenses back into water. But practically, this latent heat will not be recovered and the water remains in vapor form, so the lower heating value (LHV or NCV) is more appropriate for use [51].
The connection between HHV and LHV is made using the following formula, where the heating values are in British thermal units per pound (Btu/lb) and H_2 represents the mass percent of diatomic hydrogen in the fuel:

$$HHV = LHV + 10.30(H_2 \times 8.94). \tag{2.11}$$

The HHV, or the amount of energy released per unit mass of fuel upon combustion, can be calculated if the elemental composition of the fuel is known, where C, H, N are the dry biomass weight percent of carbon, hydrogen, and nitrogen, respectively:

$$HHV = 3.55C^2 - 232C - 2,230H + 51.2C \times H + 131N + 20,600. \tag{2.12}$$

In order to compare a range of different fuels, the *fuel carbon intensity factor* is used. Typical relative carbon-intensity factors for various fuels are provided in [52].

$$fuel\ carbon\ intensity\ factor = GCV/NCV/(1 + 4.325/C : H) \tag{2.13}$$

2.3.3.3. Waste heat models

2.3.3.3.1 Industrial processes (oil refining, steel making, glass making)

According to [53], the waste heat in manufacturing is generated from several industrial systems distributed throughout a plant, as exhaust and flue gases, heated air from heating systems (such as high-temperature gases from burners in process heating); lower temperature gases from heat treating furnaces, dryers, and heaters; and heat from heat exchangers, cooling liquids, and gases. Waste heat can also be found within liquids and solids. Waste heat within liquids includes cooling water, heated wash water, and blow-down water. Solids can be hot products that are discharged after processing or after reactions are complete, or

they can be hot by-products from processes or combustion of solid materials. Other waste heat sources are not as apparent such as hot surfaces, steam leaks, and boiler blow-down water. In Table 2.1, a summary of the waste heat sources from the industry is provided.

Table 2.1: Temperature Range and Characteristics for Industrial Waste Heat Sources

Waste Heat Source	Temperature Range	Cleanliness
Furnace or heating system exhaust gases	600 to 2000	Varies
Gas (combustion) turbine exhaust gases	900 to 1100	Clean
Jacket cooling water	190 to 200	Clean
Exhaust gases (for gas fuels)	900 to 1100	Mostly clean
Hot surfaces	150 to 600	Clean
Compressor after-inter cooler water	100 to 180	Clean
Hot products	200 to 2500	Mostly clean
Steam vents or leaks	250 to 600	Mostly clean
Condensate	150 to 500	Clean
Emission control devices	150 to 1500	Mostly clean

According to [54], the quantity of waste heat contained in a waste stream is a function of both the temperature and the mass flow rate of the stream:

$$\dot{E} = \dot{m}h(t), \tag{2.14}$$

where $\dot{E}$ is the waste heat loss (Btu/hr); $\dot{m}$ is the waste stream mass flow rate (lb/hr) and $h(t)$ is the waste stream specific enthalpy (Btu/lb) as a function of temperature. Although the quantity of waste heat available is an important parameter, it is not alone an effective measure of waste heat recovery opportunity. It is also important to specify the waste heat quality, as determined by its temperature. According to [54], the magnitude of the temperature difference between the heat source and sink is an important determinant of waste heat utility or *quality*. A very good description of the waste heat sources is given along with the temperature ranges, advantages, disadvantages and recovery methods.

The source and sink temperature difference influences:

1. the rate at which heat is transferred per unit surface area of heat exchanger (denser fluids have higher heat transfer coefficients, which enables higher heat transfer rates per unit area for a given temperature difference), and

2. the maximum theoretical efficiency of converting thermal from the heat source to another form of energy (i.e., mechanical or electrical).

Finally, the temperature range has important ramifications for the selection of materials in heat exchanger designs.

2.3.3.3.2 Electronics (microchips)

The example of microprocessor heat waste was considered in [55]. The surface temperature of a high-performance integrated circuits (for instance, microprocessor) is typically very high, about 80-100 °C. High performance chips consume 40-100W of power and produce significant amounts of heat. The cooling is not always effective. Attaching a TEG to a microprocessor might be an effective solution for waste heat usage, due to the large temperature gradient between the chip surface and the ambient environment. [55] is questioning the possibility of the heat removal mechanism using heat spreader and heat-sink. Due to the non-uniform distribution on the microprocessor surface temperature, the thermoelectric conversion is reduced.

The input heat in the TEG can be considered as a constant value because the generated heat from the CPU at the steady state is equal to the dissipated heat. Therefore, the steady-state temperature of the layers of the heat dissipation path is away from the die surface, it is uniform. The steady-state temperature depends on the power consumption of all on-chip heat sources. It is given by the following equation [55]:

$$T(x, y) = \sum^{N} R_i Q_i, \tag{2.15}$$

where $T(x, y)$ is the temperature at the location (x, y) of TEG, R_i is the thermal resistance between heat source and location, Q_i is the power consumption of heat source, and N is the total number of on-chip heat sources. The power output for the model was obtained in the range $0.3 - 6.7$ mW.

2.3.3.3.3 Biological (warm-blooded animals)

One of the examples of sensors powered by human body heat are medical sensors that monitor physiological parameters. These sensors must operate up to a few years without maintenance. For this purpose, thermoelectric generators, which are attached to the skin, are used. Because of the temperature difference between the skin and the environment, the heat from the skin flows through the thermoelectric generator. The heat from the human body depends on the human body location. The power output also depends on the surrounding conditions. Normally, the heat emitted from the skin in indoor conditions (22°C) is $1 - 10\ mW.\text{cm}^{-2}$ [56].

Because the skin temperature is not uniform, knowledge of differences in body temperatures is required for designing the TEG taking into account the ambient temperature. Temperature in head and trunk is $33 - 36$°C. In extremities, at near-basal metabolic rate it can decrease below $30 - 25$°C periodically in any environmental temperature. Variation of the skin temperature on the location where the watch is usually worn (outer side of distal forearm) is higher than in other wrist locations. It causes the higher variations of thermal resistance of the forearm in the special point. In cold weather, the thermal resistance in extremities reaches very large values, that can be significantly larger than the thermal resistance of the ambient air [57].

If the air temperature is 22°C and thermoelectric materials are chosen such that $ZT = 1$, then the power output for a human is no larger than $1 - 2$ mW. For big animals, it can be equal to several milliwatts [57].

Thermoelectric harvesting on living being provides the reasonable amount of energy for practical applications.

2.3.3.3.4 Exhaust gases

In a vehicle the combustion of fuel (natural gas, gasoline, petrol, biodiesel blends, diesel fuel, fuel oil, or coal) results in the emission of warm exhaust gas; the integration of TEG can help to increase the energy extracted from the fuel without increasing fuel consumption and gas emissions [58]. There are three key factors that can lead to high-performance of a system: thermoelectric conversion system, optimal integration with the vehicle, and design of the thermoelectric interface [59].

The temperature of the exhaust gas changes in the range 400-650 °C and depends on time. Two parameters are taken into account for designing the TEG working on exhaust gas: temperature and mass flow rate. The absorbed heat at the hot side from exhaust gas is calculated as follows:

$$q_1^j = \frac{C_f M_f (t_{f_i}^j - t_{f_o}^j)}{r}. \tag{2.16}$$

The released heat at the cold side to ambient air is:

$$q_1^j = \frac{C_f M_f (t_{c_i}^j - t_{c_o}^j)}{r}, \tag{2.17}$$

where C is the specific heat capacity, M is the mass flow rate, t_f^j indicates the temperature of the exhaust gas and t_c^j the temperature of the cooling air.

In [60], the efficiency of TEG for exhausted gas is presented. The exhaust gas neutralisation (efficiency) is low and equals 2.66% with output power 65.6W.

2.3.4. Conclusion

The use of thermoelectric materials for waste-heat recovery and other applications can significantly help in an effort to save energy and reduce pollutants. Taking into account the low heat to energy conversion efficiency, the thermoelectric generators can be used as an additional power source. Moreover, many researches are devoted to increase the ZT merit in thermoelectric materials, which might lead to the increase of possible applications.

Thermoelectric heat power output calculations are identical for different sources of heating such as fuel heat, waste heat, etc. Typically, the power output is determined by temperature differences and thermal resistance. Besides these two parameters, the power output can be also defined by additional parameters. For instance, the mass flow rate is included in the model of power output for exhausted gases. The temperature differences for various heat sources were presented in this section.

2.4. Vibration

2.4.1. Resource

One of the most effective methods of implementing a vibration energy harvester (VEH) system is to use mechanical vibration to apply a force to a transducer or displace an electromagnetic coil. Power generation from mechanical vibration usually uses ambient vibration around the harvesting device as an energy source and then converts it into electrical energy [61].

Applying a force to a transducer represents the category of brute force harvesting devices. The generated power is the integral of force over distance. Examples are a heel strike generator or energy harvesting ticket gates. Large scale power generation uses direct-force type generation. However, this is not suitable for some applications as they usually limit the generator to one attachment point.

Displacing an electromagnetic coil or other movement-in-a-box approaches represents the category of inertial harvesting devices. The transducer will convert the motion into electrical power, proportional to the force over distance integral. Examples are kinetic watch generators using oscillating weights [62].
To have an idea about the power that can be harvested with VEH, Table 2.2 shows the achievable power density compared to other energy harvesting types. The unsatisfactory results shown in the table are mainly due to the fact that the resonant frequency of the generator is often not matched with the frequency of ambient vibrations or the frequency bandwidth of the generator is usually limited to a specific range which cannot cover the random vibration frequencies of external sources. If the frequency of ambient vibration deviates slightly from the resonant frequency of the energy harvester, the resulting power output of harvesters is reduced drastically [63].

Table 2.2: Power Density Comparison for Different Energy Types [61]

Harvesting method	Power Density
Solar Cells	15 mW/cm^3
Piezoelectric	330μW/cm^3
Vibration	116μW/cm^3
Thermoelectric	40μW/cm^3

2.4.2. Harvesters

Advanced Cerametrics [64] is a company that produces vibration-based energy harvesters that can replace batteries and be used to power wireless sensor nodes. Other companies, like Ambiosystems [65], Microstrain [66] or EnOcean [67] focus on producing battery-less sensor nodes that can be powered by harvesting energy from more sources, not only vibration.

Examples of vibrational harvesters and their capabilities are:

Perpetuum PMG17: up to 45mW@1grm*s*(15Hz) – 55mm diameter*x*55mm length resonant generator tuned to 100 or 120 Hz. The PMG17 transforms the kinetic energy of machine vibration into electrical current, which is sufficient to power completely wireless sensor nodes, including sensors, micro processors and 802.15.4 transceivers [68].

nPower PEG: The nPower PEG personal energy generator captures and stores the kinetic energy created from walking, running and biking and uses it to recharge mobile electronic devices [69].

Micro-electromagnetic generator: 20 Hz 2.5 μW@1 g manufactured within Microlab at UC Berkeley. Magnet size and coil properties were optimised, with the final device producing 46 μW in a resistive load of 4 K from just 0.59 m/s^2 acceleration levels at its resonant frequency of 52 Hz. This generator compares very favorably with other demonstrated examples in the literature, both in terms of normalised power density and efficiency [70].

Metglas 2605SC: Compared to piezoelectric materials, the Metglas 2605SC offers advantages including higher energy conversion efficiency, longer life cycles, lack of depolarisation and higher flexibility to survive in strong ambient vibrations. In experiments, the maximum output power and power density on the resistor can reach 200 μW and 900 μW/cm^3, respectively, at a low frequency of 58 Hz. For a working prototype under a vibration with resonance frequency of 1.1 KHz and peak acceleration of 8.06 m/s^2 (0.82 g), the average power and power density during charging the ultracapacitor can achieve 576 μW and 606 μW/cm^3, respectively, which compete favorably with piezoelectric vibration energy harvesters [71].

2.4.3. Models

2.4.3.1. Piezoelectric Vibration Energy Harvester Modelling

In [62], the piezoelectric transducer is modelled as equivalent to the electric circuit structure shown in Figure 2.8, with the maximum obtainable output power given by:

$$P_{max} = V_{po}^2 f_o C_p \frac{8Q}{\pi}, \tag{2.18}$$

where V_{po} is the Open Circuit Voltage (OCV) of the piezo, f_0 is the mechanical excitation frequency, Q is the quality factor of the resonant charging path and C_p is the capacitance of the piezo.

In [72], the spring-mass-damper model of the piezoelectric vibration harvester is used to find the displacement of the end mass and the stress along the beam for input sinusoidal base excitation. The resonant frequency of the system is calculated using Rayleigh method, and the expression for voltage generated across the load resistance (R) is derived. The performance of the energy harvester is studied in terms of the amount of power generated.

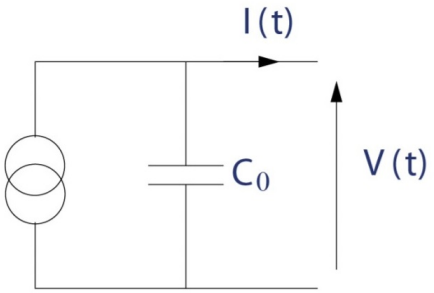

Figure 2.8: Piezoelectric transducer model [62]

The results from analytical solution are verified using finite element (FE) analysis carried out in COMSOL Multiphysics. The spring-mass-damper model of the vibration energy harvester consists of an equivalent mass m, a spring with spring constant k and dampers: b_m - mechanical damping coefficient, θ -electrically induced damping coefficient.

The power supplied to the load by a piezoelectric harvester is $\frac{v(t)^2}{R}$, where $v(t)$ is taken from the dynamic response for the case of parallel connection of the piezoelectric layers [72]:

$$\begin{cases} v(t) = -\frac{2jR\theta m\omega^3 Y_0}{(\omega_n^2-\omega^2+j2\xi_m\omega\omega_n)(m+j2mRC_p\omega)+j4R\theta^2\omega} e^{j\omega t} \\ z(t) = -\frac{(1+2jRC_p\omega)m\omega^2 Y_0}{(\omega_n^2-\omega^2+j2\xi_m\omega\omega_n)(m+j2mRC_p\omega)+j4R\theta^2\omega} e^{j\omega t}. \end{cases} \tag{2.19}$$

In the above equations, ω_n is the natural frequency of the harvester and ω is the angular frequency of the harmonic motion of the input base excitation. C_p is the capacitance of a single piezoelectric layer, $y(t)$ is the base displacement due to input vibration (while Y_0 is its amplitude), $z(t)$ is the displacement of the end mass relative to the vibrating base, $v(t)$ is the voltage generated, ξ_m is the mechanical damping ratio.

For the case of a series connection of the piezoelectric layers, the equivalent capacitance halves and the dynamic response becomes [72]:

$$\begin{cases} v(t) = -\frac{2jR\theta m\omega^3 Y_0}{(\omega_n^2-\omega^2+j2\xi_m\omega\omega_n)(2m+jmRC_p\omega)+j2R\theta^2\omega} e^{j\omega t} \\ z(t) = -\frac{(2+jRC_p\omega)m\omega^2 Y_0}{(\omega_n^2-\omega^2+j2\xi_m\omega\omega_n)(2m+jmRC_p\omega)+j2R\theta^2\omega} e^{j\omega t}. \end{cases} \tag{2.20}$$

In [70], the same techniques as in [72] are used but with the coupled electro-mechanical beam equation being used in modal coordinates.

2.4.3.2. Electromagnetic Energy Harvester Modelling

Figure 2.9 shows the basic scheme for the operation mode of an Electromagnetic Energy Harvester.

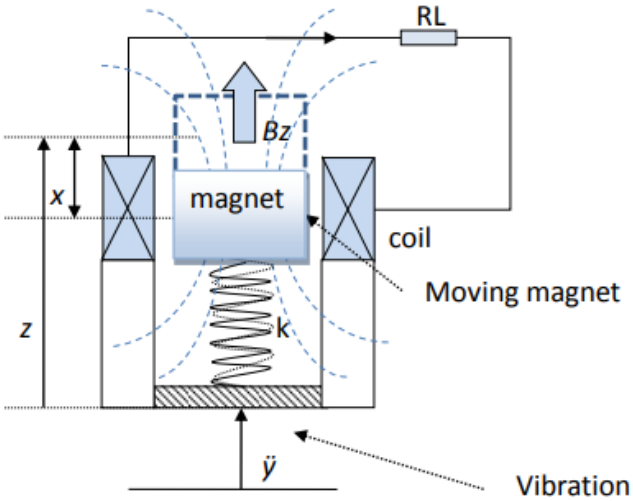

Figure 2.9: Electromagnetic energy harvester [70]

The governing equations for a single degree of freedom (DOF) model of an Electromagnetic (EM) VEH can be written as:

$$\begin{cases} m\ddot{z} + d\dot{z} + kz = -\alpha V_L - m\ddot{y} \\ \dot{V}_L + \omega_c V_L = \delta_c \omega_c \dot{z}, \end{cases} \tag{2.21}$$

where α is the electrical coupling force factor, δ_c is the conversion factor,ω_c is the characteristic cut-off frequency, L_e is the coil's self-inductance, m is the mass, d is the mechanical damping, k is the elasticity of the spring and V_L is the voltage across the load R_L.

The electrical power P_e across the resistive load R_L in frequency domain with a harmonic input $\dot{y} = Y_0 e^{j\omega t}$ is given by,

$$\begin{aligned} P_e(\omega) &= p_e(\omega)|Y(j\omega)|^2 = \frac{|V(j\omega)|^2}{2R_L} = \frac{|H_{VY}(j\omega)|^2 |Y(j\omega)|^2}{2R_L} = \\ & \frac{Y_0^2}{2R_L} \left| \frac{m\delta_c \omega_c j\omega}{(\omega_c + j\omega)(-m\omega^2 + dj\omega + k) + \alpha\delta\omega_c j\omega} \right|. \end{aligned} \tag{2.22}$$

2.4.3.3. A general model for electromagnetic and piezoelectric harvesters

Figure 2.10 shows the mechanical principles for electromagnetic and piezoelectric transducer types. The magnet moves inside the coil causing the displacement z to vary. The harvested power is given by equation 2.22, where the corresponding parameters are adjusted according to Table 2.3. This table shows the parameters for these types of VEH.

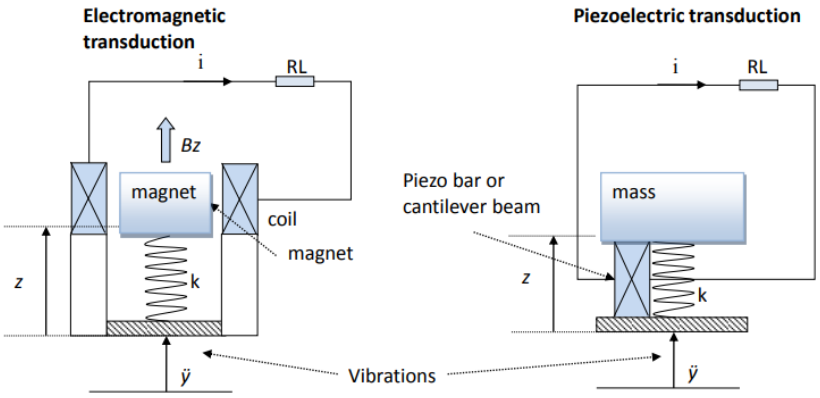

Figure 2.10: Electromagnetic and Piezoelectric Transduction schemes [70]

Table 2.3: Equation Parameters [70]

Parameters	Electromagnetic	Piezoelectric	Description
α	B_z/R_L	$h_{33}C_0$	Electrical restoring force factor
δ_c	$B_z l$	αR_L	Conversion coefficient
ω_c	$\frac{R_L}{L_e}$	$\frac{1}{R_L C_0}$	Characteristic cut-off frequency

2.4.3.4. Electrostatic energy harvester

Electrostatic harvesting of mechanical energy is based on varying vibration-dependent capacitance of variable capacitors (varactors). Ambient vibrations induce a displacement of charged plates of varactors and mechanical energy is converted into electrical energy. The electrostatic energy stored within capacitor is given by:

$$E = \frac{1}{2}QV = \frac{1}{2}CV^2 = \frac{1}{2}\frac{Q^2}{C}, \tag{2.23}$$

where $C = \epsilon_r \epsilon_0 \frac{A}{d}$ for a parallel capacitor. A variation in capacitance causes either voltage or charge increase. In the same fashion, in order to vary the energy at constant voltage, it is needed to counteract the electrostatic force between the mobile plates, $F_e = \frac{1}{2}\epsilon\frac{AV^2}{d^2}$, while at constant charge.

Figure 2.11 shows the equivalent circuit for the varactors based harvesters.

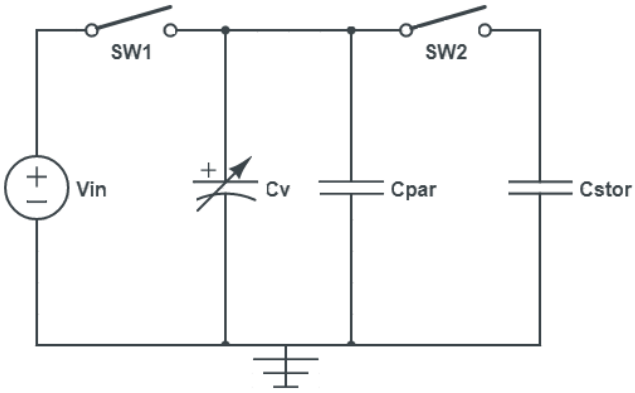

Figure 2.11: Equivalent circuit for a Electrostatic energy harvester [70]

The maximum potential energy per cycle that can be harvested is

$$E = \frac{1}{2} V_{in}^2 \Delta C \left(\frac{C_{max} + C_{par}}{C_{min} + C_{par}}\right) \longrightarrow E = \frac{1}{2} V_{max} V_{in} \Delta C, \tag{2.24}$$

with $\Delta C = C_{max} - C_{min}$ and V_{max} representing the minimum and maximum capacitance of the varactors and the maximum allowable voltage across a switch, respectively.

2.4.4. Conclusion

In [62], a simplistic way of modelling piezoelectric energy harvesters is given, for which in [72], mathematical expressions for natural frequency, displacement of end mass and generated voltage for parallel and series configurations are derived. For the parallel configuration, the derived expressions have been evaluated in MATLAB and the results are validated using finite element analysis of an identical system. The model is used to find the short circuit and open circuit resonance frequencies of the energy harvester. The effect of load resistance on the resonance frequency, displacement of the end mass and generated power is studied, and the optimal value of the load resistance is found for maximum power generation. The obtained analytical model is very detailed and can be further used and applied in our research. In [70], a similar analysis is done for cantilever beam as in [72], using modal coordinates and the results are validated through experiments, proving the accuracy of the model.

As a general conclusion, there is a large number of proposals for Vibration Energy Harvesters in the literature and even if the mathematical tools to generate these models might be different from one author to another, in the end the models are accurate and ready to be used.

2.5. Wind Power

Wind power has been harvested for thousands of years, first to propel sailing boats, then to drive mechanical systems such as mill, pumps, etc. Nowadays, it can be harvested by a range of methods to produce electrical power.

2.5.1. Resource

Wind is a displacement of air due to different causes, the main one being the sun heating the non-uniform surface of the earth. The different elements at the surface of the earth (land, forest, desert, water, mountains ...) radiate the solar heat in the atmosphere in different fashions, such that hotter and colder masses of air appear, causing air to move around [73]. This phenomenon applies at a planetary level (Figure 2.12a), but also at much smaller scale with more local winds like coastal wind (Figure 2.12b).

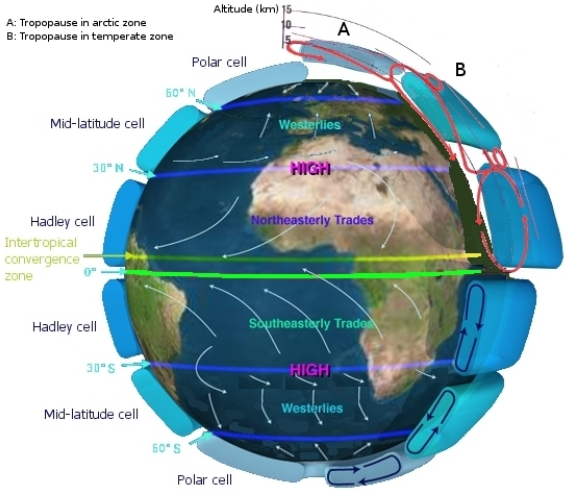

(a) Planetary Winds

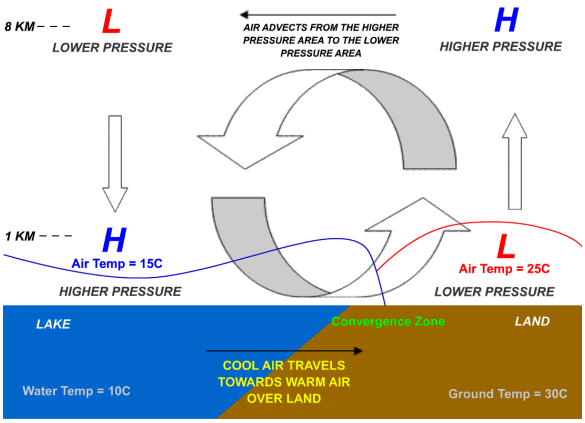

(b) Lake or Sea Breeze Phenomenon [74]

Figure 2.12: Main Wind Generating Phenomena

2.5.2. Harvesters

There are two main types of wind turbines designs: vertical axis (VAWT) or horizontal axis (HAWT).

2.5.2.1. Horizontal Axis Wind Turbine

Horizontal axis wind turbines are the most commonly used type of wind turbine, and they are used almost exclusively in high-power installation. Those turbines offer a range of power outputs from a few watts to thousands of kilowatts.

2.5.2.1.1 Down- vs Up-wind

We distinguish two main types of HAWT depending on wether they face the wind up- or down-wind. The difference is illustrated in Figure 2.13 [75].
Downwind Turbines do not need a yawing system as the blades act as vanes. The position of the blades downwind allows them to bend more as there is no risk of collision with the mast. This also reduces the effort on the mast as some energy is dissipated in the blades' flexibility. The design of the turbine is then simplified. However, the flexibility of the blades and the turbulences generated by the mast can reduce the efficiency of the turbine.

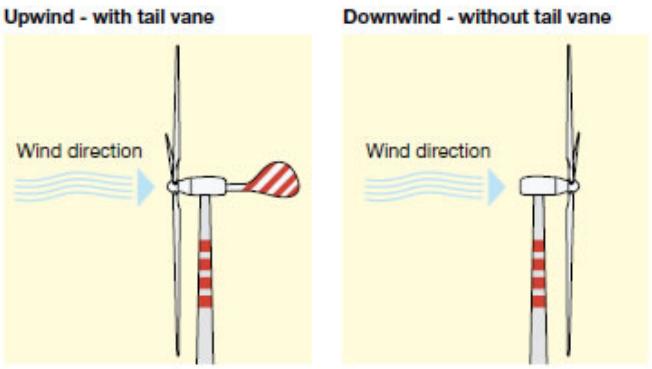

Figure 2.13: Up- and Down-wind Turbines [75]

Upwind turbines are more complex to design than downwind designs as they require stronger structural elements for the blades and the mast, but present a better efficiency as less energy is lost in the flexibility of the blades and the turbulences generated by the mast.
Small turbines are often oriented with the help of a tail, while larger turbines are oriented by a yaw motor which rotates the turbine based on measurements from a wind vane.

2.5.2.1.2 Other Characteristics

High power HAWTs are often equipped with variable pitch to control the rotation speed of the turbine, which also allows feathering to help the braking system stop the turbine. Some (small) turbines might also be equipped with ducts to reduce noise and increase extracted power.

2.5.2.2. Vertical Axis Wind Turbine

Vertical axis wind turbines generally have a lower efficiency than horizontal axis turbines, but present some advantages: the turbine is omnidirectional, i.e. it does not need to be oriented according to the wind direction and the alternator is located at ground level, reducing the weight on the top of the mast. The turbines are also well adapted to be installed on existing structures, like on top of a building.

There are however some drawbacks with the vertical axis turbine design: the omni-directionality of the VAWT presented as an advantage above requires stronger elements to withstand non constant torque due to gusts of wind; difficulties in modelling them make the design of vertical axes turbines more complex compared to the horizontal case.

2.5.3. Modelling Electricity Production of Wind Turbine

To model the energy output of a wind turbine, we go through a three steps process. We first need to model the resource availability and the turbine characteristics, and then deduce the electrical power output.

2.5.3.1. Resource Modelling

To determine the viability of a wind turbine installation, a key indicator is the mean wind speed on site [76]. The mean speed V_m is typically obtained through measurement over an extended period at the implantation site.

2.5.3.1.1 Weibull Distribution

The Weibull distribution is used to approximate the mean wind speed distribution in Figure 2.14 and can be expressed as follows:

$$p(V_m) = \frac{k}{C}\left(\frac{V_m}{C}\right)^{k-1} e^{-V_m C^k}, \tag{2.25}$$

where k and C are the shape and scale coefficients, respectively. These coefficients are adjusted to match the wind data on site.

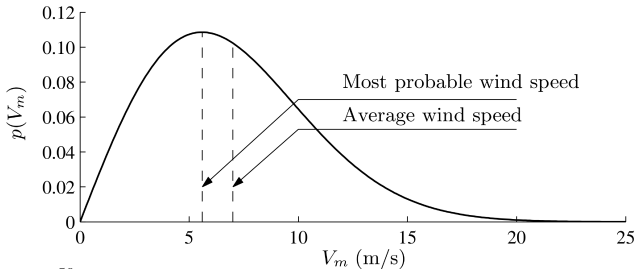

Figure 2.14: Weibull probability distribution of mean wind speeds [76]

2.5.3.1.2 Vertical Distribution

The wind is also distributed in a vertical fashion, i.e. the wind speed depends on the height. To represent this distribution, [76] uses Prandtl's logarithmic law:

$$\frac{V_m(z)}{V_m(z_{ref})} = \frac{\ln(z/z_0)}{\ln(z_{ref}/z_0)}, \tag{2.26}$$

with z_{ref} the reference height, usually 10m, z the height with respect to the ground, and z_0 the roughness length which is dependent on the nature of the ground. Some typical values are e.g. 0.2 to 0.3 mm for sand and 40 to 100mm for high grass [76].

2.5.3.1.3 Energy in the Wind

The wind as a fluid in movement contains a certain amount of kinetic energy [76]:

$$\text{Average Energy} = \frac{1}{2}\rho A \int_0^{T_p} V^3 dt, \tag{2.27}$$

where ρ is the density of the fluid, i.e. air, A the considered cross-section through which the wind is passing, V the speed of the wind and T_p the time interval considered.

Betz's Law gives an upper-band of the energy that can be extracted from the wind using an open flow wind turbine (actuator disk, Section 2.5.3.2).In practice, the wind turbine almost never reaches the Betz's limit (59% of the kinetic energy) [76, 77].

2.5.3.2. Turbine Modelling

The literature presents a large number of model based on HAWT and VAWT technologies and on power grid and electric power points of view. They are briefly described in the following sections.

2.5.3.2.1 Horizontal Axis Turbine

As there is less variety in the design of horizontal axis wind turbines, there are only two main types of models:

Actuator Disk Model: The actuator disk model is based on the momentum theory and an idealised wind energy extracting device. After applying different fluid mechanic laws, the power extracted from the wind can be expressed as follows:

$$P_D = 2\rho A_D V^3 a(1-a)^2, \tag{2.28}$$

where A_D is the disk area and a the axial flow interference factor [76].

Blade Element Models: It is also possible to extensively study of the geometry of the wind turbine and its aerodynamic characteristics to produce more accurate models [76].

2.5.3.2.2 Vertical Axis Turbine

The model of vertical axis turbine is very dependent on the technology and design of the turbine. Several models for Darriesus turbines are presented in [78].

2.5.3.2.3 Power Grid Point of View

There have been several studies on the influence of a wind turbine in power electric networks. Among them, [79] focuses on fixed speed turbines within depth study of all the chain from the drive train to the electric network, considering the different states of the turbine (starting, stopping), while [80] provides a model for variable speed wind turbine, which includes power electronics to maintain a suitable current frequency for the network.

2.5.3.3. Electricity Production Modelling

As shown above, a wind turbine can be modelled by an extensive study of its geometry and by applying fluid mechanic principles. However, due to the complexity of the mechanical models of the diverse types of wind turbine, we will focus on the power output characteristics, i.e. the potential of a wind turbine to produce electric power from a given wind speed or speed range.

2.5.3.3.1 Wind Turbine Characteristic

As simple users of wind turbine generators, one can use the very detailed characteristics that manufacturers provide for each turbine they produce, and from there extract simple models as presented in Figure 2.15.

The typical values used to characterise a wind turbine include: the wind cut in speed V_{ci} (wind speed at which the turbine starts producing), the rated speed V_r of the wind turbine at which it reaches its nominal power output P_r, and the cut off speed V_{co} at which the wind turbine is stopped for safety reasons, such as breaking risk or early fatigue of the turbine.

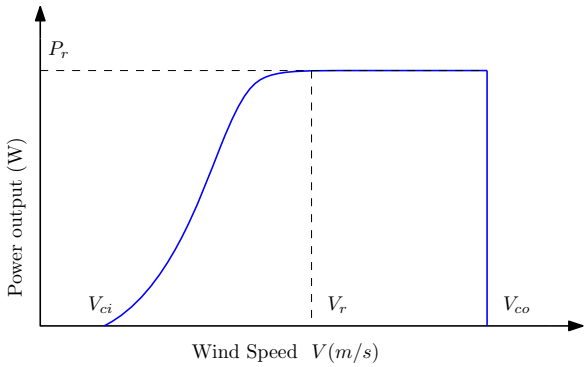

Figure 2.15: Typical wind turbine power output characteristic

2.5.3.3.2 Electricity Production

Once the wind resource and the wind turbine characteristic are obtained, the electricity production of the given turbine under the estimated wind distribution still needs to be deduced. For this [81] proposes a model with a focus on the cost effectiveness of the turbine taking into account outage history. Several models based on learning and approximation techniques were developed to estimate the electricity production on wind turbine or wind farms, such as neural networks in [82] or fuzzy models in [83] (fuzzy model).

2.5.4. Conclusion

In the context of telecommunications, the presence of a wind turbine might perturb the transmission. Various studies [84, 85] have shown that wind turbine can influence wireless transmissions. Indeed turbine representing big surfaces (with respect to the used wavelength) in movement can generate some Doppler effect which may affect the nearby devices. There might be some shadowing effect if the blades sweep in front of the antennas. For those reasons, one should consider the type, size and position of the wind turbine before implanting one or multiple turbines next to a transmitter, adding to the already known constrains such as noise, visual impact, or maintenance.

2.6. Electromagnetic Radiation

Harvesting power from electromagnetic sources has attracted recent interest because of the broadcast nature of wireless communications.

2.6.1. Resource

According to the distance of the application, EM sources can be divided into two categories: near field and far field. EM induction and magnetic resonance methods are near field methods to harvest power for wirelessly recharging devices within a distance of a wavelength, and are controllable and predictable. In far field applications, energy received by antennas from RF/microwave radiation is converted to power by rectifier circuits. The energy could be from ambient radiation or from dedicated beam-forming signals emitted by a known transmitter. This kind of energy is available in reasonable quantities in urban environments, but is very scarce in sparse sub-urban environments. The harvestable power levels may be as low as -40dBm for ambient sources, and are unpredictable and uncontrollable. Dedicated sources can be partially controllable and predictable if the emitting source and receiving antenna are static. However it becomes random if the receiver is moving.

The Radio Frequency (RF) power densities in both urban and semi-urban environments in London are extensively studied in [86]. As mentioned in the paper, significantly higher power density is available for harvesting in the Global System for Mobile Communications (GSM900 and GSM1800 bands), while the available energy decreases in the DTV, 3G and WiFi bands successively. Other studies consider wireless power transfer applications operating at microwave frequencies. Working in these bands permits the use of smaller antennas, thus reducing the required antenna aperture and making antenna beam steering easier.

2.6.2. Harvesters

The system design is based on a simple concept of capturing the ambient RF energy using the following equipment: appropriate antenna, tuning circuit, voltage multiplier, storage capacitor.

2.6.3. Models

Energy harvesting models are broadly classified as deterministic models (Section 2.6.3.1) and stochastic models (Section 2.6.3.2). Deterministic models may be applied for dedicated RF energy sources, while stochastic models may be applied for ambient RF energy sources.

2.6.3.1. Deterministic models

In deterministic models, full knowledge of energy arrival instants and amounts is known in advance by the transmitters. The advantage is that these are useful to characterise the optimal energy scheduling strategies and provide insights into designing suboptimal schemes.

A major energy harvesting solution is to collect energy from RF signals which are artificially generated by other communication devices. The received RF power in free space propagation can be modelled with the **Friis equation** as follows:

$$P_r = P_t G_t G_r \left(\frac{\beta\lambda}{4\pi d}\right)^2, \tag{2.29}$$

where λ is the wavelength, β represents the polarisation loss, P_t is the transmit power, G_t and G_r denote the transmitting and receiving antenna gains, respectively, and d is the distance between the transmitter and the receiver. The above model is commonly used for **dedicated RF energy harvesting**. Dedicated RF energy harvesting models can be grouped into deterministic models, because with dedicated sources the exact amounts and times of energy arrivals can be known reasonably accurately, ignoring multipath and fading phenomena for far-off, non-line-of-sight sources.

2.6.3.2. Stochastic models

Recent attention has focused on stochastic energy harvesting models in which the energy renewal processes are regarded as random processes. One major advantage of this type of models is that there is no need for the non-causal knowledge of the Energy State Information (ESI), thereby making them suitable for applications when the ESI is unpredictable. Models for ambient RF energy harvesting can be grouped into stochastic models because neither the amounts nor the times of arrivals can be known non-causally at the harvester.

By leveraging RF signals, new dedicated energy harvesting technologies may theoretically be proposed to deliver information and power simultaneously [87]. However, simultaneous energy and information delivery is not possible due to circuit design constraints. Therefore, practically, energy and information can be transferred in a time-sharing manner, or a power-splitting manner [88]. This constitutes a practical model of energy harvesting in a wireless information channel.

2.6.3.2.1 Stochastic geometry model

This model is used to describe an ambient RF energy harvesting source [88]. A network presented in [89] comprises a number of ambient RF energy sources, i.e., wireless information transmitters, in which a sensor node is powered solely by the energy harvested from these energy sources. Figure 2.16 shows the considered network model, where the sensor node harvests RF energy emitted from the ambient sources and utilises the harvested energy to perform uplink data transmission to the data sink. The distribution of ambient RF energy sources is modelled as a Ginibre $\alpha-$DPP (Determinantal Point Process). The transmit power of the ambient RF sources are assumed to be identical. The sensor is considered to lie at the origin. The sensor is battery-less and utilises the instantaneously harvested RF energy to supply its operations.

The performance metrics of the sensor node are defined as the expectation of RF energy harvesting rate, the variance of the RF energy harvesting rate, the power outage probability

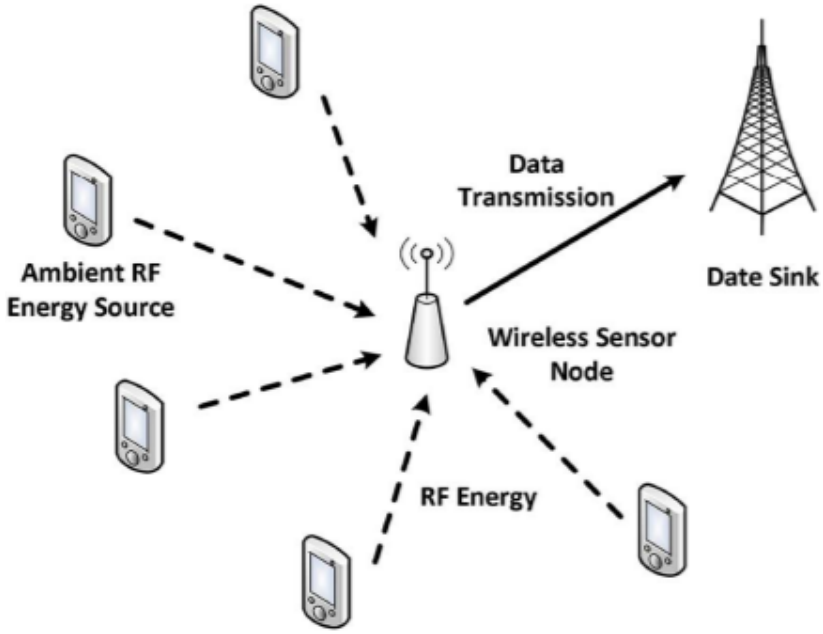

Figure 2.16: Network model of ambient RF energy harvesting [89]

and the transmission outage probability. Power outage occurs when the sensor node becomes inactive due to lack of sufficient energy supply. The power outage probability is then defined as $P_{po} = Prob(P_H < P_C)$, where P_H is the harvested energy, and P_C is the consumed energy. Let $m > 0$ denote the minimum transmission rate requirement. If the sensor fails to achieve this requirement, a transmission outage occurs. The different theoretical performance metrics are estimated by a Monte Carlo simulation of the underlying α-DPPs. As shown in Figure 2.17, the numerical results, averaged over 5×10^5 simulation runs, match the analytical results accurately over a wide range of densities ρ from 0.01 to 1. The numerical results verify that the analytical expressions for the upper bounds are very tight for different values of α.

2.6.4. Conclusion

The models presented are quite standard and widely used, covering most of the aspects of practical energy harvesting. This is shown by the tightness of the analytical and simulated results. We may use these models directly. However some missing aspects not covered in the literature are moving sources/receivers, indoor spaces and also ultra-high frequency bands like mm-wave and 60GHz bands, which are potential new frequency bands to be used for 5G. These could be grounds for future work.

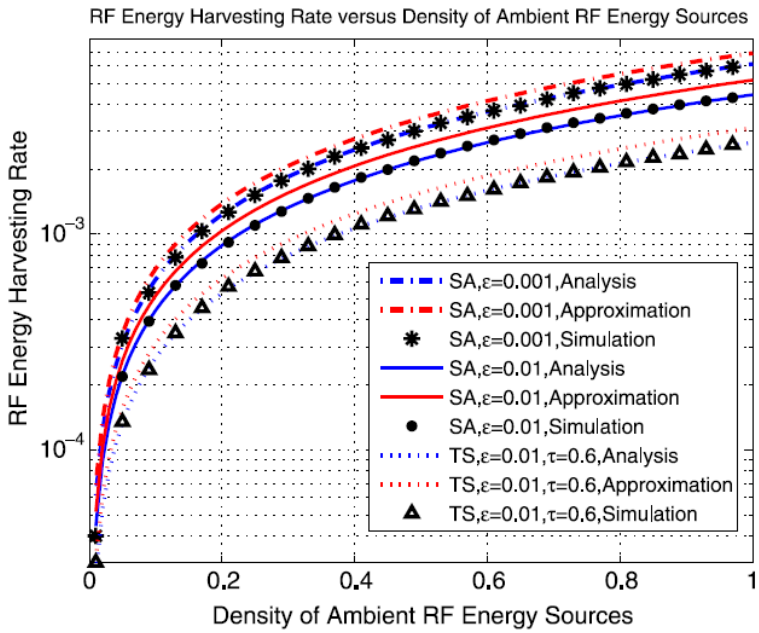

Figure 2.17: RF energy harvesting rate versus density of ambient RF energy sources [89]

2.7. Conclusion

In this section, the main types of energy harvesting sources have been surveyed. For each type, the resource itself was described along with the technology used to extract energy and the corresponding models used in the literature.

3. Energy Storage Technologies

3.1. Introduction

Storing surplus electricity removes the need to immediately consume renewable energy as it is generated. This solution has received greater attention as a means to support higher levels of electricity generation from renewable energy, especially from variable sources such as wind and solar photo-voltaic panels [90]. The use of renewable energy and storage systems shows that the reduction of both electricity expenditure and harmful emission can be achieved while also minimizing the dependence on the electricity grid [90]. This gives an opportunity to mobile service providers as they can use renewable energy in core networks thus reducing operational cost.

Energy storage technology can be divided into 4 classes depending on the form in which the harvested energy is stored:

- Mechanical Storage System
- Electrical Storage System
- Electrochemical Storage System

3.2. Mechanical Energy Storage

In this section we describe two mechanical storage technologies, specifically: Small-Scale Compressed Air (CA) energy storage and Flywheel energy storage.

3.2.1. Small-Scale Compressed Air (CA)

A CA works based on the gas-turbine technology. In a CA, during low energy demand, ambient air is compressed and stored under pressure typically in an underground cavern. When electricity is required, the pressurised air is heated and expanded in an expansion turbine driving a generator for power production. Usually, the expanded air is mixed with fuel and combusted. Then, it is further expanded through a low pressure turbine, which is connected to the generator to produce the electricity. The waste heat during combustion can be captured using a recuperator.

There are three ways in which a CA system can deal with the heat to store the compressed air. Air storage can be adiabatic, diabatic, or isothermal.

Adiabatic storage prevents heat transfer between the fluid and the surrounding since the system is insulated. In this way, it keeps the heat produced by compression and returns it to the air as it is expanded to generate power. The theoretical efficiency of adiabatic storage approaches 100% with perfect insulation, but in practice the efficiency is expected to be 70%. This is a subject of ongoing study. German project ADELE [91] proposed a large

industry-scaled adiabatic CA plant.
Diabatic storage dissipates much of the heat of compression with inter-coolers into the atmosphere as waste. During recovery process, the temperature of the compressed air indicates the amount of stored energy. Consequently, if the temperature is low, the air must be re-heated prior to expansion in the turbine to power the generator. This reheating can be accomplished with a natural gas fired burner. In fact, a diabatic-CA is not a pure energy storage system, but a hybrid system composed of a natural gas fired turbine and an electrical storage system. This degrades the efficiency, and, while this approach is relatively simple, the burning of fuel increases the overall costs, compromising the ecological benefits associated with renewable energy sources. Nevertheless, this is the only system which has been implemented commercially.
Isothermal compression and expansion systems attempt to maintain the temperature by constant heat exchange to the environment. They are only practical for low power levels, without very effective heat exchangers. The theoretical efficiency storage approaches 100% for perfect heat transfer to the environment, but in practice neither of these perfect thermodynamic cycles are obtainable, as some heat losses are unavoidable.

CA systems are capable of providing large energy storage of hundreds of Mega Watts (MW) with a single unit and they are often intended for large scale applications. However, to fulfill the mobile communications requirement, a small scale CA system has been proposed as a technology for the energy storage in a stand-alone renewable energy power plant (photovoltaic power), designed to provide the energy demand of a radio base station for mobile telecommunications [92]. The proposed solution's goal is to reduce the typical costs required by using diesel generators to power radio base stations, enhancing therefore the sustainability of the system. However, this work focuses on the sizing of the deployment. No proper model is yet available in the literature, as this technology is still new for base station applications.

3.2.2. Flywheel

A flywheel stores energy mechanically in the form of kinetic energy (a mass rotating about an axis). A Flywheel device is made up of a central shaft that holds a rotor and a flywheel. This central shaft rotates on two magnetic bearings to reduce friction. These are all contained within a vacuum to reduce aerodynamic drag losses. The energy is stored by accelerating the rotor/flywheel to a very high speed and maintaining the energy in the system as kinetic energy. Then the flywheel releases energy by reversing the charging process so that the motor is then used as a generator. As the flywheel discharges, the rotor/flywheel slows down until eventually coming to a complete stop.

In order to optimise the energy-to-mass ratio, the flywheel needs to spin at the maximum possible speed because kinetic energy only increases linearly with mass but goes as the square of the rotational speed.

Traditional flywheel rotors are usually constructed of steel and are limited to a spin rate of a few thousand Revolutions per Minute (RPM). Advanced flywheels constructed from carbon fiber materials and magnetic bearings can spin in vacuum at speeds up to 40000 to 60000 RPM [93]. The typical power range of this solution is from some kW to tens of MW, for times

of seconds or hours.

In Flywheel Energy Storage Systems (FESS), losses arise due to friction and aerodynamic drag which increases with higher rotor speed. For this reason, dynamic behaviour of FESS is characterised by both rotor mass and frictional components. Another important factor in FESS is the loss due to aerodynamic drag.

Based on this idea, the model in [94] represents the FESS system into an equivalent electrical circuit. Other models in the literature attempt to represent the energy storage in flywheels in more detailed ways. Among them, a finite element-based method is suggested in [95].

3.2.3. Conclusion

Small-Scale Compressed Air is still a new technology for telecommunication applications. More research is needed, in particular for what regards the modelling of this storage technology. On the contrary, Flywheel energy storage is a well studied technology and different models are available in the literature.

3.3. Electrical Storage

In this section we describe two mechanical storage technologies, specifically: super-capacitors (SC) energy storage and Super-Conductive Magnetic (SCM) energy storage.

3.3.1. SC

A super-capacitor has high power density but a low energy density. It can be connected in parallel with the battery for the purpose of charging or discharging high power in a short period of time.

In the following section (3.3.1.1), super-capacitors are evaluated, describing their advantages and disadvantages for serving as a storage technology, then electrical and mathematical models are provided. These models give a very good approximation of the super-capacitor characteristics when compared to a real device in slow discharge applications.

3.3.1.1. State of the Art

Super-capacitors consist of two parallel electrodes immersed in an electrolyte separated by a dielectric insulator like a battery. The electrodes are made using porous material and have a surface area much greater than that used in battery electrodes. The capacitance of the super-capacitor is much more difficult to calculate than a normal capacitor, as it depends on complex phenomena occurring in the micro-pores of the electrodes. The energy stored in the super-capacitor is given by $\frac{1}{2}CV^2$, where C is its capacitance (measured in Farads) and V is the voltage between the terminals, and the charge Q (measured in coulombs) stored in the super-capacitor is given by CV . Super-capacitors can be made using a double-layer (carbon such as Lithiated graphite) material for the negative electrode and battery-like material (lead or nickel oxide) for the positive electrode. Such devices are often referred to as

hybrid capacitors. The energy density of these devices is significantly higher than for carbon/carbon double-layer capacitors [96].

Super-capacitors, are electrostatic devices. They present a virtually unlimited cycle life, a high power density due to the low internal resistance and a fast recharging phase, but the maximum output voltage is low and the linear discharge characteristic drops down to 0 and does not allow to exploit the whole energy amount at a voltage supply suitable for consumer electronics. The high self-discharge (about 50% in 30 days with respect to less than the 5% for a Li-ion battery) and the linear discharge characteristic of super-capacitors prevents the usage of the whole energy amount stored in the super-capacitors [97].

The choice of the storage element is made between rechargeable batteries and electric double-layer capacitors (EDLC or super-capacitors). They represent an innovative technology available on the market, namely the lithium-ion capacitor (LIC). This cutting edge technology combines the high cell voltage, energy density and low self-discharge of a lithium battery with the power density, high capacity and long cycle life of a super-capacitor [98].

Compared to rechargeable batteries, capacitors have a set of advantages [99], [100]:

- More than 1 million recharge cycles
- Predicable remaining energy independent of discharge modes
- Robust to temperature changes, shock, and vibration
- High charging and discharging efficiency
- High power density
- Can receive any charge which exceeds their stored voltage

The disadvantages are [101], [102]:

- Low energy density: A typical battery can store about 1000 J/cm^3, whereas high performance ceramic capacitors can store 1 to 10 J/cm^3
- High leakage current
- High cost

Recent advances in ultra-capacitor technology make it possible to use ultra-capacitors as the only energy storage device. For instance, a research group from MIT [103] has announced nano-tube-based ultra-capacitors, which can provide energy storage densities comparable to those of batteries.

In 2006, a U.S. patent [97] was issued for an electrical energy storage unit using an ultra-capacitor that has an energy/weight value of about 342 Wh/kg, twice that of Li-ion batteries.

The largest capacitance currently available on the market is 3000 F [104]. Powered by this kind of capacitor, sensor nodes can work for more than 527 days under a 1% duty cycle

with a single initial charge of the capacitor. It is highly possible that in the near future we will witness a paradigm shift from a battery-based to an ultra-capacitor-based design for all kinds of embedded devices. Therefore, it is essential to explore this frontier in advance. Although ultra-capacitor-based designs have many advantages, the energy leakage of ultra-capacitors is high when they reach their full capacity, imposing thus a major challenge.

Leakage Profile Comparison is analysed in [99]. To simplify the comparison against ultra-capacitors, Li-ion batteries are chosen as representatives of the other batteries. The paper provides leakage profile comparisons between Li-ion batteries and a 2000 F ultra-capacitor over a period of 2 months after they are fully charged. For Li-ion battery, the leakage rate is 8% per month. The 2000 F ultra-capacitor has a very high leakage rate (43.8%) during the first month, but low leakage rate (5.26%) during the second month. At the end of the second month, the ultra-capacitor still has 1.9 V of remaining voltage. These results indicate that ultra-capacitors have leakage performance that is comparable to that of batteries when voltage is controlled under an appropriate level. However, ultra-capacitors suffer severe energy leakage when it is charged to the limit.
To investigate leakage of ultra-capacitors, [99] uses seven types of ultra-capacitors ranging from 22 F to 3000 F. After an ultra-capacitor was fully charged, it was isolated and its remaining voltage was continuously monitored over 1000 hours. The results in [99] conclude that: the leakage power reduces over time after the initial charge and that leakage is more severe for larger ultra-capacitors than for smaller ultra-capacitors (for example, at 2.7 V, the leakage power of a 3000 F capacitor is about 17 times of that of a 100 F).

In terms of correlation between the voltage and leakage of ultra-capacitors, [99] concludes that when the voltage of ultra-capacitors approaches its limit, the value of leakage power increases significantly. For example, when the voltage of the 100 F ultra-capacitor increases to 2.7 V, its leakage power is 8.4 mW, which is equivalent to the power needed for powering a Telos node to work under more than 13% duty cycle. To investigate lifetime difference due to leakage, the nodes are simulated using the empirical data collected. A fully charged 50 F ultra-capacitor powers a MicaZ node at 1% duty cycle. The simulations show that 24% less than the lifetime was obtained.

The lithium-ion capacitor (LIC) is an innovative technology, which is emerging nowadays and merges all the advantages of both lithium-ion batteries (LIB) and EDLC in a single device. These energy storage devices feature higher power density and similar self-discharge rate if compared with the lithium batteries. Furthermore, they have higher cell voltage and higher energy density if compared with super-capacitors [105]. The potential of the LICs in power electronics field is investigated in [98] where authors demonstrate that lithium capacitors are the possible and most cost effective storage devices replacement in applications using flywheel technology. According to Table 3.1 [105], one can see that the energy density of LIC lies in the typical range of batteries, the power density in the range of super-capacitors and confirms that lithium capacitors follow the ideal trend of growth. Moreover, the battery takes about 30% more time to complete the charging phase with respect to the capacitor.

Table 3.1: Performance comparison between LIC and LIB

	LIC	LIB
Power density (W/K_g)	6830	122
Energy density (Wh/K_g)	17	55
Self-discharge ($\%/month$)	2	1

3.3.1.2. Models: Theoretical model as transmission-line

The elementary structure of a super-capacitor, which is based on the double layer capacitor technology, consists of two activated porous carbon-based electrodes. The porous structure of this material allows its surface area to approach two thousand square-meters per gram. The measured capacitance of activated carbon shows a non-linear relationship with their surface area. This results primarily from the porous material used to form the electrodes that cause the resistance and capacitance to be distributed. The electrical response is equivalent to the transmission-line model shown in Figure3.1 [106] with a more accurate illustration of the equivalent circuit of the super-capacitor. Hence, according to [106], the super-capacitor theoretical model can be treated as a transmission line with voltage dependent distributed capacitance.

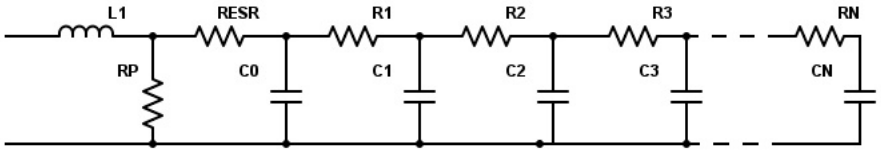

Figure 3.1: Exact scheme of a super-capacitor

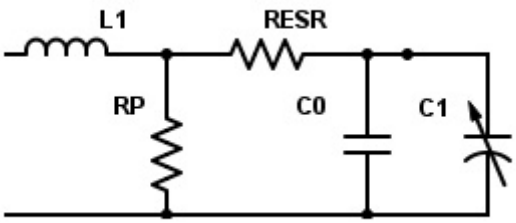

Figure 3.2: Simplified scheme of a super-capacitor

The classical equivalent circuit model illustrated in Figure3.2 [106] is the simplest of the super-capacitor models and can adequately describe the capacitors performance in slow discharge applications (in the order of a few seconds), being used to describe the terminal behaviour of the super-capacitor.
In this model, R_{ESR} is the equivalent series resistance that contributes to the energy loss during charging and discharging of a super-capacitor, while R_p is the equivalent parallel resistance that simulates energy loss due to super-capacitor self-discharge. Resistor R_p is

always higher than R_{ESR} and can be neglected during **fast** charge/discharge. L is an inductor and results primarily from the physical construction of the super-capacitor and it is usually very small.

In [106] a detailed description is given of how the charge and discharge voltage is obtained. Below, the terminal voltage when charging, respectively discharging a super-capacitor is given:

$$v_t(t) = v_r(t) + v_c(t), \tag{3.1}$$

$$v_t(t) = v_c(t) - v_r(t), \tag{3.2}$$

where $v_r(t) = ke^{\frac{1}{R_{ESR}C_{total}}}$ and $v_c(t) = q/C_{total}$. R_{ESR} is the total equivalent series resistance (for all the super-capacitor cells), q is the charge and C_{total} is the total capacitance for all the super-capacitor cells. Also, a relationship between efficiency and discharging time is established from the experimental results [106]:

$$\eta_{eff} = e^{\frac{-2R_{ESR}C_{total}}{t_{dch}}}. \tag{3.3}$$

3.3.2. Super-Conductive Magnetic (SCM)

SCM is a form of storage technology, which stores the energy in form of a Direct Current (DC) magnetic field by passing current through a super-conductor. Operating at cryogenic temperature, the super-conductor virtually has no losses as it produces the magnetic field. SCM has four main parts: Superconducting Coil with Magnet, the power conditioning system (PCS), the Cryogenic System (CS) and the control unit (CU). Detailed description of these parts is given in [107].

The super-conducting coil is the heart of the system which stores energy by generating a magnetic field. The amount of the energy stored is largely dependent on size and geometry of the coil and the characteristics of the conductor [107]. SCMs have a different mechanism of charging and discharging than other technologies. Charging is done by producing a positive voltage across the coil which in turn increases the current. On the other hand discharging is done by adjusting the electronics to appear as load across the coil which in turn produces a negative voltage. This adjustment is provided by the electronics in the PCS. Moreover, it is important to maintain the temperature of the coil low to ensure the super-conducting state. Commercially SCM temperatures are about 4.5 K. CS is used to maintain such sufficiently low operating temperature of the coils. The CU is responsible to link the grid power demand and the power flow to and from the coils as well as measuring the condition of the coils, refrigerator and other equipment parts.

SCM energy storage devices have three operating modes [108]: charging, discharging and stand by. In charging mode, the storage absorbs energy from the power system to the superconducting coils. Whereas, in discharging mode, the coil discharges the stored energy into the DC link capacitor. During stand by mode, the DC circulate efficiently in a closed loop inside the coil. Circulation of the current for longer periods enable storing large amount of energy with no loss. Thyristor controlled configuration of a SCM device is shown in Figure 3.3.

The DC voltage V_{sm} varies between positive and negative values according to charging and discharging processes. The amount of energy stored in the Superconducting Magnetic Energy Storage (SMES) is experessed by Eq. 3.4. Interested readers can refer to [108] for more relationship formulas that characterise the operation of SCM energy storage.

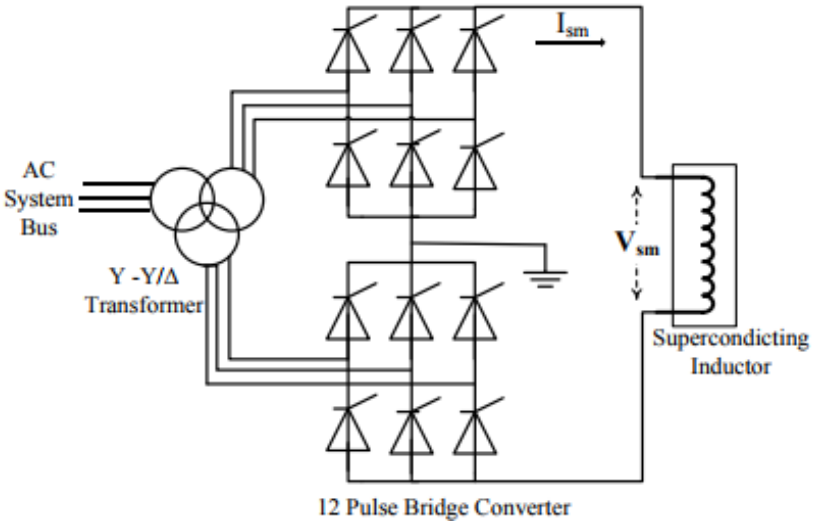

Figure 3.3: SMES Unit Configuration [108]

$$W_{sm} = W_{sm0} + \int_{t_0}^{t} P_{sm} dt, \tag{3.4}$$

where: W_{sm0} is the initial energy stored in the inductor.

3.3.3. Conclusion

The electrical scheme model of the super-capacitor analysed in [106] has as an output the charge and discharge profile of a super-capacitor. The model is given in an analytical form, implemented in simulation and validated in experiments using the Maxwell 48V series capacitor. Hence, the proposed electric model can be used in designing a voltage controller and in sizing a super-capacitor for storage application. Similar models can be found in [109] and [71], where RC circuits are used to model a super-capacitor, proving to be accurate representations of a super-capacitor behaviour.
SCM technologies while presenting interesting characteristics suffer from the conditions required to induce super-conductivity (very low operating temperature). Maintaining such conditions often requires a lot of energy, which will limit the uses of SCM technologies to big installations.

3.4. Electro-chemical Energy Storage

The electro-chemical battery storage technology stores the electrical energy in the form of chemical energy. It is one of the oldest storage system for electricity, and the most common system used to store energy in telecommunication sites [93].

There exist many types of battery and a lot of researches are focusing on new ways to increase the energy density and prolong the battery life. The most important parameters used to describe a battery are:

- Faradic efficiency = Discharged capacity [Ah] / Recharge capacity [Ah]
- Energy efficiency = Discharge energy [Wh] / Recharged energy [Wh]
- Energy density (per volume) = Nominal or Discharged energy [Wh] / Volume of the battery [l]
- Energy density (per weight) = Nominal or Discharged energy [Wh] / Weight of the battery [kg]

The energy density increases with temperature and decreases with the discharge rate. Batteries with aqueous electrolyte can be divided into two groups:

- Batteries with acid electrolyte, such as the lead acid battery
- Batteries with alkaline electrolyte, such as Ni-Cd and Ni-MH batteries

In these batteries, there are secondary reactions that reduce their efficiencies. Typical batteries characteristics are described in [93].

3.4.1. Macro-scale Batteries

Macro-scale battery can be of two types: primary (non-rechargeable) and secondary (rechargeable). Primary batteries have lower initial cost, but secondary batteries can be used in combination with the energy harvesting from the ambient sources.

The main interest of electro-chemical macro-scale batteries is energy density which is the amount of energy stored in a given system or region of space per unit volume [99]. Comparison of energy density for the primary and secondary batteries are presented in [100]. Usage of some batteries can also be limited taking into account safety reasons and usage conditions.

3.4.1.1. Lead-Acid

3.4.1.1.1 Overview

Lead-acid batteries are one of the more economical options for energy storage in renewable energy generation and they are currently the most common energy storage devices. These batteries can be used for both short-term applications (seconds) and long-term applications

(up to 8 hours).

Lead-acid batteries are made with lead based electrodes and, in the charged state, lead dioxide as positive active material and sponge lead as the negative one [93]. The electrolyte is a solution of sulphuric acid and the electrodes are electrically insulated by a separator with ionic conductivity.

The average DC-DC efficiency of a lead-acide battery ranges from 75% to 85% during normal operations, with a life of 250-1000 cycles, depending on the depth of discharge (DoD) [110].

Lead-acid batteries have very low energy density per volume and weight which is combined with relatively high self-discharge rate and not high amount of the duty-cycles making these batteries not suitable for small devices.

3.4.1.1.2 Modelling

Authors of [111] use a AP-12220EVNB module as the battery chosen for tests. Measured capacity is 19.7Ah.

The lead-acid battery is modelled by a single internal resistance. The open circuit voltage OCV is assumed to have a linear relationship with the State of Charge (SOC).

The relationship between the total internal resistance and SOC of the lead-acid battery is approximated by fitting a second-order polynomial as follows:

$$R = a_1 SOC^2 + a_2 SOC + a_3, \tag{3.5}$$

A second-order polynomial is fitted to the OCV as a function of SOC profile as follows:

$$OCV = b_1 SOC^2 + b_2 SOC + b_3. \tag{3.6}$$

The coefficients for these equations are displayed in Table 3.2.

Table 3.2: Polynomial Coefficients for the OCV and R as a function of SOC [111]

a_1	a_2	a_3	b_1	b_2	b_3
0.098	-0.12	0.061	-0.56	2.2	11

3.4.1.2. Nickel Cadmium

3.4.1.2.1 Overview

Rechargeable Nickel Cadmium (NiCd) batteries are one type of alkaline storage battery that uses nickel hydroxide as the positive electrode, cadmium as the negative electrode, and Potassium Hydroxide as alkaline electrolyte used to isolate one electrode from the other. These electrodes are rolled in a spiral shape inside the metal case and tight by the sealing

plate using an insulation gasket as shown in Figure 3.4 [112].

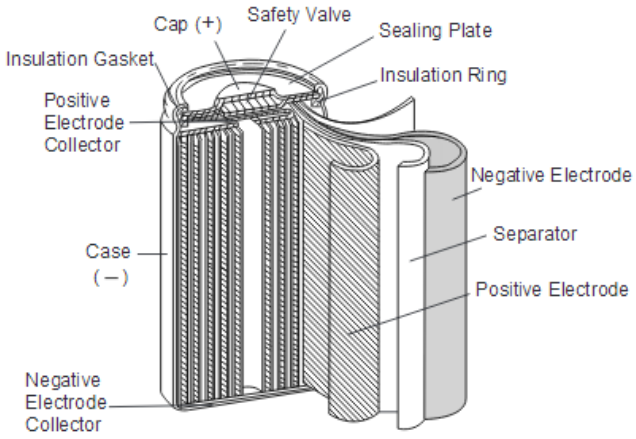

Figure 3.4: NiCd Battery Construction [112]

During the charging operation, electrical energy provided from an external power source (energy harvesting source) is stored as chemical energy in the cell [113]. The charge and discharge characteristics of NiCd batteries are influenced by the current, time, temperature and other factors [113]. Another characteristic of a battery is the cycle life, which is the number of charges and discharges achieved by a battery before the discharge capacity drops to 60% of the nominal capacity under the International Electrotechnical Commission (IEC) specifications. Cycle life varies according to the charge and discharge conditions, the temperature and other usage conditions. In fact, NiCd battery can reach 500 - 1000 cycles with cycling conditions of 0.1C charge and 0.2C discharge [113].

In order to increase the cycle life of the battery, charging control is very important in battery charging. NiCd batteries could be charged using different methods. A detailed description of these methods can be found in [112].

This type of batteries has been successfully used due to their several advantages such as: high number of deep recharge cycles [114], can be ultra-fast charged with little stress, simple storage and transportation, low cost, low internal resistance, high charge and discharge rates, etc [115]. But in the recent years, NiCd batteries are less used because they suffer from memory effect where the apparent discharge capacity is reduced when it is repetitively discharged incompletely and then recharged, causing thus a loss of energy capacity [116]. They also have a low energy density, high self-discharge and the essential element composing the battery (Cadmium) is a toxic metal making the battery disposal problematic [117].

3.4.1.2.2 Modelling

Authors of [118] propose a model based on a Thevenin circuit with two RC parallel branches.

The SoC measuring (or *Ah* counting) is implemented with a simple capacitor. The amount of charge that is introduced or extracted in a battery is calculated by means of measuring

battery current i over the considered period of time Δt. Thus, the state of charge at instant $t + \Delta t$ is defined as:

$$SOC_{t+\Delta t} = SOC_t \pm \frac{\eta}{C_n} \int_t^{t+\Delta t} i.dt.100dt, \tag{3.7}$$

where C_n is the capacity of Capacitor C and η is the efficiency, defined as the amount of charges that cannot be recovered in the charging-discharging processes.

3.4.1.3. Nickel Metal Hydride

3.4.1.3.1 Overview

Nickel Metal Hydride (NiMH) battery technology is the successor of NiCd batteries, and has the same basic structure, with the substitution of Cadmium by Hydrogen at the hydrogen-absorbing negative electrode [119].

As in NiCd batteries, the charge and discharge characteristics of NiMH batteries are also affected by current, time and temperature, and cycle life of NiMH batteries varies according to the charge and discharge conditions, the temperature and other usage conditions. For example, under IEC conditions, these batteries can be charged and discharged for more than 500 cycles [120].

The most common method for recharging NiMH batteries is by using a constant current in the range of 0.5C to 1C (fast charge) since slow charging causes crystalline formation (also known as memory effect), lesser charge efficiency and make the detection of a full charge more difficult [121].

This technology is reasonably mature and has been widely used due to its high energy density (about 50% better than NiCd batteries) [121], low internal impedance (but as low as NiCd batteries) [122], simple storage and transportation, less prone to memory effect which can be reversed by conditioning (fully discharge the battery after charging it) [114], more environmentally friendly (no toxic Cadmium), etc. On the other hand, NiMH batteries suffer from very high self discharge rate [115], charge/discharge rate lower than NiCd, low overcharge tolerance [121], short cycle life and more expensive [117], etc.

NiMH batteries have a high discharge rate (in general a nickel based cell loses 10-15% of its capacity within the first 24 hours, then they discharge 10-15% per month). Therefore they are not very good for long term deployments and storing low amounts of harvested energy [114].

3.4.1.3.2 Modelling

The Equivalent electronic network model in [123] is based on the macroscopic description of the fundamental electro-chemical and physical processes occurring inside the battery systems. Figure 3.5 represents the electronic network model for a NiMH battery. This model takes into consideration two different domains: electrical and chemical, separated by an

ideal transformer.

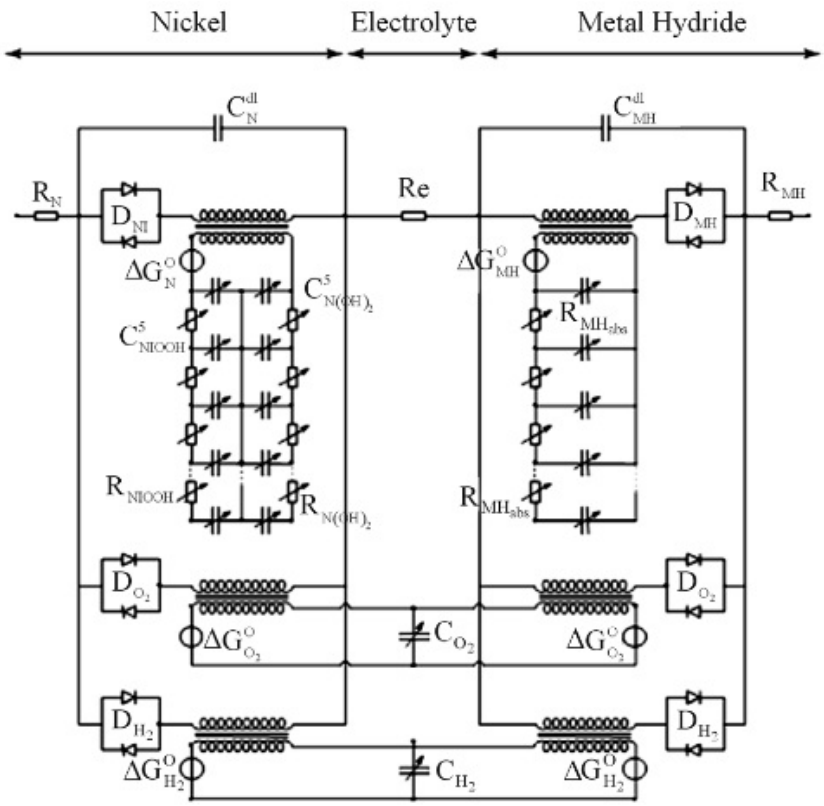

Figure 3.5: Electronic network model for NiMH battery [123]

The electrical double-layer capacitances C^{dl} model the energy storage in the electrical domain, which is physically the result of charging the solid electrodes in contact with the ionic electrolytes. Each electro-chemical-to-chemical transition is modelled by an ideal transformer in series with two anti-parallel diodes representing the redox reaction.

3.4.1.4. Lithium-ion

3.4.1.4.1 Overview

Lithium is the smallest and lightest metallic element. Compared to the standard hydrogen electrode, it has the most negative electro-chemical potential making it the most electroactive metal. Lithium-ion cells typically use a carbon based anode. Various Li-based compounds offering different characteristics and electro-chemical performance can be used for the cathode. The electrolyte is usually a lithium salt dissolved in a non-aqueous inorganic solvent [124].

The popularity of the Li-ion batteries is due to the advantages they offer such as: high energy density, high voltage (three times of NiMH batteries), low self discharge rate, does not suffer from memory effect, long cycle life (twice of NiMH batteries), small size, low internal resistance, environmentally friendly, high duty cycles, etc [125–127]. Despite all these

advantages, Li-ion batteries are more expensive, need special safety precaution because Lithium is chemically reactive, require regulations to transport [117].

3.4.1.4.2 Modelling

The Internal Resistance (IR) Model presented in [128] and shown in Figure 3.6 implements an ideal voltage source V_{OC} that represents the Open Circuit Voltage (OCV) of the battery, and an ohmic resistance describing the internal resistance.

The battery terminal voltage V_{Batt} is given by the following equation:

$$V_{Batt} = V_{OC} - R_0 i_{Batt} \tag{3.8}$$

where i_{Batt} is the battery output current with a positive value when discharging, and a negative value when charging.

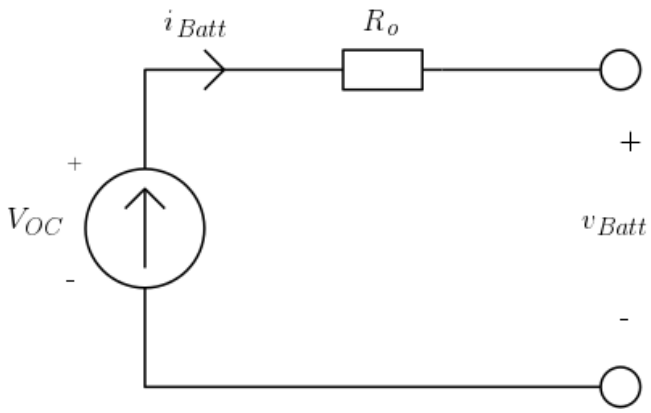

Figure 3.6: IR Model [128]

The One Time Constant (OTC) Model in [128] adds a parallel RC network in series to the internal resistance R_0 of the IR model, in order to approximate the dynamic behaviour of the lithium-ion battery. As shown in Figure 3.7, this model consists of three parts including the voltage source V_{OC}, the ohmic resistance R_0, and (R_{OTC} ,C_{OTC}) used to describe the battery transient response during charging or discharging.

The electric behaviour of the OTC model can be expressed by the following equations:

$$\dot{v}_{OTC} = \frac{-1}{R_{OTC}C_{OTC}} v_{OTC} + \frac{1}{C_{OTC}} i_{Batt}, \tag{3.9}$$

$$v_{Batt} = V_{OC} - v_{OTC} - R_0 i_{Batt}, \tag{3.10}$$

where v_{OTC} is the voltage across C_{OTC} and $\dot{v}_{OTC}$ is the first derivative with respect to time.

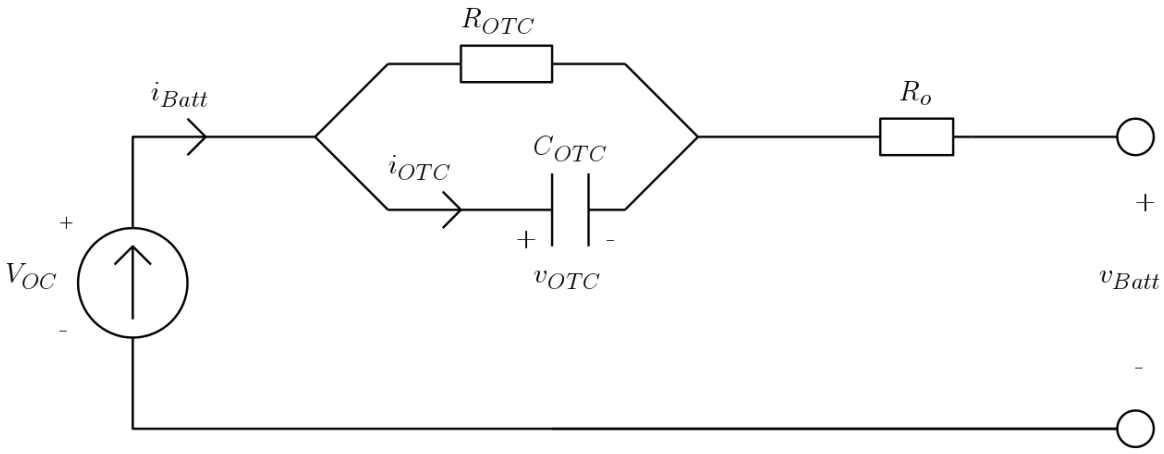

Figure 3.7: OTC Model [128]

Two Time Constant (TTC) Model: the dynamic characteristics of the battery cannot be represented very accurately by the OTC model, since its output voltage shows a big difference between the short-time and the long-time transient behaviour when the battery output current is zero (no load).

To improve the flexibility of the OTC model, an extra RC network is added in series to the OTC circuit to get the TTC circuit model [128]. As shown in Figure 3.8, this model is composed of four parts: voltage source V_{OC}, ohmic resistance R_0, (R_{TTC1},C_{TTC1}) to describe the short-term characteristics and (R_{TTC2},C_{TTC2}) to describe the long-term characteristics.

The electric behaviour of the TTC circuit model can be expressed by the following equations:

$$\dot{v}_{TTC1} = \frac{-1}{R_{TTC1}C_{TTC1}} v_{TTC1} + \frac{1}{C_{TTC1}} i_{Batt}, \tag{3.11}$$

$$\dot{v}_{TTC2} = \frac{-1}{R_{TTC2}C_{TTC2}} v_{TTC2} + \frac{1}{C_{TTC2}} i_{Batt}, \tag{3.12}$$

$$v_{Batt} = V_{OC} - v_{TTC1} - v_{TTC2} - R_0 i_{Batt}, \tag{3.13}$$

where v_{TTC1} and v_{TTC2} are the voltages across C_{TTC1} and C_{TTC2}, respectively.

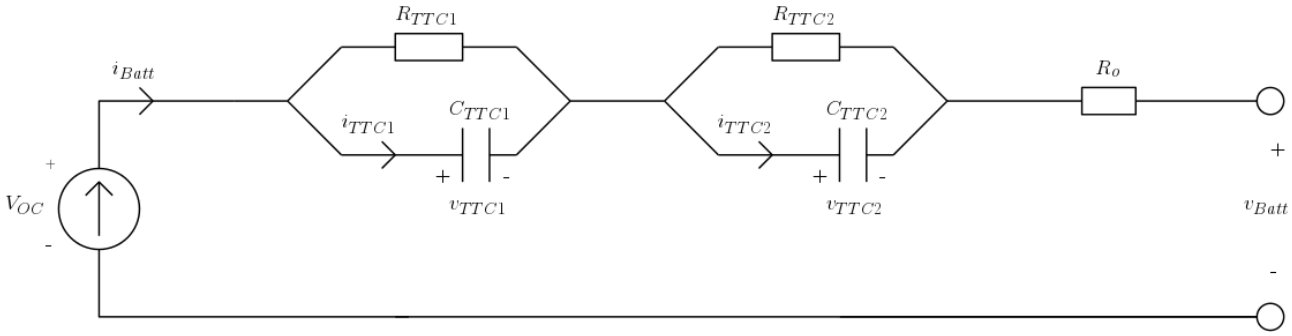

Figure 3.8: TTC Model [128]

The Equivalent electronic network model: for Li-ion batteries presented in [123] is shown

in Figure 3.9 and is essentially very similar to that of NiMH.

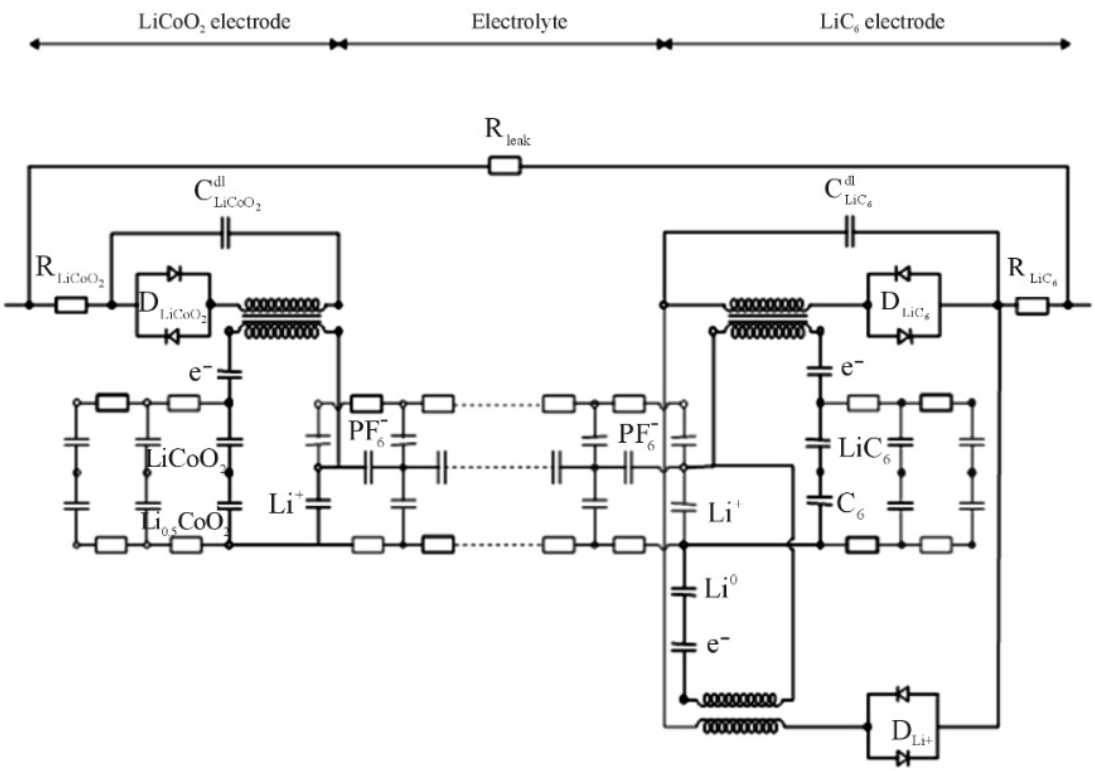

Figure 3.9: Electronic network model of Li-ion battery [123]

$LiCoO_2$ and LiC_6 electrodes are presented on the left-hand side and the right-hand side of Figure 3.9, respectively. The two electrodes, separated by the electrolyte, are represented by a double layer capacitances (C^{dl}) in the chemical domain together with the diodes (D_i) representing the charge transfer reactions and the ohmic resistances (R_i) inside both electrodes.

3.4.1.5. Generic dynamic model

A general model is presented in [129], as shown in Figure 3.10 describe the charging and discharging process of all above batteries.

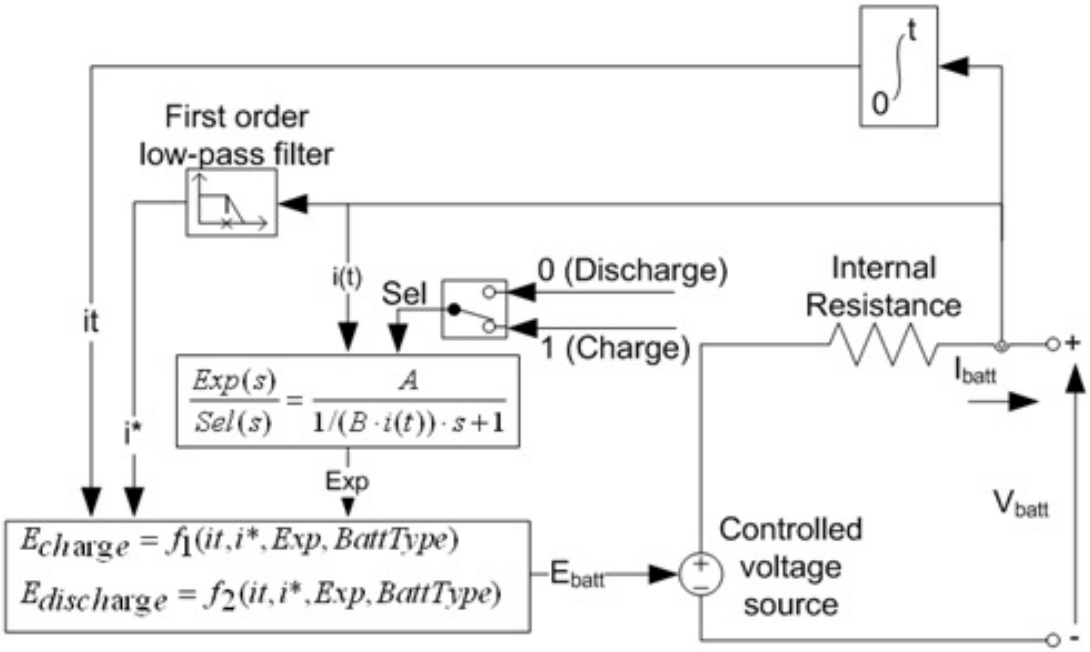

Figure 3.10: Generic dynamic model [129]

A typical discharging curve of a battery is given in Figure 3.11.

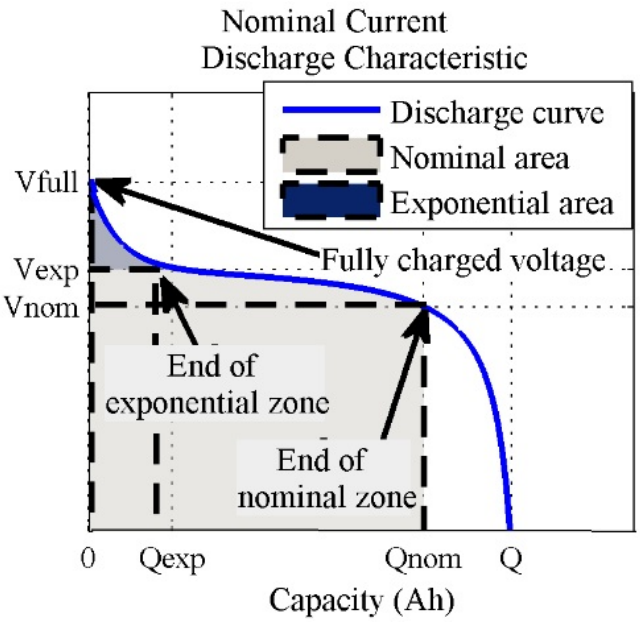

Figure 3.11: Typical discharging curve of a battery [130]

As it is shown in Figure 3.11, the battery has two discharging regions: nominal area under which the battery operates normally, and the exponential area in which the battery voltage decays exponentially.

The charging and discharging models for each type of the batteries are summarised in the following.

- **LA**
  - Discharge: $V_{batt} = E_0 - Ri - K\frac{Q}{Q-it}(it + i^*) + B|i(t)|.[-exp(t) + Au(t)]$,
  - Charge: $V_{batt} = E_0 - Ri - K\frac{Q}{it-0.1Q}i^* + K\frac{Q}{Q-it}it + B|i(t)|.[-exp(t) + Au(t)]$,
- **NiCd**
  - Discharge: $V_{batt} = E_0 - Ri - K\frac{Q}{Q-it}(it + i^*) + B|i(t)|.[-exp(t) + Au(t)]$,
  - Charge: $V_{batt} = E_0 - Ri - K\frac{Q}{|it|-0.1Q}i^* + K\frac{Q}{Q-it}it + B|i(t)|.[-exp(t) + Au(t)]$,
- **NiMH**
  - Discharge: $V_{batt} = E_0 - Ri - K\frac{Q}{Q-it}(it + i^*) + B|i(t)|.[-exp(t) + Au(t)]$,
  - Charge: $V_{batt} = E_0 - Ri - K\frac{Q}{|it|-0.1Q}i^* + K\frac{Q}{Q-it}it + B|i(t)|.[-exp(t) + Au(t)]$,
- **Li-ion**
  - Discharge: $V_{batt} = E_0 - Ri - K\frac{Q}{Q-it}(it + i^*) + Aexp(-B.it)$,
  - Charge: $V_{batt} = E_0 - Ri - K\frac{Q}{it-0.1Q}i^* + K\frac{Q}{Q-it}it + Aexp(-B.it)$,

where

- V_{batt} is the battery voltage (V),
- E_0 is the battery constant voltage (V),
- K is the polarisation constant (V/Ah) or polarisation resistance (Ω),
- Q is the battery capacity (Ah),
- $it = \int idt$ is the actual battery charge (Ah),
- A is the exponential zone amplitude (V),
- B is the exponential zone time constant inverse $(Ah)^{-1}$,
- R is the internal resistance (Ω),
- i is the battery current (A),
- i^* is the filtered current (A),
- $u(t)$ is the charge or discharge mode.

3.4.1.6. Sodium Sulphur (NaS)

Sodium-sulphur batteries have three times the energy density of Lead-Acid ones, a longer life span, and lower maintenance. These batteries are made up of a cylindrical electrochemical cell that contains a molten-sodium negative electrode and a molten-sulphur positive electrode. The sodium-sulphur cells operate only at high temperatures (300 °C to 350 °C). Both electrodes are in a liquid phase, while the separator is in a ceramic form. The applicability in telecommunication area needs to be studied [93].

The most important factor to consider in order to accurately model the NaS battery are: internal resistance, service life, temperature, electromotive force and depth of discharge [131].

The internal resistance consists of the ohmic resistance associated with electrolyte resistance, plate resistance and fluid resistance, and the resistance associated with the polarisation effect. The internal resistance varies depending on the depth of discharge and temperature. Furthermore, its value also varies due to the life cycle resistance that depends on the number of the charge-discharge cycle already experienced by the battery. In particular, the internal resistance increases as the number of charge-discharge cycle increases. This factor is important as it determines the remaining available maximum pulse power and voltage output of a NAS battery.

The effect of temperature on the internal resistance is very important as it determines the limit to the battery's peak power output.

The electromotive force (EMF) of NaS battery depends mainly on the depth of discharge. Due to the composition reaction, the EMF of NaS battery is relatively constant but drops linearly after 60-75% depth of discharge. In practice, NaS battery is limited to discharge to less than 100% of its theoretical capacity.

The depth of discharge represents the capacity left in the battery. It is related to the internal resistance change, temperature and battery's EMF level.

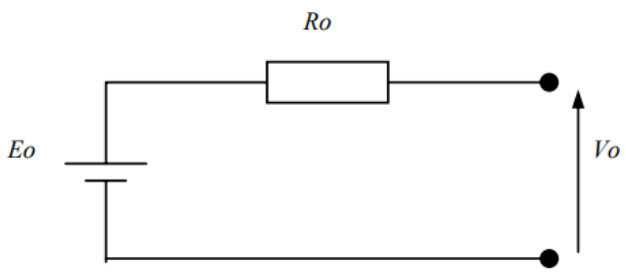

Figure 3.12: Simple NaS battery model [131]

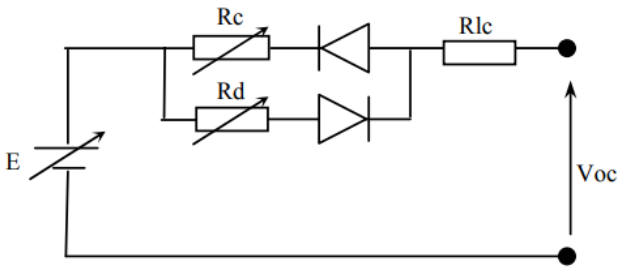

Figure 3.13: Modified NaS battery model [131]

The most commonly used battery model is shown in Figure 3.12. Since NaS battery's internal resistance varies with temperature and depth of discharge, this model is not accurate and can only be applied in simplified case studies where the energy from E_0 is assumed to be unlimited.

The modified model, depicted in Figure 3.13, is still simple but yet meets most of the requirements for modelling the NaS battery.

In particular, it takes into account the non-linear battery element characteristic during charging and discharging as well as the internal resistance which depends on the temperature changes and depth of discharge of the battery.

3.4.1.7. Sodium-Nickel Chloride

It consists of nickel-chloride as positive electrode and works at very high temperature (300 °C) without cooling.

To represent the main characteristics of sodium-nickel chloride, a model based on an equivalent circuit is proposed in [132]. The model is based on parallel RC branches. However, large number of RC branches will increase model complexity though they provide better accuracy. It is shown that a model with two RC branches is considered as a better compromise between accuracy and complexity [133]. Using these guidelines, a two RC branch model is shown in Figure 3.14.

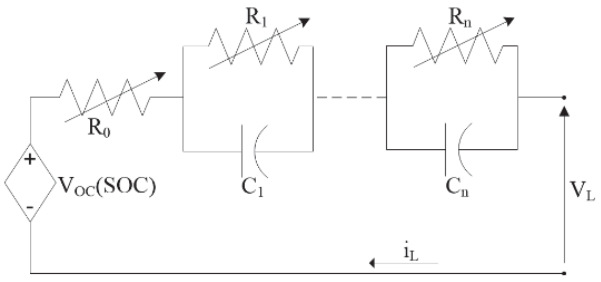

Figure 3.14: Equivalent circuit model of Sodium-Nickel Chloride [132]

In particular, the first branch elements (R1 & C1) characterise the fast electro-chemical dynamics whereas the second branch elements (R2 & C2) characterise the slower electro-

chemical dynamics such as diffusion of electrolytes. The relationship among the parameters of the model and how they influence the state of charge is provided in detail in [132]. Moreover, an experimental comparison of the model simulation and actual measured battery values shows a reasonable match confirming that for most practical applications, a two parallel RC branches model provides a reasonable balance between accuracy and complexity.

3.4.2. Micro-scale Batteries

Reducing the battery size to fit in small devices as well as increasing the lifetime of it became one of the research purposes [134]. Micro-scale batteries are mainly designed as: micro-sized, solid thin film, flexible and 3D using battery technology lithium (great majority) and non-lithium.

Solid state thin film battery have high energy densities, good capacity retention for thousands of charge and discharge cycles, and an extremely low self-discharge rate. Batteries fabricated using the crystalline $LiCoO_2$ cathode consistently provide the maximum power levels up to 30 mW/cm^2, long cycle life, negligible self-discharge and rapid charge rates. Similar good results have been obtained with crystalline $LiMn_2O_4$ cathodes. These cathodes can be used with Li-free or Li-ion thin-film anodes to produce batteries. The design of such a battery is presented in Figure 3.15, where a primary thin film Lithium battery can be placed into a chip [135].

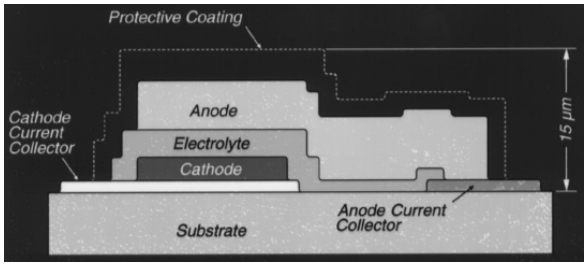

Figure 3.15: Micro-sized battery chip [135]

Thin film batteries have the size about 1 mm^2 and can be minimised by using the 3D structure [134]. The example of 3D battery is demonstrated on the Figure 3.16b where three-dimensional nickel-zinc rechargeable micro-battery is designed and fabricated with post size $50 \times 40mm$ and foot print area $5 \times 5mm^2$. It is admitted that 3D designs would not trade energy density for power density if the electrodes are made longer rather than thicker.

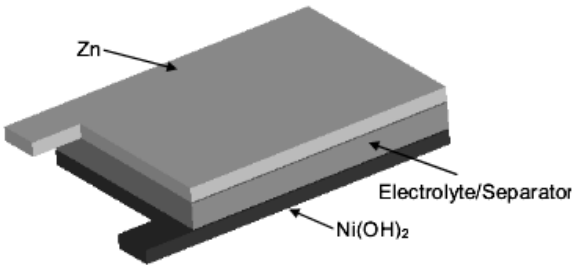

(a) 2-D thin-film micro-battery

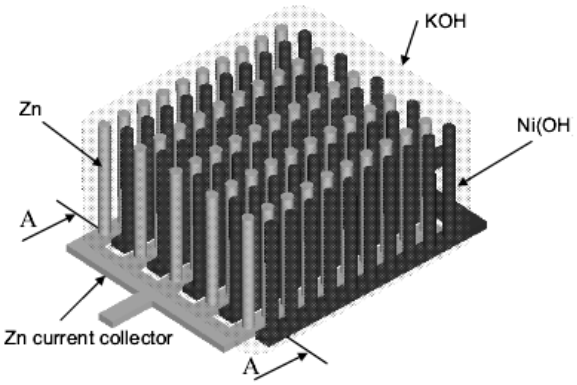

(b) 3-D post-electrode micro-battery

Figure 3.16: Comparison of 2D and 3D microbatteries [134]

According to [136], 3D batteries can have the following types of architecture: array of interdigitated (the arrays are periodic) cylindrical cathodes and anodes; interdigitated plate array of cathodes and anodes; rod array of cylindrical anodes coated with a thin layer of ion-conducting dielectric (electrolyte) with the remaining free volume filled with the cathode material and aperiodic ”sponge” structure.
3D batteries have following advantages in comparison with the thin film 2D batteries [136]:

- Larger anode and cathode surface
- Possibility to achieve large energy capacity without loosing power density
- Less sensitivity to ohmic losses (the distance that ions must be transported in discharging in 2D is 350% larger than in 3D)
- The energy capacity per total cell volume in fact is less than in 2D batteries but can be increased without increasing the footprint area
- Energy per unit area in 3D is higher than in 2D batteries

3.4.2.1. Models

Thin film cells consist of thin currents collector, depositing layer of the lower electrode, electrolyte, upper electrode and a second current collector to form the battery [137]. Ohmic drop in the electrolyte/separator layer is the main thin film power limitation. Increasing the separator thickness decreases the maximum power. The maximum power is calculated per footprint area (P_A): resistance (R) area product (A). It is illustrated in Figure 3.17.

$$R \cdot A = \frac{L_s}{\sigma_i}, P_A \frac{V_{OC}}{2} \cdot \frac{V_{OC}}{2RA} = \frac{\sigma_i V_{OC}^2}{4L_s}, \tag{3.14}$$

where σ_i is an ionic conductivity, A is a footprint area and L_s is a separator thickness.

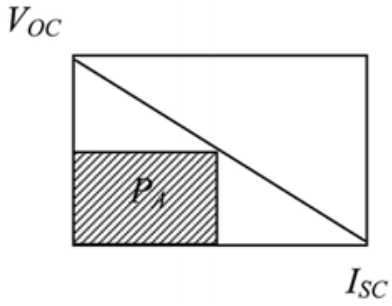

Figure 3.17: Maximum power calculation: I_{SC} - half the short circuit current, V_{OC} - Ohmic loss (half of the open circuit voltage) [137]

According to this formula, the energy per footprint increases with thickness of the cathode, which leads to slow diffusion in the electrode. From this, the maximum power can be calculated with Fick's law on base of diffusion coefficient of lithium in the solid materials. This defines the shortest discharge time and maximum power density. Reducing the electrode thickness compensates the reduction of the electrolyte conductivity, but on the other side it leads to reduction of energy density per footprint. For applications demanding high power density, the solution is to construct a thick cell with the short ionic current path between two electrodes (3D micro-batteries).

In [138], 3D-micro-batteries are modelled in order to achieve uniform electro-chemical activity. The objective function in the optimisation problem is based on the current density of the electrolyte. The density is correlated to the ionic conductivity (concentration).

The objective function states as:

$$minimise \quad F(\emptyset) = \sqrt{j_x^2 + j_y^2 + j_z^2} d\Omega, \tag{3.15}$$

$$subject \quad to \quad \int_\Omega H(\emptyset) d\Omega = V^*, \tag{3.16}$$

where V^* is volume of the electrode. Constraint is presented by Heaviside function and limits the size of the battery electrode. Otherwise, the electrode can occupy a whole battery cell volume.

3.4.3. Flow batteries

Basically, in flow batteries, two charged electrolytes separated by a membrane are pumped to the cell stack where a chemical reaction occurs, allowing current to be obtained when required [110]. Flow batteries store energy directly in the electrolyte solution for longer cycle life, and quick response times. Different categories exist and are discussed in the following.

3.4.3.1. Redox Flow Batteries

3.4.3.1.1 Overview

This type of energy storage devices falls into the electro-chemical energy storage devices due to the fact that it is based on redox reactions for energy storage in electrolyte solutions

which flow through a battery of electro-chemical cells. During discharge phase, an electron is released from the anode via oxidation process, and it moves to the cathode creating a potential difference. It is accepted via the reduction process. The power delivered by the electro-chemical device is the product of the total current and total voltage developed in the electro-chemical cells. The amount of energy stored is determined by the total amount of active chemical available in the volume of electrolyte solution present in the system.

3.4.3.1.2 Modelling

Following the lack of existing storage models related to flow batteries, the general models are proposed in [139], where the key battery characteristics that contribute in the design of storage systems are stated. This includes battery capacity, battery voltage, battery state of charge, depth of discharge, days of autonomy, efficiency, and lifetime of battery. Flow batteries models in the literature are typically complex and into chemistry details. Some good and detailed models for Vanadium Redox batteries can be found in [135] [140]. A numerical model for Polysulphide Bromide batteries can be found in [141].

3.4.3.2. Vanadium Redox (VR)

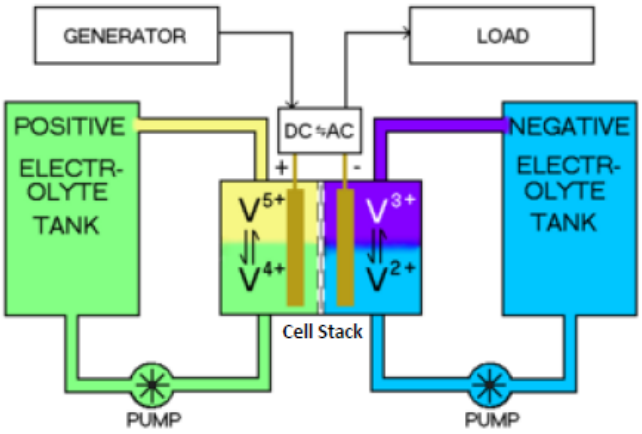

Figure 3.18: Vanadium redox flow battery [110]

VR battery is made up of a cell stack, electrolyte tank system, control system and a Power Conversion System (PCS) as shown in Figure 3.18.

As the battery discharges, the electrolyte flows from their respective tanks to cell stack where H^+ ions are passed between the two electolytes through the permeable membrane. This process induces self-separation within the solution, changing the ionic form of the vanadium as the potential energy is converted into electrical energy. In the charging phase, this process is reversed. During the recharge phase, these batteries operate at normal temperature with an efficiency of 85% [110].

These batteries cannot be fully discharged because this leads to a decrease in performance. When the battery reaches the end of its life, the cell stack can be replaced, while the elec-

trolyte can be reused, having an infinite life. The main characteristics of these batteries are summarised in the following:

- Can operate for 10000 cycles with an estimated life time ranging from 7 to 15 years
- Requires lot of cells in order to obtain the same power output due to low power density
- Offers relatively high cell voltage which is favourable for higher power and energy density
- Fairly expensive ion-exchange membranes required to minimise losses due to cross-membrane transport

Some good and detailed models for Vanadium Redox batteries can be found in [142–144].

3.4.3.3. Poly-sulphide Bromide (PSB)

PSB batteries operate very similarly to VR batteries. The unit is made up of the same components: a cell stack, electrolyte tank system, control system and a PCS.

A numerical model for Polysulphide Bromide batteries can be found in [141].

3.4.4. Micro-fuel cells

Fuel-cells are electro-chemical energy conversion devices that produce Direct Current (DC) electrical power. They differ from batteries due to an external source of fuel and they commonly run on hydrogen. In a standard cell, the fuel is fed continuously to the anode (negative electrode) and an oxidant is fed continuously to the cathode (positive electrode). The use of a catalyst promotes the separation of the electron and the proton in the hydrogen atom.

3.4.4.1. Types of micro-fuel cells

3.4.4.1.1 Hydrogen fuel-cells

use direct pure hydrogen as a source of fuel and oxygen is used as an oxidant. It converts hydrogen into electrical energy and heat through chemical reaction of hydrogen and oxygen into water. The overall reaction is:

$$2H_2 + O_2 \rightarrow 2H_2O + \text{energy}.$$

The advantages of hydrogen fuel-cells are:

- High efficiency.
- Clean and environment friendly.
- Silent operation.
- Modular, i.e., can form stacks according to voltage requirement.

An interesting aspect of hydrogen fuel-cells is that they can be integrated into renewable energy systems in sustainable way without the emission of carbon dioxide. As an example, solar panels, wind turbines or micro-hydro generators can be used to convert radiant ambient energy to electricity. The electricity in turn drives the electrolysis which breaks water into hydrogen and oxygen gases. The produced hydrogen can be used by a fuel-cell.

3.4.4.1.2 Polymer Electrolyte Fuel Cell (PEFC)

The electrolyte in this fuel cell is an ion exchange membrane (fluorinated sulfonic acid polymer or other similar polymer) that is an excellent proton conductor. The only liquid in this fuel cell is water, thus corrosion problems are reduced. The advantages of this type of fuel-cells are shown in the following:

- Solid electrolyte which provides excellent resistance to gas crossover.
- Low operating temperature which allows rapid start-up.
- High current densities of over $2 W/cm^2$.

3.4.4.1.3 Alkaline Fuel Cell (AFC)

The AFC was one of the first modern fuel cells to be developed in 1960. The application at that time was to provide on-board electric power for the Apollo space vehicle. The electrolyte in this fuel cell is Potassium Hydroxide (KOH). It can operate at high temperature ($\approx 250\ ^\circ$C) if the electrolyte is concentrated (85%), and lower temperature ($< 120^\circ$C) when the electrolyte is less concentrated (35 to 50%).

3.4.4.1.4 Phosphoric Acid Fuel Cell (PAFC)

The electrolyte in this fuel cell is concentrated (100%) Phosphoric acid. In this way, the water vapour pressure is reduced, so that water management in the cell is not difficult. It operates typically at high temperature (100 to 220 $^\circ$C).

3.4.4.1.5 Molten Carbonate Fuel Cell (MCFC)

The electrolyte in this fuel cell is usually a combination of alkali carbonates, which is retained in a ceramic matrix of $LiAlO_2$. The fuel cell operates at 600 to 700°C where the alkali carbonates form a highly conductive molten salt with carbonate ions providing ionic conduction. At the high operating temperatures, Ni (anode) and nickel oxide (cathode) are adequate to promote the reaction.

Although a fuel cell is similar to a typical battery in many ways, it differs in several aspects. The battery is an energy storage device in which all the energy available is stored within the battery itself, and it stops providing energy when the chemical reactants are consumed. On the other hand, a fuel cell is an energy conversion device to which fuel and oxidant are supplied continuously.

In the following sections, we summarise the specifications of micro-fuel cells achieved in academia and industry as reviewed in [145]. These achievable specifications may act as relevant models for the purposes of engineering energy harvesting systems.

3.4.4.2. Specifications of micro-fuel cells in literature

In this section we give some typical specifications for micro-fuel cells in the literature.

- **Hydrogen-fed micro-fuel cell** Substrate - Poly-methyl methacrylate; Maximum power density - 315 $mW\ cm^{-2}$.
- **Direct methanol fuel cell** Substrate - Stainless steel; Maximum power density - 65 $mW\ cm^{-2}$.
- **Direct formic acid fuel cell:** Substrate: Silicon wafer. Maximum power density - 30.7 $mW\ cm^{-2}$.
- **Methanol fuel cell** Maximum power density - 10 $mW\ cm^{-2}$.

3.4.4.3. Specifications by different companies

In this section we give the specifications of micro-fuel cells developed by the industry.
Micro-reformed hydrogen fuel cell:

- Ultracell; Maximum power 25W; cartridge duration: 9h and 24h at 20W for 200 and 550 cm^3 volume of cartridge, respectively.
- Casio; Maximum power - 2.5W.
- Seiko Instruments Inc. ; Time of operation: $2-5$h

Direct formic acid fuel cell:

- Korea Institute of Science and Technology;
  Maximum power density: $60 mW\ cm^{-2}$; delivered power : $13.7 W$ (maximum 30W).

Hydrogen fed micro-fuel cell:

- Angstrom Power Inc. ; Maximum power: 2W, time of operation: 6h.
- NTT DoCoMo and Aquafairy Co. ; Maximum power: 2W (800 mAh at 3.6V), time of operation - 5h .
- Hitachi Maxwell Ltd. ; Maximum power: 10W; time of operation : 4-5h.
- Canon Inc. ; Stack power density: $0.2-0.3\ W\ cm^3$, system power density - $0.1-0.15\ W\ cm^3$.

3.4.5. Micro-Heat Engines

Heat engines convert chemical energy into heat and then to mechanical energy that can be used directly for applications such as vehicle propulsion or fluid pumping, or converted into electric power [146]. Interest in micro heat engines arises from their capability to provide high power density supply for micro-systems, available from the combustion of hydrocarbon fuels, which is several orders higher than that of conventional batteries [147]. The energy densities of existing electro-chemical batteries are too low (around 1 kJ/g) to sustain high power needs of some devices for long periods. An attractive alternative to batteries are hydrocarbon fuels, knowing that a typical liquid hydrocarbon fuel holds around 50 kJ/g in its chemical bonds [148]. Besides having a high specific energy, fuels have the ability to be stored for decades without loss of potency.

Nowadays, fossil fuels are the most used energy source for electric power generation, mostly due to the low cost per joule, high energy density (gasoline has an energy density of 12.7 kJ/cm3), abundant availability, storability and ease of transport. In contrast, the miniaturisation of heat engines and power generation approaches based on combustion of hydrocarbon fuels are constrained by the complexity and multitude of components involved. However, the extension of silicon micro-fabrication technology from micro-electronics to micro-electromechanical systems (MEMS) is changing this situation. The initial concept consisted of using silicon deep reactive ion etching, fusion wafer bonding, and thin film processes to micro-fabricate and integrate high speed turbomachinery, with bearings, a generator, and a combustor within a cubic centimeter volume. An application-ready power supply would also require auxiliary components, such as a fuel tank, engine and fuel controller, electrical power conditioning with short-term storage, thermal management and packaging [99].

Expected performance is 10-20 W of electrical power output at thermal efficiencies in the order of 5-20%. Given the relatively large power level, a single micro-engine would only need to operate at low duty-cycles (less than 1% of the time) to periodically recharge a battery [99]. Despite their high power density (0.1-2 W/g) and their high density energy storage for compact, long duration power supplies, micro-engines are not expected to reduce further in size due to manufacturing and efficiency constraints. Thus it will require many years of development before reaching the expected efficiencies and being suitable for wireless sensor network applications [99].

3.4.5.1. Models

Thermodynamic modelling is used to predict thermal efficiency (Carnot limit) in micro-heat engines. It is also used to evaluate performance with different designed parameters.

3.4.5.1.1 Finite heat model

One of the challenges on micro-scale heat engines is isolation of hot and cold sections. Therefore leakage is an important parameters to be considered in the model [149]. The model assumes the finite heat input and includes leakage conductance and additional source conductance.

The merits of performance of micro-heat engines are power and power density. The power density is important for applications concerning mobility, weight and space. As weight is proportional to volume, the power density is calculated as the maximum power divided to the volume and equivalent to the maximum power divided to weight unit. For introduced thermoelectric model, the power density calculation is as following:

$$Power\ density = \frac{\dot{W}}{(A + A_0)(L + L_0)}, \tag{3.17}$$

where A and A_0 are cross-sectional area of micro-heat engine and additional area due to the leakage conductance, respectively. L and L_0 are length of micro-heat engine and additional length due to the source conductance, respectively. $\dot{W}$ is the work rate (power).

The maximum power is an important characteristic of a micro-heat engine. It represents the limits which should be predicted and optimised according to some key parameters such as thermal conductivity of an engine construction material, length scale and hot side temperature:

$$\dot{W_{MAX}} = K_H K_S \frac{\left(\sqrt{K_S T_H + K_L T_C} - \sqrt{K_S T_C + K_L T_C}\right)^2}{K_S K_H + K_S K_C + K_H K_L + K_C K_L + K_H K_C}, \tag{3.18}$$

where K_S, K_H, K_C and K_L are the thermal conductance of source, engine hot side, engine cold side and leakage, respectively. T_H and T_C are the temperatures of hot side and cold side.

The larger length scale, the larger the power output generated without any leakage. Decreasing L leads to leakage and K_L/K_S ratio increase. The simulations of the model showed that the power output increases with higher source temperatures.

The goal in designing micro-heat density is to reach high power, high power density and high efficiency. But, unfortunately, these objectives are in trade-off relationship with each other. For instance, the optimal lengths for maximum power and power density are different. To minimise the leakage and thus to increase the maximum power, the length has to be larger, which leads to decrease of power density. The possible way to increase power in this case is to use range of micro-heat engines.

3.4.5.1.2 Membrane based model

Another model is proposed in [150] for silicon micro-technology of micro-heat engine. It is based on bistable buckling membrane (Figure 3.19) to generate the upward and downward driving forces. In this engine, chamber is partially filled by a liquid coolant and the gas bubble consists of liquid coolant's saturated vapour and residual air.

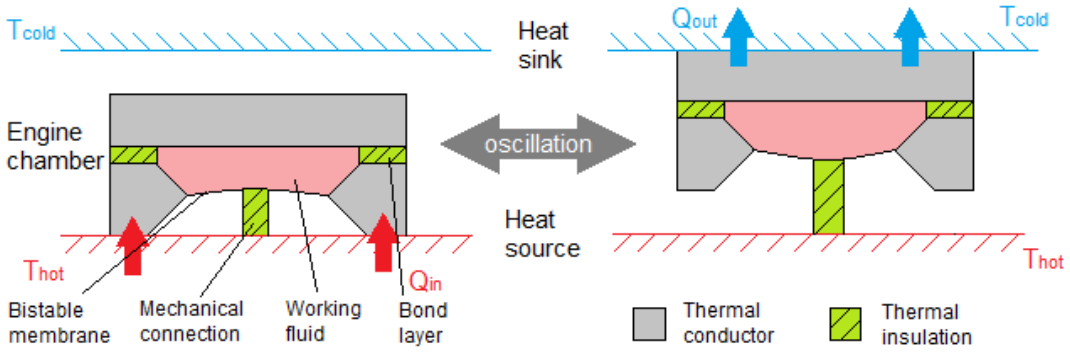

Figure 3.19: Scheme of membrane based micro-heat engine [150]

The output power for such a system is calculated as follows:

$$W_{net} = u_2 - u_1 + u_4 - u_3, \tag{3.19}$$

where u_i is an internal energy calculated for each stage of the system: isochoric heat addition and rejection, adiabatic expansion and compression [140].

The system model is presented in Figure 3.20, where C_{US} is the heat capacity of the upper substrate, C_{wf} is the heat capacity of working fluid, C_{bl} the heat capacity of the bonding layer and C_{ls} is the heat capacity of the lower substrate. R_{wf} and R_{bl} are thermal resistors of working fluid and bond layer. R_{on}/R_{off} is the interface thermal resistivity, when the engine chamber is in contact or not, respectively. S_1/S_2 are switchers of cavity contact with heat source or heat sink, respectively. The temperature difference between heat source and sink is converted into transient temperature difference in the working fluid that performs thermodynamic cycle.

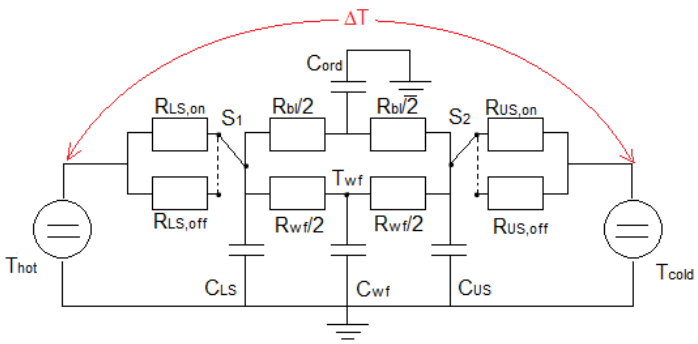

Figure 3.20: Thermal network model [150]

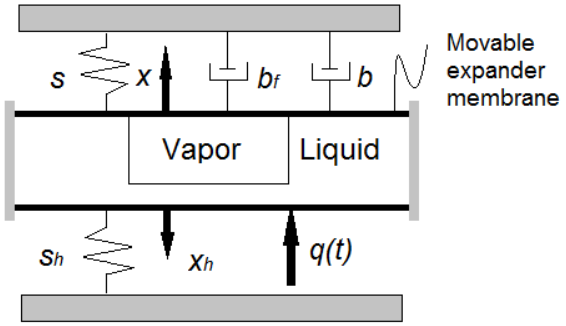

Figure 3.21: Engine schematic mode [151]

Another modelling scheme is proposed in [151] for similar flexing membrane micro-heat engine, operating on two-phase working fluid as shown in Figure 3.21. The engine is fitted in the cylindrical cavity of diameter $2r_o$, thickness h. Liquid in the radial annulus and a saturated vapour bubble (radius $2r_i$) are fitted in the cavity. Movable rigid expander is occupied

by a spring of stiffness s and two dumpers with coefficient b and b_s . Dumper b_s serves to account for the frictional losses in the engine, while dumper b is used to model useful work harvested by an engine converter. It converts the mechanical power into electrical power.

The model provides the average power over time, generated by dumper volume, evaporation and condensation models, the model of motion of the expander membrane and lower evaporator.

The average power over time generated by the damper can be calculated as following:

$$\Pi = \frac{1}{2} \sum_{k} b \left| Q_k \Gamma(f_k) \right|. \tag{3.20}$$

Conversion of mechanical to electrical energy is feasible and equal to 7%, the efficiency of 5-10 % is reachable when thermal inertia is reduced, load is matched to the engine.

3.4.6. Conclusion

In this section, electro-chemical storage technologies were presented. Modelling these batteries can be done using their chemical properties, or using electrical circuits.

Micro-scaled batteries were also considered: thin/thick firm batteries and 3D batteries. For the 3D batteries, the main approach that should be applied for battery design is optimisation of the density current. The approach provides the optimal energy storage configuration. For firm batteries, it was demonstrated, that its main power limitation is the electrolyte/separate layer. The model takes into account the separator thickness, footprint area, ionic conductivity and Omnic losses, calculating the energy and power per footprint. The model is good to define the appropriate battery design for the specific application.

In all considered micro-heat models, the thermodynamic modelling is used. The first model is more common. It includes, leakage and provides the power output and density. The model includes the main micro-heat engine characteristics. The two other models are for more specific types of micro-heat engines: for silicon micro technology and for flexing membrane micro-heat engine.

3.5. Conclusion

In this section, the main types of storage technology have been surveyed. The relevant models use an electrical equivalent circuit, rather than describing the technology using its specific properties, for instance, describing an electro-chemical battery using its chemical properties.

4. Power Consumption Sources

4.1. Introduction

In the modelling of the power consumption of wireless communication networks we isolated four categories of devices:

- Base stations (Section 4.2)
- Core network (Section 4.3)
- Mobile devices (Section 4.4)
- Internet of Things devices (Section 4.5)

For each, a detailed description of the device is given as well as a break down in subsystems, which help us to highlight the characteristics of each type of device. A short review of the literature of models relevant to our work is also given for each device.
The approaches taken and the selection of models in each of the section are based on the needs of the SCAVENGE ESR.

4.2. Base Stations

4.2.1. System Description and Constituting Elements

The characterisation based on the energy consumption of the different parts of a base station is a serious challenge. First of all, there are many different types of base stations: a rough classification can be made between macro base stations and small base stations. The latter, which can present further distinctions, for example in micro, pico or femto cells, have a minor impact on the energy consumption.

A second factor that makes difficult to characterise the energy consumption of a base station is that it is quite infeasible to directly measure the actual consumption for each constituting element. The problem can be overcome using different base station models that list and characterise the elements of a base station according to their power consumption.

There is plenty of works in literature that deal with this problem. For what concern the SCAVENGE project, a major reference is given by the EARTH model in [152]. Its main contribution is to list simply and clearly the fundamental elements of a Base Station (BS) and try to characterise them. Another relevant work is given by [153], which enables a major flexibility in the description of the BS elements, differentiating also the cells based on their size and functionality.

In the next sections we are going to briefly describe the main constituting elements of the base stations, giving an overview of their functionalities and their impact on the total energy consumption.

4.2.1.1. Constituting Elements

A BS consists of multiple transceivers (TRXs), each of which serves one transmit antenna element. A TRX comprises a power amplifier (PA), a radio frequency (RF) small-signal TRX module, a base-band engine including a receiver (uplink) and transmitter (downlink) section, a DC-DC power supply, an active cooling system, and an AC-DC unit (mains supply) for connection to the electrical power grid (Figure 4.1 [154]).

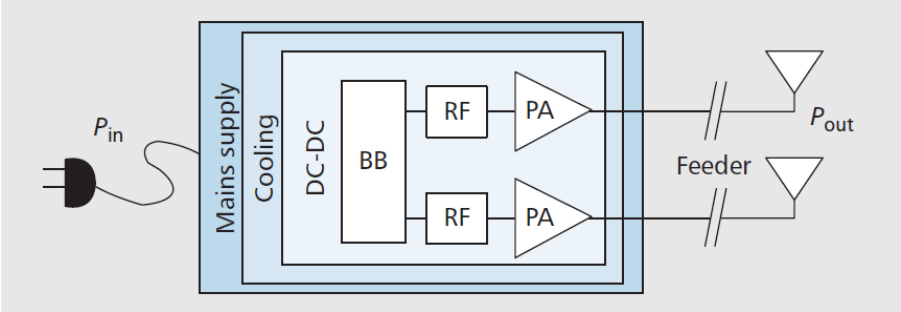

Figure 4.1: Block diagram of a base station transceiver [154] [155]

4.2.1.1.1 Base-Band Unit

In a base station, the base-band unit (BBU) processes the transmitted/received signal in the original frequency without modulation. The base-band unit performs multiple tasks such as filtering, channel equalisation and denoising among others.

4.2.1.1.2 Power Amplifier

The power amplifier, specifically in our case the RF power amplifier, is able to convert a low-power RF signal into a higher power signal. Modern RF amplifiers operate in different classes, achieving different design goals. The typical design goals include gain, power output, bandwidth, power efficiency, linearity, input and output matching, and heat dissipation.

4.2.1.1.3 RF Transceiver

RF Transceiver (RF-TRX) incorporates a Receiver (Rx) and a Transmitter (Tx) for uplink (UL) and downlink (DL) communications. The RF-TRX has vendor-specific architecture, and may differ significantly depending on the BS type. RF transceiver does all the processing at transmitting frequency, modulating, filtering the base-band signal and in our study includes the ADC–DAC.

4.2.1.1.4 Antenna and Feeder

The antenna is the end transmitting element of the base station and is characterised by many parameters, e.g., including: gain, that characterises the directivity of an antenna; radiation pattern, characterises how the antenna radiates in a 3D space; bandwidth; impedance; resonant frequency; polarisation, which is the orientation of the electric field in respect to the

ground; and efficiency, corresponding to the ratio between the emitted power and the power fed to the antenna.

The feeder is a coaxial cable used to feed the signal from the power-amplifiers, often situated at ground-level to the antennas.

4.2.1.1.5 Cooling Equipment

Electronic equipments in the BS can operate in a certain temperature range. In addition, in order to extend life time of the batteries (used for back up) the temperature should be kept at certain level [156], hence, a cooling equipment is employed at BS. It is important to remark that in small base stations (pico, femto) passive cooling techniques are used instead of employing an equipment [157, 158].

4.2.1.2. Power Consumption

Power consumption in base station is a complex problem. Indeed, not only the hardware of the technology (2G, 3G . . .) and the size of the base station (Macro, Small. . .) are the main issues, but there is very little power consumption related to the available traffic. However, literature tends to converge to the shares presented in Figure 4.2, with a distinction between small and macro base stations.

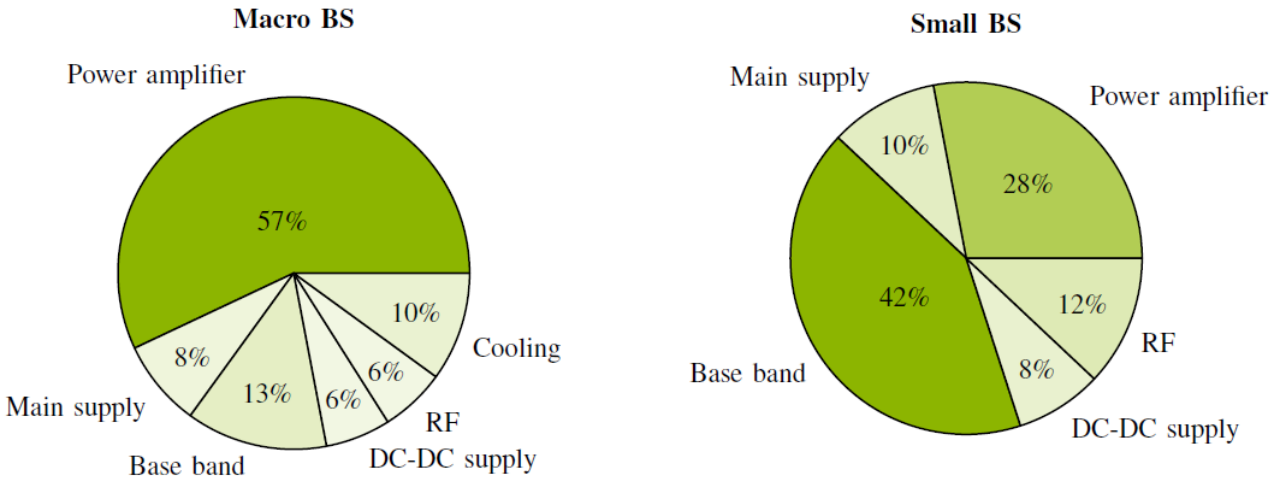

Figure 4.2: Comparison of BS energy consumption [154]

For macro base stations, the main power consumption part relates to the power amplifiers, because of the relatively high transmission of data. In small base stations however the base-band unit represents the biggest share.

4.2.2. Models

4.2.2.1. Load-based Power Consumption

This section surveys some literature works related to power consumption modelling in high power devices, specifically BSs, showing the evolution of the modelling adapting to new

technologies and focusing on load-based analysis for macro and small BSs.

The power consumption of a base station consists of two components: (i) the static power consumed by an idle BS and (ii) the dynamic consumption depending on the BS load.

Some works consider only static power models, such as the 2010 one in [159] where a component-level power model for both GSM and Universal Mobile Telecommunications System (UMTS) macro and micro base stations is proposed. According to the authors, the macro BS power consumption model can be reduced to the static part due to the negligible amount of dynamic consumption for these technologies. Regarding micro base stations, both components should be considered since traffic load has statistically a higher variability and thus power amplifier adaptive control can be applied playing an important role in the BS power consumption.

However, most of the reviewed literature considers power models with both components. A real-data-based power consumption model for both macro and micro BSs is presented in [160] where the power consumption evolution over a day is investigated and the energy efficiency is measured in different scenarios, defined as the power consumption needed to cover a certain area in W/m^2. Moreover, a well-known power consumption model was presented by EARTH project [154] [155]. The project proposes a simplified block diagram of a complete BS (Figure 4.1) that can be generalised to all BS types, including macro, micro, pico and femto BSs.

It provides a BS power consumption model at maximum load and another one at variable load. According to its results, the relations between relative RF output power P_{out} and BS power consumption P_{in} are nearly linear. Hence, the following linear approximation of the power model is provided:

$$P_{in} = \begin{cases} N_{TRX} * (P_0 + \Delta_p P_{out}), & 0 < P_{out} \leq P_{max} \\ N_{TRX} * P_{sleep}, & P_{out} = 0 \end{cases} , \tag{4.1}$$

where P_0 is the linear model parameter to represent the power consumption at zero RF output power (actually estimated using a reasonably low output power, assumed to be 1% of P_{max}), and Δ_p is the slope of the load-dependent power consumption. Parameters for the different BS types are also provided based on 2010 State-of-the-Art as summarised in Table 4.1. Note that EARTH project already foresaw fast deactivation of components in future BSs, i.e., put the BSs into sleep mode when there is nothing to transmit. This could be an important solution to save energy, captured in the model with P_{sleep}.

Table 4.1: Power model parameters for different BS types [155]

BS Type	*NTRX*	P_{max}[W]	P_0 [W]	Δ_p	P_{sleep}[W]
Macro	6	20	130.0	4.7	75.0
RRH	6	20	84.0	2.8	56.0
Micro	2	6.3	56.0	2.6	39.0
Pico	2	0.13	6.8	4.0	4.3
Femto	2	0.05	4.8	8.0	2.9

A very similar approach is used in [161] to obtain the final BS power consumption. Nevertheless, the model in [155] is extended and more detailed equations are provided for the contribution of the power amplifier, antenna, main supply, cooling and base band and radio frequency units. Following this work, an improved model based on realistic environments considering components such as walls, temperature, and component behaviour is presented in [162]. It is claimed that the power consumption model of each component cannot be specified with a single constant due to the existence of correlations between components. Thus, these correlations are reflected under practical assumptions with detailed equations.

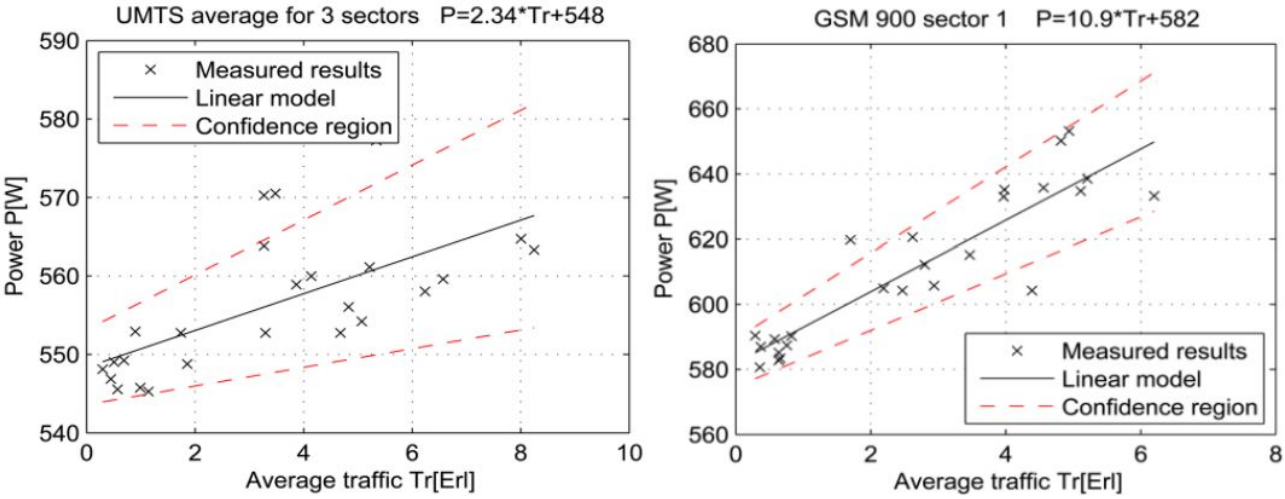

Figure 4.3: Traffic load linear regression model in GSM and UMTS BSs [163]

Accurate models for traffic load in mobile networks are a key factor to properly quantify the overall power consumption. Changes in the instantaneous power consumption of Global System for Mobile Communications (GSM) and UMTS base stations according to their respective traffic load are investigated in [163]. Real data measurements show the existence of a direct relationship between traffic load and BS power consumption. According to this relationship, a linear power consumption model is developed for base stations of both technologies as shown in Figure 4.3.

4.2.2.2. Backhaul Power Consumption

In [164], three different backhaul architectures are considered and are illustrated in Figure 4.4. For each backhaul architecture, the corresponding power consumption model is formu-

lated. The introduced model incorporates all the fundamental devices used in the backhauling. In this section, the backhaul architectures are briefly explained. The parameters used in the architectures are resumed in Table 4.2.

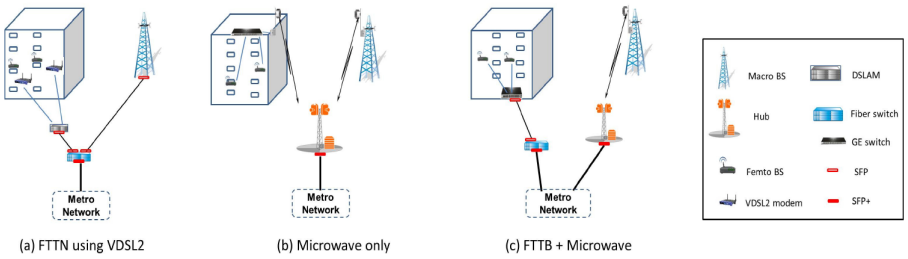

Figure 4.4: Backhaul Architecture [164]

Table 4.2: Notations and Definitions

Notation	Definition
P_{modem}	Power consumption value of VDSL2 modem
N_{femto}	Number of femto BS
N_{DSLAM}	Number of DSLAMs in the area
P_{DSLAM}	Power consumption value of DSLAM
P_{SFP}	Power consumption value SFP
N_s^F	Number of fiber switches in the area
P_s^F	Power consumption value of fibre switch
N_{macro}	Number of macro BS
N_{ul}	Total number of uplink interfaces used to connect toward the MN
N_b	Number of buildings
N_{hub}	Number of hubs
N_s^{MW}	Total number of switches inside the hubs
P_j^{MW}	Power consumption related to microwave backhaul operations
N_{GES}	Number of GESs
P_{GES}	Power consumption of a GES
P_{SFP+}	The power consumption of a SFP+ used to transmit the backhauled traffic toward the MN

4.2.2.2.1 Architecture 1

In the first architecture, very-high-speed Digital Subscriber Line version 2 (VDSL2) modems are used for backhauling of femto-cell BSs. Each femto-cell BS is connected to a Digital subscriber line access multiplexer (DSLAM) using a high speed connection over copper. Further, DSLAMSs and the macro BSs are connected to fibre switches (FSs) through point-to-point optical links. Small form-factor pluggable transceivers (SFPs) are used to receive and transmit the optical signals. The traffic coming from the wireless network is aggregated at FSs before arriving to the metro network (MN). The aggregated data is transmitted over

10Gbps fibre links and enhanced small form-factor pluggable (SFP+) transceivers modules. The power consumption model of the first architecture is given as:

$$P_{bh}^{1} = N_{femto}P_{modem} + N_{DSLAM}(P_{DSLAM} + 2P_{SFP}) + N_s^F P_s^F + 2N_{macro}P_{SFP} + N_{ul}P_{SFP+}, \quad (4.2)$$

4.2.2.2.2 Architecture 2

In the second backhaul architecture, femto-cell BSs are employed in a closed area and connected to a Gigabit Ethernet Switch (GES) using conventional Fast Ethernet Connections. The data traffic coming from the femto-cell BSs is aggregated by the GES before being conveyed to the microwave antenna placed outside the building. Microwave antennas (the antenna of the buildings and the antenna at the micro BSs) are connected to hubs using a point-to-point star topology. Further, hubs are equipped with switches to aggregate the coming traffic before conveying it to MN. The transmission between the hubs and the MN is realised by 10 Gbps optical point-to-point links and SFP+ modules. The power consumption model of the second architecture is given as:

$$P_{bh}^{2} = \sum_{j=1}^{N_{macro}+N_b+N_{hub}} P_j^{MW} + N_{GES}P_{GES} + N_{ul}P_{SFP+}, \quad (4.3)$$

According to [164] P_j^{MW} can be modelled as:

$$P_j^{MW} = \left\{ \begin{array}{ll} P_{low-c}, & \text{if } N_j^{ant} = 1 \\ P_{high-c} + P_s^{MW} \left\lceil \frac{C_j}{C_{switch}^{MW}} \right\rceil, & \text{otherwise} \end{array} \right\}.$$

where N_j^{ant} is the number of antennas at access point j (such as macro BS, antenna device outside the building or hub) , C_j is the rate of the aggregated traffic at access point j, C_{switch}^{MW} and P_s^{MW} are the maximum capacity of a switch inside a hub and its power consumption, respectively. P_{low-c} and P_{high-c} are power consumption values of the microwave antennas at the low and high power consumption regimes, respectively. Hence, the power consumption model P_{bh}^{2} is revised as:

$$P_{bh}^{2} = (N_{macro} + N_b)P_{low-c} + N_b P_{GES} + N_{hub}P_{high-c} + N_{ul}P_{SFP+} + N_s^{MW}P_s^{MW}. \quad (4.4)$$

4.2.2.2.3 Architecture 3

The third backhaul architecture is similar to the second one. The fundamental difference is the connection link between the indoor femto-cell BSs and the MN. First, femto-cell BSs are connected to a GES via Fast Ethernet and then GES is connected to a FS over 1 Gbps optical point-to- point links. To receive and transmit the optical signal SFP transceivers are used. In the end, FSs are connected to the MN via employing 10 Gbps optical links and SFP+ transceivers. The backhaul model between the macro BSs and the MN is identical to the model used in the second architecture. The power consumption model of the third architecture is given as:

$$P_{bh}^{3} = N_b(P_{GES} + 2P_{SFP}) + N_{macro}P_{low-c} + N_s^F P_s^F + N_{hub}(P_{high-c} + P_{SFP+}) + N_s^{MW}P_s^{MW} + N_{ul}P_{SFP+}. \quad (4.5)$$

For further information, the reader can refer to [164–166].

4.2.3. Conclusion

Base station power consumption modelling has been deeply studied so far with a lot of models, general and application-specific. Indeed, it is still an evolving topic since new technologies arise and hence, new more complex models are needed. However, there are current models that already predict future technologies and we believe they are accurate enough for our purposes in this project. Thus, we do not provide any new model proposal in this section.

In the literature, [164] is the most comprehensive work related to power consumption model of realistic backhaul architectures. In particular, it is an important work as it takes into account the affect of the all mid-devices in the introduced consumption models. However, in the analysis of the Heterogeneous Cellular Networks (HCN), the main measure is the total transmission power used by the BSs which is assumed proportional to the amount of data served by the BS. Hence, the consumption model is highly correlated to the structure of the HCN. For instance, when we consider the HCN with cache enabled helper nodes the energy efficiency of the network is directly related to the amount of data offloaded to helper nodes. At this point, we want to remark that the backhaul power consumption is directly related to the network architecture and the considered scenario. In the project, we are particularly interested in on-demand video streaming scenarios in HCN architectures where the local caches are utilised to minimise the backhaul traffic of the small-cell base stations. Hence, as a next step, we will analyse HCN architectures with cache capabilities and the corresponding power consumption models.

4.3. Core Network

4.3.1. Introduction

The Core Network (CN) or Evolved Packet Core (EPC) in the Long Term Evolution (LTE), is the backbone of the mobile network and it provides different services to mobile users who are connected by the Radio Access Network (RAN). It mainly makes use of proprietary equipment, but with the evolution brought by virtualisation technologies, the dependence on such equipment will be minimised in future mobile networks. In this section, we discuss the CN constituents, the system power consumption and power consumption models for virtualisation platform.

4.3.2. EPC Constituents

The EPC network consists of a number of Network Functions (NFs), all interconnected through an IP infrastructure to provide packet data services to the access networks. The EPC carries traffic between the Evolved Terrestrial Radio Access Network (E-UTRAN) Node Bs (eNBs for short) and the Internet on behalf of the User Equipment (UE) using specialised hardware. This includes the Packet Data Network Gateway (PGW), which is responsible for Internet Protocol (IP) address allocation for the UEs, as well as for QoS enforcement and flow-based charging, according to rules from the Policy and Charging Rules Function (PCRF). It is also responsible for the filtering of downlink user IP packets into different QoS-based bearers. The Serving Gateway (SGW) serves as the local mobility anchor for

the data bearers when the UE moves across BSs. It also retains the information about the bearers when the UE is in the idle state (known as EPS connection management) and temporarily buffers downlink data while the Mobility Management Entity (MME) initiates paging of the UE to re-establish the bearers. It also serves as the mobility anchor for interworking with other 3GPP technologies such as the General Packet Radio Service (GPRS) and UMTS. The MME is the control node that processes the signaling between the UE and the EPC, while at the same time authenticating the UE with the Home Subscriber Server (HSS). It is involved in the bearer activation/deactivation process and is also responsible for choosing the SGW for a UE at the initial attach time and at time of intra-LTE handover involving EPC node relocation. The Non-Access Stratum (NAS) signaling terminates at the MME, which is also responsible for the generation and allocation of temporary identities to the UEs. It checks the authorisation of the UE to camp on the service provider's Public Land Mobile Network (PLMN) and enforces UE roaming restrictions. The BS, SGW, and PGW communicate over GPRS tunneling protocols (*GTP tunnels*), traversing a network of switches and routers. The PCRF is responsible for policy control decision-making, as well as for controlling the flow-based charging functionalities in the Policy Control Enforcement Function (PCEF), which resides in the PGW. The PCEF provides the QoS authorisation (QoS class identifier, QoS Class Identifier (QCI), and bit rates) that dictates how a certain data flow is handled by the PCEF and ensures that this is done in accordance with the UE's subscription profile [167].

4.3.3. System Consumption and Elements Shares

Conventionally, IP packets traverse multiple core routers and are fully processed by the routers at each intermediate node. This significantly increases the energy consumed in transporting each packet from source to destination as the CN uses different ICT devices that consume approximately 2% - 10% of the global energy. A 50% increment in energy consumption is expected due to the increase in the number of mobile devices [168] in the mobile space. Therefore, drastic measures need to be taken in order to minimise the energy consumption in both the RAN and CN. From the energy perspective, data centres have already been identified as a critical segment when it comes to higher energy consumption [169]. This is due to the fact that ports (routers, switches) are deliberately kept active all the time for providing services when required. Normally, the CN equipment (switches, routers, links and optical transmission systems) are commonly redundant-provisioned to provide the best QoS and high availability of the network. Thus, great energy saving opportunities could be explored in the energy-inefficient core network during idle periods.

As the Internet traffic grows exponentially, new devices are introduced into the mobile space. Power consumption can be computed as a function of the capacity required to support a given access rate [170], taking into account estimates of efficiency improvement in routers. In order to fully evaluate the power consumption of the network equipment without using the rated power of the power suppliers, heat dissipation of the given network equipment can help to estimate the power consumption in the device. Considering the cooling requirements, we can assume that for every watt of power consumed in the CN another watt of power is required for cooling [171]. As most Internet traffic originates from the customer premises to a web server, which is often linked directly to the CN, it would be proper to devise new strategies that can minimise the number of hops in order to reduce the activity periods of the

CN equipment. This can be made possible by the Mobile Edge Computing (MEC [172]) and contents caching, which introduces the virtualisation of the functions and deploying them closer to mobile users.

4.3.4. Softwarization of the EPC Network Functions

Traditional EPC networks are complex and rather inflexible, use proprietary (costly) equipment and incur high signaling overhead. To overcome these limitations, *softwarization* of the NFs, mainly through Network Function Virtualisation (NFV), has been envisioned to minimisâĂće the dependence on proprietary equipment. The use of NFV technologies introduces a new network design paradigm named MEC [172]. MEC makes use of the large amount of power and storage space distributed at the network edge, which can yield sufficient capacities to perform computation-intensive and latency-critical tasks on mobile devices. It uses a virtualisation platform to run applications at the mobile network edge, which in turn turns a cell/BS into a *computation hub*. Mainly, it aims at enabling cloud computing capabilities and IT services in close proximity to end users, by pushing computation and storage resources towards the network edge (i.e., placing computing and storage resources in the access networks to improve delivery of contents/applications to end users). This enables processing of some workloads locally at the network edge, or in proximity to a set of co-located base stations, without moving them to the cloud. Since MEC servers are small-scale data centres, each of which consumes less energy than conventional cloud data centres, it is expected that powering the MEC infrastructure with renewable energy sources will reduce the overall network energy consumption. Despite of the potential possessed by MEC, energy efficiency is still a major concern in 5G systems and at the same time a prime concern for the design of MEC architectures [173]. This requires future mobile networks to be aware of sustainability issues, as customers' demands increase alongside rising energy costs and social concerns over carbon emission.

4.3.5. Power Consumption in virtualised Platforms

In view of the growing trend of data centre energy consumption and the associated environmental concerns, large IT companies have been increasingly pressured to minimise their carbon footprint [174], through the use of green energy and virtualised servers. However, the use of virtualised servers also comes with power consumption challenges. Therefore, it is important to understand why there is an increase in power consumption and overheads in the use of Virtual Machine (VM) for processing network and computing tasks. The amount of consumed power should be quantified in order to understand the power consumption variation in relation to the arrival workloads.

Considering the different workloads arrival rate at a virtualised MEC server $\lambda(t) \in [0, \lambda_{max}]$, where λ_{max} is the maximum possible arrival rate, the system decides the amount of workload that can be computed locally. The power consumption on the server consists of operational power, which is load independent and transmission and computation power, which is load dependent. To quantify the amount of power consumed by the server, we can consider the power consumed by the server resources, in relation to the workloads, and then define the system power as [175],

$$d_{op}(\lambda(t)) = d_{idle} + d_{dyn}(\lambda(t)) \tag{4.6}$$

where d_{idle} is the static power consumption and $d_{dyn}(\lambda(t))$ is the dynamic power consumption depending on the amount of workload. The computing power demand depends on the number of available active servers as well as the locally processed workload. [176] presents that on average an idle server consumes approximately 70% of the power consumed by the server running at the full CPU speed. This fact justifies the technique of switching idle servers to sleep mode to reduce the total power consumption. Therefore, the power model is defined as,

$$P(u) = k \cdot P_{max} + u(1 - k) \cdot P_{max}, \tag{4.7}$$

where P_{max} is the maximum power consumed when the server is fully utilised, k is the fraction of power consumed by the idle server and u is the CPU utilisation. The utilisation of the CPU varies over time due to the workload variability. Thus, the CPU utilisation is a function of time and it can be represented as $u(t)$. Therefore, the total energy consumption E for a node can be defined as an integral of the power consumption function over a period as shown below:

$$E = \int_{t_1}^{t_2} P(u(t))dt. \tag{4.8}$$

Since the energy impact of the VM can be considered in terms of dynamic energy used, the power consumption contributed by the CPU depends on several factors which include the specific instructions executed, on-chip cache usage, frequency used and the processor operation status (i.e, active or idle). An alternative to quantify the power usage is to track the processor state as such information is available in the operating system (OS) as processor utilisation. Then, for a given frequency the CPU energy model is defined as [177],

$$E_{cpu} = \alpha_{cpu} u_{cpu} + \gamma_{cpu}, \tag{4.9}$$

where $\alpha_{cpu}, \gamma_{cpu}$ are model specific constants and u_{cpu} is the processor utilisation fraction. When assigning CPU usage to active VMs, it requires accounting for the exact chip resources used including the shared caches and processing components. If the processor utilisation of VM A, is represented by $u_{cpu,A}$ then the energy consumed by VM A is denoted $E_{cpu,A}$ and it can be stated as,

$$E_{cpu,A} = \alpha_{cpu} u_{cpu,A}, \tag{4.10}$$

Considering the memory usage during active states, we can make use of the fact that prior power models have been able to identify the key factor affecting memory usage, that is, the read and write throughput. While instrumentation techniques have been applied to capture accurate memory throughput [178], a low overhead estimate of memory throughput can be identified through the Cache Miss (CM) counter, which is available in most processors and thus, memory power consumption can be stated as:

$$E_{Mem}(T) = \alpha_{mem} N_{CM}(T) + \gamma_{mem}, \tag{4.11}$$

where $E_{Mem}(T)$ represents the energy used by the memory over time T, $N_{CM}(T)$ is the number of cache misses over T and α_{mem} and γ_{mem} are linear model parameters. Then, the memory energy used by VM A can be defined as:

$$E_{Mem,A}(T) = \alpha_{mem} N_{CM,A}, \tag{4.12}$$

where $N_{CM,A}$ represents the number of cache miss for a VM A across all cores used by it during time period T and α_{mem} is a model specific constant.

The lack of visibility into power states of the hard disk hinders the development of power models related to disk usage. Therefore, the disk model is restricted to hypervisor observable parameters. The hypervisor can observe the number of read/write bytes as well as the service times for those reads/writes. Making use of the available information through read/write bytes, the energy consumed by the disk can be defined as follows:

$$E_{Disk}(T) = \alpha_{rb} b_r + \alpha_{wb} b_w + \gamma_{Disk}, \tag{4.13}$$

where $E_{Disk}(T)$ represents the energy consumed by the disk over time period T, b_r and b_w are the number of bytes read and written during T, γ_{Disk}, α_{rb} and α_{wb} are model parameters. It is also required to track the disk usage with respect to individual VMs. What can be noted is that the time at which the disk activity occurs is usually different compared to when the VM is active on the processor, since the hypervisor can batch Input-Ouput (IO) interrupts and buffer IO operations. Thus, instead of looking at storage system activity during the active context of a VM, the IO operations need to be explicitly tracked in the hypervisor. This yields the following disk energy model,

$$E_{Disk,A} = \alpha_{rb} b_{r,A} + \alpha_{wb} b_{w,A}, \tag{4.14}$$

where $b_{r,A}$ and $b_{w,A}$ represent the number of bytes read/written. Since the difference in read/write is negligible, a common parameter can be used to represent the number of bytes by taking the sum of the VM disk counters, and then re-representing equation 4.13 as:

$$E_{Disk}(T) = \alpha_{io} b_{io} + \gamma_{Disk}. \tag{4.15}$$

Then, VM disk energy can be computed as

$$E_{Disk,A} = \alpha_{io} b_{io,A}. \tag{4.16}$$

Other important components include the Network Interface Card (NIC) since it also contributes to the power consumption in the server system as data traffic is continually increasing and the data is transferred through the NIC subject to processing by the host OS network subsystem. This processing requires substantial amount of host CPU, especially for high speed links [179].

A crucial step in optimizing energy consumption is quantifying its use. However, due to the inability to efficiently measure energy on individual data centre assets, data centres have been unable to measure energy reduction and carbon emission reductions related to data centre consolidation, virtualisation, and capital equipment upgrade projects. With no way for data centres to measure and report the effectiveness of these projects, their success

can only be approximated through a power consumption framework for existing hardware platforms and hypervisors, i.e, tracking processor states.

4.3.6. Conclusion

Having powerful analytics can help to quantify, justify, and prioritise energy savings and carbon reduction savings, through virtualisation, server retirement, and equipment refresh/upgrade projects. Therefore, our contribution in SCAVENGE project will include developing new power models or improving the already existing power models in the context of micro data centres (MEC servers) in order to understand how much energy is required for computation with respect to the locally computed workloads in order to motivate the usage of renewable energy in future mobile networks. The proposed models must account for all the components that contribute to power usage in the server. This will also assist in developing energy-aware procedures for network management under battery levels constraints and workload variations. Currently, there are no energy-efficiency Key Performance Indicators (KPIs) for virtualisation platforms, therefore it is of great importance to develop/identify such KPIs in virtualised environments. Models validation and power usage in micro data centres will make use of available benchmark specs [180] following available simulation tool-kits.

4.4. Mobile Devices

4.4.1. Introduction

In this section, we introduce the constituting elements in a mobile phone. Our approach is to look at the mobile phone as a set of parts that consume energy depending on the tasks being performed. After that, models available for mobile devices power consumption are surveyed. Details on the models and the mathematical equations that build them are presented. Some models are limited in terms of technology by being useful only for 3G bands while others are UE specific. Different models focus on different input parameters, i.e., they model the mobile devices from different points of view depending on their consuming parts and performed tasks.

4.4.2. Constituting Elements

Mobile devices do not have a standard defining their constituents. Instead, 3GPP defines the set of rules related to radio and some operating capabilities, varying from release to release, and evolving these capabilities to match the evolution of the rest of the network. However, the most advanced and most widely used devices that obey to the latest 3GPP specifications, are usually equipped with state of the art cameras, touch screens, sensors, etc., that act as a complement to offer the users a wider and richer experience than just pure communications. These functionalities, complementary to the basic one of a mobile equipment in cellular networks can be present in a mobile device in many forms and numbers. With respect to connectivity, mobile devices are also usually equipped with more than one interface for different radio access technologies, mainly LTE and the previous cellular generations, and Wi-Fi and Bluetooth for shorter distance communications. However, some devices can carry other radio technologies like Infra-red or Near Field Communication (NFC), as examples.

Due to this variety, it is not possible to single out a unique model for mobile devices. We therefore try to group and categorise the most commonly seen constituting elements. A possible valid list would be Cellular connectivity, short range connectivity like Wi-Fi, NFC, BT, Zigbee or others, GPS, Baseband processor, Application processor, Human interfaces, Memory card interfaces, Sensing, Multimedia devices and Power and charging.

4.4.3. Model 1

An analysis of power consumption of a recent mobile phone (the Openmoko Neo Freerunner) is presented in [181] by measuring the power consumption of the main hardware component, to derive an overall energy model of this device as a function of the main usage scenarios. The results are validated using two additional mobile devices: HTC Dream (G1) and Google Nexus One (N1).

The experimental results are used to model the energy consumption of each part of the Freerunner device as a function of time (Table 4.3) where P_{BL} is the back-light power expressed in Watts and time t is expressed in seconds.

Table 4.3: Energy for various usage scenarios

Usage Scenario	Consumed Energy Model
Audio	$0.32t$
Video	$(0.45 + P_{BL})t$
SMS	$(0.3 + P_{BL})t$
Call	$1.05t$
Web	$(0.43 + P_{BL})t$
Email	$(0.61 + P_{BL})t$

4.4.4. Model 2

In [182], the transition state machine in 3G networks is described and a detailed energy consumption analysis of data transmission with constant bit rate is presented. Based on this description and analysis, a power consumption model is proposed and evaluated on the smart-phone Nokia N900, which follows a 3GPP release 5 and 6 supporting HSDPA/HSPA data bearers.

4.4.4.1. State machine

In 3G, there are five power consumption states:

- **Idle:** In this state, the UE is not communicating with the network, but still listening to broadcast messages. So, it does not have a Radio Resource Control (RRC) connection, but can still have an IP address and can be reached by paging.
- **CELL_PCH (Cell Paging Channel):** In this state, the channel is shared by all mobile devices (no dedicated physical channel is allocated to the UE, therefore no uplink activity is possible). So the inclusion of an additional mobile phone does not really have

Table 4.4: Power consumption of the different states in 3G [182]

Power Consumption State	Consumed Power
Idle	Small Consumption
CELL_PCH, URA_PCH	30 mW
CELL_FACH	400 mW
CELL_DCH	800 mW

any impact on the network. UE monitors paging messages from the Radio Network Controller (RNC), thus the power consumption is very small.

- **CELL_FACH (Cell Forward Access Channel):** In this state, UE is communicating with the network via a shared channel. Small bits of data can be transmitted at relatively low data rates (up to 16 kbps in the uplink).

- **CELL_DCH (Cell Dedicated Channel):** In this state, a dedicated transport channel is dedicated to UE in both uplink and downlink, giving the UE the potential to transfer large quantity of data. The power consumption of the radio interface is proportional to the number of transport block sets sent and received over this interface. It is consuming the most network resources and impact on the battery is very high too.

- **URA_PCH (UTRAN Registration Area_PCH):** This state is very similar to CELL_PCH, although some vendors have not implemented it in their solution.

Table 4.4 resumes the power consumption of the different states in 3G.

4.4.4.2. Power consumption modelling of CELL_DCH state

The power consumption of UE to send or receive packets in CELL_DCH state is given by this equation:

$$P = P_{DCH} + P_{peak} + P_{enc}(s), \tag{4.17}$$

where P_{DCH} is the power consumption of maintaining CELL_DCH state, P_{peak} is the power consumed of sending or receiving packets and $P_{enc}(s)$ is the power consumption of encapsulation or decapsulation of packets as a function of size s of the packet.

P_{DCH} includes the power consumption of reception of control signals. Therefore, it is the minimal power consumption for the UE, and it is considered approximately a fixed value since the most of the traffic is data traffic.

$P_{enc}(s)$ is assumed linear where the power consumption is proportional to the size of the packet. The experiments show that this quantity accounts only for 0.1% of the total power consumption, which is yielded only by computation and considered as negligible compared to the power consumption of sending and receiving. Therefore, this power consumption component is excluded from the model.

The number of transport blocks needed for sending one IP packet, which is decided by the size of the packet and specifications from different 3GPP releases, is given in the following:

$$N = \left\lceil \frac{s}{MTBS} \right\rceil, \tag{4.18}$$

where *MTBS* is the maximum transport block size.

The power consumption of peaks changes more or less linearly with the number of transport blocks. When more than one transport block is needed for sending or receiving one IP packet, the time spent on processing this packet is τN, where τ is defined as the value of the transmission time interval (TTI). Thus, by defining I as a packet sending intervals (in ms), and noticing that the packet sending interval is always larger than the packet processing time, P_{peak} can be given by:

$$P_{peak} = \frac{N}{I} E_{peak} \quad \text{when} \quad I > \tau N. \tag{4.19}$$

Finally, the power consumption for one connection in uplink or downlink in CELL_DCH state can be written as:

$$P = P_{DCH} + \frac{E_{peak}}{I} \left\lceil \frac{s}{MTBS} \right\rceil. \tag{4.20}$$

This model can be extended to formulate the power consumption of multiple connections by counting the amount of bits sent or received in a certain interval.

4.4.5. Model 3

In [183], an advanced model called "e-aware"is proposed for estimating how application layer protocol properties affect the energy consumption of mobile devices, operating in 3G Wideband Code Division Multiple Access (WCDMA) and Wireless Local Area Network (WLAN 802.11) networks. The model makes a distinction between signalling and media transfers, and takes into account the fundamentals of radio interface properties, such as different energy states and timers controlling them. The model is fine-tuned using device-specific coefficients that are defined according to real-world measurements with actual devices.

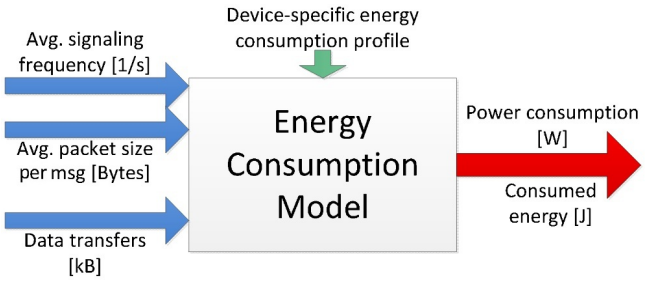

Figure 4.5: The operating principle of e-Aware model [183]

E-Aware model is shown in Figure 4.5, where the network parameters (blue arrows) include the average transmission interval and packet size for transferred data smaller than 1.5 KB

(often used as the Maximum Transmission Unit (MTU) with the User Datagram Protocol (UDP)), and the amount of moved data in the other case. The device-specific energy profile (green arrow) is based on real-life measurement data gathered by using a real mobile device in a real networking environment. As output, e-aware gives power and energy consumption estimates (red arrow) for the scenario.

The total power consumption at time t is defined as follows:

$$P(t) = \max[P_{sig}(t), P_{med}(t)], \tag{4.21}$$

where P_{sig} is the signalling power consumption, and P_{med} is the media transfers power consumption.

4.4.5.1. Signalling

In WCDMA, there are three threshold values for packet transmission interval: τ_1, τ_2 and τ_3 calculated using the following equations:

$$\tau_1 = D \cdot s_{sig} + t_{setup}, \tag{4.22}$$
$$\tau_2 = \tau_1 + t_{dch}, \tag{4.23}$$
$$\tau_3 = \tau_2 + t_{fach}, \tag{4.24}$$

where D is a coefficient, s_{sig} is the packet size (in bytes), t_{setup} is the delay caused by the transition from idle to transfer mode, t_{dch} and t_{fach} is the DCH and FACH release timer for WCDMA, respectively.

When the transmission interval τ is below τ_1, the radio remains in sending or receiving mode, and the power consumption is close to the continuous media transfers consumption, and is only slightly affected by the transmission interval. Thus, the power consumption when $\tau \leq \tau_1$ is given by:

$$P_{sig,tra}(\tau) = A \cdot s_{sig} - \tau B + C, \tag{4.25}$$

where A, B and C are coefficients.

When $\tau > \tau_3$, the idle power consumption is given by the following equation:

$$P_{sig,idle}(\tau) = \frac{\tau_3}{\tau}[P_{sig,fach}(\tau_3) - P_{idle}] + P_{idle}, \tag{4.26}$$

where P_{idle} is the power consumption of the device when the radio interface is in the Idle mode, and $P_{sig,fach}$ is the power consumed in the FACH state.

The power consumption of signalling depends on the size of the packets, because WCDMA triggers a change from FACH to DCH state when s_{sig} exceeds a certain threshold ($s_{threshold}$) controlled by the network operator. Following the measurements, a fixed $s_{threshold} = 250$ Bytes is used for uplink and downlink. Thus, when $s_{sig} < s_{threshold}$, FACH mode is used for transmission and τ_2 is skipped in the calculation ($t_{dch} = 0$). In this case, the power consumption is equal to $P_{sig,idle}$ when $\tau > \tau_3$. However, when $\tau_1 \leq \tau \leq \tau_3$, the power consumption is given by:

$$P_{sig,fach}(\tau) = \frac{\tau_1}{\tau}[P_{sig,tra}(\tau_1) - P_{fach}] + P_{fach}, \tag{4.27}$$

where P_{fach} is the power consumption of the device when WCDMA radio interface is in FACH mode but not sending or receiving data.

When $s_{sig} \geq s_{threshold}$, DCH is used for transmission. In this case, the power consumption is also equal to $P_{sig,idle}$ when $\tau > \tau_3$, to $P_{sig,dch}$ when $\tau_1 \leq \tau \leq \tau_2$ and to $P_{sig,fach}$ when $\tau_2 \leq \tau \leq \tau_3$ as shown in the following:

$$P_{sig,dch}(\tau) = \frac{\tau_1}{\tau}[P_{sig,tra}(\tau_1) - P_{dch}] + P_{dch}, \tag{4.28}$$

$$P_{sig,fach}(\tau) = \frac{\tau_2}{\tau}[P_{sig,dch}(\tau_2) - P_{fach}] + P_{fach}, \tag{4.29}$$

where P_{dch} is the power consumption of the device when the WCDMA radio interface is in DCH mode but not sending or receiving data.

On the other hand, IEEE 802.11 standard does not use standby timers, but instead switches the radio to idle mode right after media transfer. Therefore, τ_1 is calculated in the same way as in WCDMA, whereas τ_2 is given by the following equation:

$$\tau_2 = \tau_1 + t_{ovh}, \tag{4.30}$$

where t_{ovh} is an overhead time between the instant the 802.11 interface switches to Idle mode and the instant the power consumption returns to P_{idle}. During this time, the device consumes the power P_{ovh}.

As with WCDMA, when $\tau \leq \tau_1$, the 802.11 radio is almost 100% of its time in sending or receiving mode, thus it consumes the same amount of power $P_{sig,tra}$ as in WCDMA.
However, when $\tau_1 \leq \tau \leq \tau_2$, the power consumption is given by:

$$P_{sig,ovh}(\tau) = \frac{\tau_1}{\tau}[P_{sig,tra}(\tau_1) - P_{ovh}] + P_{ovh}, \tag{4.31}$$

and, when $\tau > \tau_2$, the power consumption is given by:

$$P_{sig,idle}(\tau) = \frac{\tau_2}{\tau}[P_{sig,ovh}(\tau_2) - P_{idle}] + P_{idle}. \tag{4.32}$$

4.4.5.2. Media Transfers

The file transfer time (t_{tra}) is calculated using the size of the moved data and the measured data transfer rate for the radio technology in use. The setup time (t_{setup}) is included in t_{tra}. During t_{tra}, the power consumption is averagely P_{UL} for upload and P_{DL} for downloads, after which the power consumption returns to P_{idle} through intermediate power state.

With WCDMA, transferring larger amounts of data is always made in DCH power state. Thus, after the completion of a transfer, the radio interface remains in DCH for t_{dch} seconds, and power consumption is P_{dch}. Then the power state is switched to FACH, in which the radio interface stays for t_{fach} seconds, while the power consumption is P_{fach}.

With 802.11, the power consumption is on average at intermediate level P_{ovh} for certain overhead time t_{ovh} after the transfer completion.

4.4.6. Model 4

Work presented in [184] provides a model for LTE UE power consumption. The proposed model is based on a review of the major power consuming parts in an LTE UE radio modem. The model is divided into four elements that are considered to be consuming parts and are functions of UL and DL power and data rate. The model also accounts for the two LTE RRC modes of operation, RRC idle and RRC connected. Figure 4.6 shows the model consuming parts.

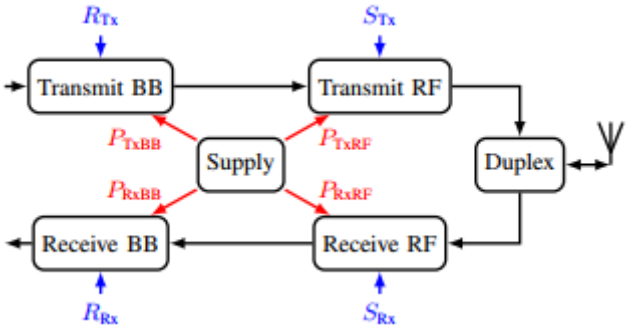

Figure 4.6: Model Consuming parts: Transmit Baseband, Transmit RF, Receive RF and Receive Baseband [184]

The model was validated by making measurements on a commercial LTE USB dongle. The measurements were used to assign realistic power consumption values to each model parameter. Verification measurements on the dongle show that the model results in an average error of 2.6 %.
The mathematical formulation of the model with its individual contributions is presented below.

$$\begin{aligned} P_{tot} \quad = \quad & m_{idle}.P_{idle} + \overline{m_{idle}}.(P_{con} + m_{Tx}.m_{Rx}.P_{Rx+Tx} + \\ & m_{Rx}[P_{Rx} + P_{RxRF}(S_{Rx}) + P_{RxBB}(R_{Rx}) + m_{2CW}.P(2CW)] \\ & m_{Tx}[P_{Tx} + P_{TxRF}(S_{Tx}) + P_{TxBB}(R_{Tx})])[W], \end{aligned} \tag{4.33}$$

where P is the power consumption. Subscript *tot* defines the total consumption, *idle* and *con* the consumption in RRC idle and connected mode, *RxRF* and *TxRF* the consumption of the RF part in the *Rx* and *Tx* chains respectively, *RxBB* and *TxBB* the consumption of the BB parts, and $2CW$ is related to increased consumption when using two codewords (CW) in DL. The parameters P_{Rx}, P_{Tx}, and P_{Rx+Tx} are included to model the base power the *Rx* and *Tx* chains consume when active. The logical variable m is the mode, which can be RRC idle, transmitting, receiving, and indicate the use of 2 CW. The *Rx* and *Tx* power levels are designated by S, and R is the *Rx* and *Tx* data rate.

The values of the parameters, after evaluating the model with real results taken from the experiment with a dongle are given in Tables 4.5 and 4.6.

Finally, after determining the best fit parameters to suit the model, tests were made to verify and compare the model results to the values obtained with the dongle equipment.

Table 4.5: Constant Parameters of the model [184]

Part	P_{idle}	P_{con}	P_{Rx}	P_{Tx}	P_{Rx+Tx}	P_{2CW}
Mode	m_{idle}	$\overline{m_{idle}}$	m_{Rx}	m_{Tx}	$m_{Tx}.m_{Rx}$	m_{2CW}
Value	0.50	1.53	0.42	0.55	0.16	0.07

Table 4.6: Polynomial Model Parameters in Miliwatt [184]

Part	Variable	p_0	p_{0-mod}	p_1	Residual e
Rx BB	R_{Rx}[Mbit/s]	1923	-26.6	2.89	0.08
Tx BB	R_{Tx}[Mbit/s]	2110	34.5	0.87	0.01
Rx RF	S_{Rx}[dBm]	1889	-60.7	-1.11	0.06
Tx RF1	S_{Tx}[dBm]	2004	-71.3	5.50	0.60
Tx RF2	S_{Tx}[dBm]	1132	-943	117	6.87

4.4.7. Model 5

In the work presented in [185], and in order to derive an accurate power consumption model, extensive measurements for different commercially available LTE UEs have been performed. The results show that the power consumption curve can be divided into two parts:

1. For a low transmission power, below a device specific threshold γ, there is a small, almost horizontal slope;
2. For higher transmission power values, the power amplifier switches the mode and the slope becomes significantly steeper;

From these observations, the empirically derived power consumption $\overline{P}$ can be approximated by two linear functions:

$$\overline{P}(P_{Tx}) = \begin{cases} \alpha_L.P_{Tx} + \beta_L, & P_{Tx} \leq \gamma \\ \alpha_H.P_{Tx} + \beta_H, & P_{Tx} > \gamma \end{cases}, \tag{4.34}$$

where the device-specific parameters (for the devices under tests) are given by Table 4.7. An approximation error for all devices is also provided in the table.

Table 4.7: Empirical Model Parameters for Different LTE UEs [185]

Model Parameter	HTC Velocity 4G		Samsung GT-B 3740	Samsung GT-B3730	Huawei E 398	Sierra Wireless AC 330U	
Frequency[MHz]	800	2600	800	2600	1800	2100	2600
α_L[mW/dBm]	4.8	4	7.7	7.2	10	5.6	5.4
β_L[W]	1.6	1.2	1.6	1.6	1.7	1.6	1.9
α_H[mW/dBm]	68	61	13	54	24	27	28
β_H[W]	0.79	0.52	0.4	1.5	1.9	1.5	1.8
γ[dBm]	12	12	11	10	16	16	16
$\overline{P}_{IDLE}$[mW]	40	40	175	44	236	63	63
MaximumError[%]	5.1	3.5	1.7	3.9	4.7	3.6	1.5

Table 4.8: Model description by radio access technology and energy phase type [186]

	3G	GSM	Wi-Fi
Transfer Energy - $R(x)$	$0.025(x) + 3.5$	$0.036(x) + 1.7$	$0.007(x) + 5.9$
Tail Energy - E	0.62J/s	0.25J/s	*NA*
Maintenance - M	0.02J/s	0.03J/s	0.05J/s
Tail-time - T	12.5s	6s	*NA*
50KB transfer with a 20 s interval	12.5J	5.0J	7.6J

4.4.8. Model 6

In [186] a consumption model for 3G, 2G and Wi-Fi in mobile devices is presented. The model derives from a detailed measurement study to quantify the energy consumed by data transfers across these radio interfaces. The study shows that

- In 3G, a large fraction (nearly 60%) of the energy, referred to as the tail energy, is wasted in high-power states after the completion of a typical transfer;
- In GSM, although a similar trend exists, the time spent in the high-power state after the transfer, or the tail time, is much smaller compared to 3G (6s VS 12 s);
- In WiFi, the association overhead is comparable to the tail energy of 3G, but the data transfer itself is significantly more efficient than 3G for all transfer sizes;

The model is dependent on the concept of ramp energy, i.e. the energy needed to change from a state of no connection to a state where there is a wireless transfer. It depends as well on what is called tail energy. It is explained explain that, after a transfer of any number of bytes is completed, there is a time window where the mobile device is still on a higher power consuming state, although the transfer is already completed.

The energy consumption model is a function of both the size of transfer and the time between successive transfers. Table 4.8 describes the energy model derived from the measurement study.

The energy spent to download/upload x bytes of data over the cellular network consists of ramp energy, transmission energy and tail energy. $R(x)$ denotes the sum of the Ramp energy and the transfer energy to send x bytes and E denotes the Tail energy. For Wi-Fi, $R(x)$ is used to denote the sum of the transfer energy and the energy for scanning and association, and the Tail energy E is set to zero. In addition to the transfer cost, the total energy to transmit a packet also depends on the time the interface is on. M denotes the energy consumption to keep the interface on, the maintenance energy per second. Finally, T denotes the tail-time. The last row in Table 4.8 shows an example computation for the average energy spent to download 50 kB of data with a 20 second inter-transfer interval.

4.4.9. Conclusion

We found that there is no generic model for the UE consumption: a model that would account for several radio interfaces, different UE components, that accounts fully for networking scenarios and that would be totally device brand and model independent. The studied models

provide some of these characteristics but not all and especially not all of them at the same time.

Moreover, we did not find any model that would take into account the security of cellular networks. But we think designing a model based on security for UEs is not crucial. Algorithms for key establishment and for integrity and encryption are well defined and depend only on the cellular technology in use. So, for different communication sessions in any cellular radio interface, power, data size and throughput are of bigger relevance, rather than the security system used.

4.5. Internet of Things Devices

Internet of things (IoT) is the concept based on the technologies of the interactions between ”things” and environment using benefits of the network technologies.

4.5.1. Constitution Elements

There are three components of the [187]: a) Hardware - made up of sensors, actuators and embedded communication hardware (b) Middleware - storage and computing tools for data analysis and (c) Presentation - visualisation and interpretation tools.

The hardware normally is presented by physical devices: sensor, node contains sensor interfaces (sensor unit), processing units, transceiver units and power supply [187], [188] (Figure 4.7). These devices can also contain additional application elements, such as locating system, power generator (power scavenging unit: solar cells etc.)

The sensor unit consists of two subunits: sensors and ADCs. The ADC converts the analog signal into the digital signal, which further is directed to the processing unit. This latter unit is associated with the small storage unit. It manages the procedures of collaboration of a sensor node with other nodes in the network. A transceiver unit connects the node to the network.

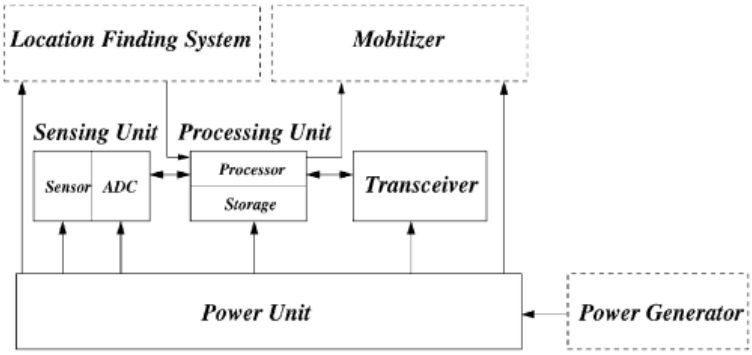

Figure 4.7: Sensor scheme [188]

4.5.1.1. Communication unit / Transceiver

The functionalities of both a transmitter and a receiver are combined into a single device known as a transceiver used in sensor nodes. A transceiver unit connects the node to the network. There are three options to provide communication abilities of the sensor node [189]: optical communication (laser), infrared, and RF. RF, laser and infrared communications require modulation, band pass, filtering, demodulation and multiplexing circuitry [188]. In general, radios can operate in four distinct modes of operation: transmit, receive, idle, and sleep.

Early hardware platforms/transceivers (CC1000, RFM, TR 1000) are operating in sub-GHz frequencies, characterised by low power consumption, but can be used only in the low-rate data collection scenarios. Higher data-rate is provided by ChipCon CC2400 and CC2500 operating in the 2.4 GHz ISM band, which were motivated by IEEE 802.15.4 compliance as well. To provide high data rates, Bluetooth or WiFi chips are used [190].

However, IoT concept dictates the requirements of decreasing of size, weight, energy consumption, and cost of the radio to be able to integrate radios in almost all objects. [191] indicates that the key components of IoT are Radio Frequency Identification (RFID) systems. These readers are composed of one or more readers and several RFID tags, which are applied to objects. Tags have a unique identifier. By generating the appropriate signal, readers trigger the tag transmission.

4.5.1.2. Processing unit

The processing unit is divided into two parts: Processing unit and storage unit.
Processing units (microcontrollers, microprocessors, SOCs, FPGAs) and software applications are also key component of IoT devices. Various platforms are used to run the IoT device applications: Arduino, UDOO, FriendlyARM, Intel Galileo, Raspberry PI, Gadgeteer, BeagleBone, Cubieboard, Z1, WiSense, Mulle, and T-Mote Sky, as well as software platforms which are presented by operating systems [192].

Generally, 8-bit microprocessors are attached to a sensor. 16-bit and 32-bit microprocessors are components of sink nodes, gateway nodes, and Internet access nodes. The most common chips used for Wireless Sensor Network (WSN) IoT applications are ARM9, XScale, and ColdFire [193].

The storage unit of the node consists of a flash memory, containing the program code for the node. This Random Access Memory (RAM) stores sensed information and any data needed for computations. Some motes also have non-volatile storage. But writing to the SD card has a high cost power, that is why this solution is more expensive and is only for large capacity energy storage devices [194].

There are several Real-Time Operating Systems (RTOS) that are used to run IoT applications. One of the most widely used ones is the Contiki RTOS, which also has a simulator (Cooja) to simulate IoT and WSN applications [192]. TinyOS, LiteOS, Riot OS, SOS, MANTIS OS, EYES OS, Jennic BS, and OKI RTOS are also lightweight operating systems developed for IoT applications [192].

Another computational component of an IoT device is a cloud platform. It aims at sending data to the cloud and Big data centres to be processed in real-time [192].

4.5.1.3. Power supply

Power supply of IoT devices can be provided by primary, secondary batteries, capacitors, fuel cells or simply powered by a grid. More interesting is that different components of a sensor can have different sources of power. For example, in [195], the power supplies for two sensing units are from electrical outlets, whereas a third sensor is powered from a battery.

Energy can be harvested from environmental sources: thermal, solar, vibration, and wireless RF energy sources. Therefore, the harvesting unit is dependent on the type of the energy source. For example, two main units for RF energy harvesting are the wireless energy harvesting unit (WEH) and the power management unit (PMU) [196]. PMU is needed to control the transceiver and sensing unit functionality, and manages the energy consumption of each unit and/or accommodates battery charging using the harvested energy.

4.5.1.4. Power amplifier

A low power amplifier (PA) is a key component of WSNs. To reduce operational cost, all the energy used by the transceiver is either scavenged from the environment or from a battery source and it should last the entire lifetime of the product. IoT devices are supposed to operate for several years, that is why few principles were established for power amplifiers, which serve to optimise the power consumption. The principales as outlined in [197] are: the power added efficiency of the power amplifier when switched on should be maximised; the power control mechanism should be incorporated to vary the output power for various transmit distance; the power amplifier should be shut down when idle; the turn-on time of the power amplifier should be short to minimise overhead power; the transmit power should be about 1-3 mW for typical receiver sensitivity and indoor multi-path fading conditions.

4.5.1.5. Sensing unit

In reality, the sensor unit is supposed to be a transceiver between the physical world and the world of processing unit [198]. The sensor unit is the one of the vital part of wireless sensor node, it senses the physical state of the environment and sends the data to the processor.

Sensing units of IoT devices consist of sensors and ADCs. IoT devices/sensors can be equipped by many types of sensor units such as seismic, low sampling rate magnetic, thermal, visual, infrared, acoustic, radar, gyroscopes, pressure, humidity, image, light, gas RFID and micro flow. They are able to monitor a wide variety of following ambient conditions [188], [199]: temperature, humidity, vehicular movement, lightning condition, pressure, soil make-up, noise levels, the presence or absence of certain kinds of objects, mechanical stress levels on attached objects, and the current characteristics such as speed, direction, and size of an object.

4.5.2. System Consumption and Elements Shares

4.5.2.1. System consumption

Industrial wireless sensor devices follow a common behavioural pattern, so their power consumption can be easily characterised and is due mainly to cyclic activities as following:

- acquiring data by sensors
- data processing in a controller unit
- sending/receiving information in the network
- internal processes of the operating system

Figure 4.8 shows the periodicity of the IoT device behaviour in terms of power consumption level over time: the device wakes up within T_{RCD} intervals, capturing a sequence of N_S samples at T_S sampling periods, and taking a time T_{PRC} to process the record. The average interval time between radio packets is depicted as T_{MSG}, time in which the device can also go to sleep after finishing transmitting the data or if there is no data to send.

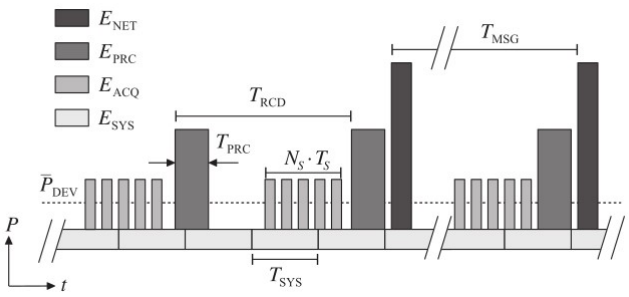

Figure 4.8: Characteristic time evolution of energy usage split in components. Dashed line represents the average consumption [200]

Regarding the energy consumption of acquiring data by sensors, according to [201], to better understand what is the energy required in collecting one sample, we have to look at a breakdown of the microprocessor/ sensor activity during that sample: the sensor start-up time, the processor and sensor energy required to initiate sampling, the analog-to-digital conversion and the transfer of data from the ADC output to the processor memory. This means that the data acquisition power consumption is subject to the chosen microprocessor and the sensor. Also, the time between consecutive records is scheduled from the application layer, thus providing a control mechanism over the energy consumption at the expense of increasing the monitoring interval time.

The energy consumption for data processing in a controller unit depends basically on the technology of the used processor [200]. The number of operations to process the original sensed signal must be recorded, accounting basically for the number of arithmetic operations, namely, additions, multiplications, divisions, and comparisons, i.e., the main actors in signal processing loops [201]. Thus, depending on selected hardware architecture, these

counters have to be mapped into the corresponding number of microcontroller clock cycles, and subsequently, the latter is mapped into the corresponding energy expenditure. The importance of the processor architecture is analysed in [52], where the authors implement an algorithm and evaluate it on different operating systems (TinyOS v1.0 (T1), TinyOS v2.0 (T2), Contiki and Mantis). When measuring the power consumption in a real platform, a term related with the operating system management tasks is always present. This term is a constant bias for all measurements and can be accounted only once in the general model for power consumption. To illustrate this, [52] performed measurements in order to analyse and compare the low-level current consumption of two motes (MicaZ and Tmote Sky), during the execution of an application running on different operating systems. The amount of energy consumption that the operating system introduces can be minimised if power management functions of the operating systems are used.

The energy consumption during the network protocol execution is given by the sum of the following terms: node energy consumption during the sleep time slots, node energy consumption during receive time slots and node energy consumption during transmission time slots. The processor influence on energy consumption when implementing the same communication protocol, IEEE 802.15.4, is analysed in [202] by evaluating various radio modules and showing that there is a big difference in energy consumption for radio chips produced by different providers even when implementing the same communication protocol. The network protocol is the one that sets the data rate and the message length, the number of messages to retransmit and how often to send messages. Data rate and payload size affect directly the power consumption of the devices [202]. However, of all components, the RF components consume the major share of the total power consumption, even more than the CPU. The RF components include PA, ADC, DAC, Low Noise Amplifier (LNA), Local Oscillator (LO), intermediate frequency amplifier (IF), filters and mixers. The management of energy consumption of the RF transceiver depends on the design of these constituents, and the design of the modulation and coding schemes is interdependent on the specifications of these components. [203] presents a comprehensive analysis of the energy consumption of wireless cellular systems. It studies the impact of different classes of PA on the energy efficiency and also studies the impact of Peak-to-Average-Power-Ratio (PAPR) on the efficiency of the PA. Rough estimates of the energy consumption by different elements in different states are given in [204] and reproduced in Table 4.9.

4.5.3. Energy Consumption Models

In this section, we consider three different models for energy consumption of IoT devices, which use different approaches to describe the energy consumption. The models include sensing, communication and processing modelling with focus on the circuit consumption as well as on impact of communication and sensing protocols on the overall consumption.

4.5.3.1. Model 1

The model consists of three elements: transceiver, sensing and processor energy consumption.

Table 4.9: Power consumption of RF elements

Block	Transmission(mW)	Reception(mW)	Idle(mW)	Deep sleep(mW)
PA	60.0	0	0	0
DAC	15.4	0	0	0
RF Mixers	25.2	25.2	0	0
BB Mixers	25.2	25.2	0	0
Ref. System	0.5	0.5	0.5	0.1
Frequency Synthesiser	40.0	40.0	0	0
Filters	6	6	0	0
ADC	0	5.85	0	0
LNA	0	24	0	0
Total	172.3	126.75	0.5	0.1

4.5.3.1.1 Transceiver energy consumption model

According to [205], the transceiver energy model represents the sum of state energy consumption ($E_{trans-state}$) and state transition energy consumption ($E_{trans-change}$), where usually six states (Tx, Rx, Off, Idle, Sleep, CCA/ED) and nine state transitions are defined.

$$E_{trans-state} = \sum \frac{V_{tr} I_{TX} L_i}{R} + \sum \frac{V_{tr} I_{RX} L_i}{R} + V_{tr}(I_{Idle} T_{Idle} + I_{sleep} T_{sleep} + I_{CCA} T_{CCA}), \tag{4.35}$$

where I_x is the electric current in the state x, T_x is the time interval of transceiver in the state x, V_{tr} is the working voltage, L_i is the size length of the ith packet of receiving or sending.

The transition energy consumption is defined as:

$$E_{trans-transition} = \sum_{j=1}^{n} N_{trans-change}(j) e_{trans-change}(j), \tag{4.36}$$

where n is the number of state transitions, $N_{trans-change}(j)$ is the frequency of the state in transition j, and $e_{trans-change}(j)$ is the energy consumption of one-time state transition j defined as:

$$e_{trans-change}(j) = V_{tr} T_{init-end}(j) \frac{I_{init}(j) + I_{end}(j)}{2}. \tag{4.37}$$

4.5.3.1.2 Sensing energy model

The sensor module can be represented as a sum of one-time energy consumption of sensor closing E_{on-off} and opening E_{off-on} and energy consumption of sensing operation:

$$E_{sensor} = E_{on-off} + E_{off-on} + E_{sensor-run} = N(e_{on-off} + e_{off-on} + V_s I_s T_s), \tag{4.38}$$

where V_s,I_s are the working voltage and current of the sensor, T_s is the time interval of the sensing operation, N is the number of opening and closing operations.

Simulations show that the energy consumption in the sensing model is inversely proportional to the sensing period.

4.5.3.1.3 Processing energy model

The processor is responsible for the sensor controlling, data processing and protocol communication. It supports three states: sleep, idle and run. The processor energy function is described by:

$$E_{cpu} = \sum P_{cpu-state}(i)\, T_{cpu-state}(i) + \sum N_{cpu-change}(j)\, e_{cpu-change}(j), \tag{4.39}$$

where $i = 1, .., m$ is the processor operation state (mostly common $m = 3$), $j = 1, .., n$ is the type of the state transition ($n = 5$), $P_{cpu-state}(i)$ is the power of the state i, $T_{cpu-state}(i)$ is the statistical variable that represents time interval in the state i, $N_{cpu-change}(j)$ is the frequency of state transition j, $e_{cpu-change}(j)$ is the energy consumption of one-time state transition j.

4.5.3.2. Model 2

In [206], a power consumption model for low power IoT devices is presented, which takes a new system level approach.
Energy follows the *energy flow model* given by:

$$\mathcal{E}_{BUF} + \int_{\tau=0}^{t} \mathcal{P}_{SCV}(\tau) d\tau \geq \int_{\tau=0}^{t} \mathcal{P}_{DEV}(\tau) d\tau = \mathcal{E}_{DEV}(t), \tag{4.40}$$

with $\mathcal{E}$ and $\mathcal{P}$ being the energy and power terms, respectively.
In this general model, the energy initially stored in the buffer $\mathcal{E}_{BUF}$ and the additional energy scavenged from the surroundings $\mathcal{E}_{SCV}$ must be greater than the energy required for the device to operate $\mathcal{E}_{DEV}$ throughout the whole operation time t of the system. Energy flow in a wireless sensor device closely follows this model.

4.5.3.2.1 Bottom-Up Modelling of Energy Consumption

The role of the duty-cycle is fundamental in power consumption. Therefore, the power required to operate a wireless sensor device can be broken down into three main blocks: for data sensing $\mathcal{P}_{ACQ}$ (or acquisition), data handling $\mathcal{P}_{PRC}$ (or processing), data communication $\mathcal{P}_{NET}$ (or networking) and system management tasks $\mathcal{P}_{SYS}$. The general expression $\mathcal{P}_{DEV}$ is given by

$$\mathcal{P}_{DEV} = \mathcal{P}_{NET} + \mathcal{P}_{ACQ} + \mathcal{P}_{PRC} + \mathcal{P}_{SYS}. \tag{4.41}$$

4.5.3.2.2 Data Communication energy model

Point-to-Point Communications The simplest model for wireless communications consists of an interference-free, single-hop scenario. Energetic inefficiencies due to collisions and idle times for floor acquisition are also ignored. In this case, the power consumption can be estimated for each device independently.

The average power of the communication block can be expressed in terms of the energy required to send a radio message $\mathcal{E}_{MSG}$, and the time between consecutive messages T^i_{MSG}.

$$\bar{\mathcal{P}}_{NET} = \sum_{i=1}^{N_{MSG}} \frac{\mathcal{E}_{MSG}}{T^i_{MSG}} \tag{4.42}$$

Time Synchronised Networks The employed model is based on profiling the energy consumption $\mathcal{E}^i_{SLOT}$ in each of the time slots, counting the number of slots of each type, and calculating the total energy $\mathcal{E}_{SF}$ of the slot-frame.

$$\bar{\mathcal{P}}_{NET} = \frac{\mathcal{E}_{SF}}{T_{SF}} = \frac{1}{T_{SF}} \sum_{i=1}^{N_{SLOTS}} \mathcal{E}^i_{SLOT} \tag{4.43}$$

The key feature of the presented methodology is the impact that the network configuration has on the application's energy consumption. In a TSCH network, the slot-frame period is determined by the number of slots in the slot-frame and the time assigned to each slot. As T_{SLOT} is a fixed network parameter, the slot-frame length N_{SLOT} determines how often actions repeat, which usually depends on the application's requirements.

4.5.3.2.3 Data Acquisition Energy Model

The energy consumption of the acquisition component can be modelled in the following way:

$$\mathcal{E}_{ACQ} = \mathcal{E}_{SMP}.N_S \quad (Regular\ sensing), \tag{4.44}$$

$$\mathcal{E}_{ACQ} = \mathcal{E}_{SMP}.N'_S.Pr(e) \quad (Event-driven\ sensing). \tag{4.45}$$

In this expression, $\mathcal{E}_{SMP}$ is the energy needed to acquire one sample, and N_S is the number of samples taken during one regular sensing interval. For event-driven applications, $Pr(e)$ is the probability of an event occurring in one sensing interval, and N'_S is the number of samples taken following the occurrence of an event.

4.5.3.2.4 Data Processing Energy Model

The energy consumed by the processing ($\bar{\mathcal{P}}_{PRC}$ and $\bar{\mathcal{P}}_{SYS}$) are modelled based on the number of operations required for each computation.

4.5.3.3. Model 3

The model in [207] focuses on the impact of the communication hardware on the total power consumption for single hop and multi-hop networks. The components of power consumption are functions of distance, radio environment (i.e. ϵ and α-the path loss exponent: $\alpha = 2$ for free-space) and of the drain efficiency of the power amplifier (i.e. η). The analysis here is very conservative because not all of the overhead of reliable communication is included, such as the overhead for time synchronisation, network topology design, route discovery, or microprocessor (operating system and power management algorithms). Also, the power consumption for data acquisition is not modelled. A plus of this model is the consideration of the impact of power amplifier and communication channel on the power consumption of a wireless sensor network. The minimum power consumption to reliably transmit data to another sensor node which is located at a distance d is given as:

$$P_T(d) = P_{T0} + \frac{\epsilon d}{\eta}, \tag{4.46}$$

where P_{T0} is the power consumption in front-end circuit for transmitting or receiving and does not depend on the transmission range, $\epsilon = P_{Rx-min}A$, A is a parameter determined by characteristics of the transmitting and receiving antennas and P_{Rx-min} is the minimum required received power for reliable communication.

4.5.4. Conclusion

The considered models include three consumption models: communication, sensing and processing. The energy model in [205] is reasonable to apply when the model of the microprocessor is known, then the information about work voltage and current is available. Similarly, the information about state power and transition time is available for known type of chip. For the sensing model, the main characteristic of the energy consumption is given as the sensing period. The model is complete and fully applicable for usage.

The model in [208] can be applied to analyse the energy consumption from a system level perspective, taking into account the network protocol, duty cycle and energy per message. The measurements required can be acquired from input and output points of the various components of the IoT sensors.

The model in [207] does not model the consumption of data acquisition, sensing or operating system, but takes into consideration the impact of the efficiency of the power amplifier (η) and of the communication channel (ϵ, α) on the power consumption for a reliable communication.

4.6. Conclusion

In this chapter, we present models for the different devices we identified in the network.

Section 4.2 presents a typical base-station architecture, studies power consumption modelling using two approaches. The first approach is a load based study with a macro/small

base station comparison, while the second studies the influence of different backhaul architectures on the power consumption models.

In Section 4.3, the core network is described but we focus the power consumption survey on the mobile edge computing servers, which is of main interest for future contributions in SCAVENGE project.

Section 4.4 describes a generic mobile device and concludes that the variety of devices makes the modelling of mobile phones very difficult and gives some models tackling specific devices, device features or hardware.

Finally, Section 4.5 addresses energy consumption models of IoT devices. IoT networks include a wide variety of devices with various functionalities, hardware, software, wireless transceivers, etc, and thus have many different models. In this section, we extract from the literature several models based either on a hardware component scale or a more system scale considering the different communication protocols.

5. Conclusions

In this intermediate report, we have presented an overview of the literature in the context of SCAVENGE WP2 on Energy models. The WP2 objective is to provide common ground across the SCAVENGE project regarding the modelling of energy within energy harvesting communication systems and networks. The work package is divided in two tasks:

- **Task 2.1: Energy harvester and storage models**, which aims to characterise the different types of energy harvesting and storage devices that are or could be used in communication networks.
- **Task 2.2: Energy consumption models**, which strives to quantify and model the power consumption within the different elements of wireless communication networks.

In Chapter 2, several harvestable energy sources have been identified: solar, heat, vibration, wind and electromagnetic radiations.
Solar energy (Section 2.2) can be harvested using different types of photovoltaic panels or used after concentration as a heat source to power a turbine and then produce electricity. Solar radiation is one of the most commonly used energy source in many applications. Models provided in the state-of-the-art are complete, going from the simplest to the most complex using artificial intelligence. In SCAVENGE, Solarstats [31] is the main model used by ESRs.
Heat (Section 2.3) is converted to electricity using thermoelectric harvesters. Thermoelectric energy is environmentally-friendly and serves in a few applications. To widen the applicability of thermoelectric harvesters, the efficiency of the energy conversion has to be improved. For this purpose, studies have to be directed to increase the performance of thermoelectric materials.
Vibration energy (Section 2.4) harvesters can be represented by several models. These models are complete and ready to use. Therefore, we conclude that the state-of-the-art literature already provides good mathematical tools to evaluate problems in the presence of these harvesters.
Wind (Section 2.5) is typically harvested using vertical and horizontal turbines. As a well established renewable energy source, wind power is an interesting option as it can take advantage of existing structures such as high antenna masts. However, the system needs to be designed such that the turbines do not interfere with wireless communication. Models are well established both on the resource and the harvester side.
Electromagnetic radiation (Section 2.6) from the surrounding environment can power mobile or IoT devices. However, the current technology only offers very low-efficiency energy transfers.
For each energy source, we have described the resource, the-state-of-the-art of harvesters and finally the models, that will allow us to include harvesting systems within our energy management techniques and optimisations.

Throughout our literature review, we encountered three main categories of energy storage devices gathered in Chapter 3: mechanical, electrical and electro-chemical.
Mechanical storage (Section 3.2) includes compressed air and flywheel storage solutions. These technologies due to their size are mostly suited for large infrastructures such as base

stations and the core network.
Electrical storage (Section 3.3) typically uses capacitors. Their limited capacity often restricts them to applications in IoT. The models proposed for super-capacitors are based on equivalent electrical circuits and have proven to be accurate in describing real behaviours in experimental validations.
Electrochemical storage (Section 3.4) is the main technique used nowadays. It offers many different types, characteristics and corresponding models. We also present emerging technologies such as fuel cells and flow-batteries. However, these technologies are at the stage of prototypes and face multiple challenges, such as low-efficiency, expensive manufacturing, etc.

In Chapter 4, to model the power consumption in communication networks, we divided the network into four main families of devices: the base stations, the core network, the mobile devices, the IoT devices, or sensor nodes. Each device is decomposed into several subsystems in order to better understand the overall device. Models from the literature featuring different scenarios relevant to ESRs individual projects are presented.
The **base stations** (Section 4.2) are modelled in multiple ways in the literature. We narrow our approach on traffic-based and backhaul architecture-based models to cover our needs. For simplicity, models for base stations are often considered linear with respect to the load.
The **core network** (Section 4.3) represents a large infrastructure, but in this report, we restrict its modelling to our needs and mainly focus on modelling the mobile edge computing server.
Mobile devices (Section 4.4) can be modelled in many ways. Although the surveyed models for mobile devices lack some characteristics that would make them more complete, we find that there is no added value in improving those models because we can simply select an appropriate model among them for any studied use case.
For **IoT devices** (Section 4.5), there are many available models, which are application-dependent. They present various levels of complexity and take into account multiple parameters. We can reuse them in the project to provide new models considering and combining various parameters depending on the studied applications. However, when using any of these models to quantify the consumed energy by IoT components and protocols, only the total consumption of the constituting elements is quantified. Therefore, these models are not suitable for networking scenarios where nodes frequently cooperate, often causing short-term increase in power consumption. The available models cannot predict or quantify this increase.

Some of the reviewed models in this report have already been used in the work of several ESRs through paper publications to measure the effectiveness of new energy management algorithms and transmission techniques:

- Towards self-control of service rate for battery management in energy harvesting devices, Gindullina et al. [209]
- Optimal direct load control of renewable powered small cells: A shortest path approach, Piovesan et al. [210]
- A Markov Model Accounting for Charge Recovery in Energy Harvesting Devices, Badia et al. [211]

- Energy minimization based Resource Scheduling for Strict Delay Constrained Wireless Communications, Fawaz et al. [212]

On the other hand, this literature review is a starting point for further investigations. Certain models can be refined according to research outputs of each ESR, or can be integrated in more comprehensive network-scale models.

For solar energy harvesting, the next step will be to define a model that can comprise different characteristics. This analysis should start from the data and measurements that are available from different locations. Artificial neural networks represent good mathematical tools for this problem. We will also approach the problem using stochastic Markov models, which can accurately predict the energy production and are furthermore analytically simple.

As for energy storage models, especially energy buffers related to electrochemical storage, we leverage the use of generalized models that include the energy level in the battery in the previous time slot, the energy that is used locally, and the energy from the harvester. This work will address the lack of existing models that are closely related to our network scenario, where each base station is equipped with an energy buffer that may allow it to be a source or consumer of energy and the virtualised computing platform is also renewable-powered. Other key characteristics to consider for the battery management are leakage and battery degradation. These characteristics are individual for each type of energy storage. Defining a model that will aggregate all the characteristics can benefit the development of a battery management system.

Base station power consumption modelling has been widely studied. Nevertheless, it is still an evolving topic since new features appear and hence, new and more complex models are needed. Our contribution mainly focuses on heterogeneous cellular networks with cache-enabled and densely employed small-cell base stations. Existing power consumption models for backhaul links are not directly applicable to such networks that we study. For instance, backhaul links' load thus power consumption can be further reduced in cache-enabled heterogeneous cellular networks via coded-delivery and coded caching techniques. In the scope of WP2, we aim to provide a novel power consumption model taking into account the coded-delivery and coded-caching techniques. Further analysis can be done starting from practical measurements on the existing equipment.

For the core network, we will propose new power models for virtualised computing platforms or improve existing ones in the context of micro data centres (MEC servers). These models should help us to characterise how much energy is required for hardware running virtualisation tools (VM or Container), with respect to the locally computed workloads. The proposed models models will motivate the usage of renewable energies in future mobile networks. They must account for all the components that contribute to power usage in the server.

Finally, concerning IoT devices consumption modelling, although we consider the presented models complete and ready to use, we classify them as not suitable to support stochastic and opportunistic interactions in networking scenarios. Therefore, new models are needed to account for such frequent interactions between IoT devices, especially regarding security protocols. We will also propose more accurate models, with focus on end-user devices

considering particularly cache-enabled devices. We will investigate coded caching which is expected to help in multicast communication and reduce the number of packets required to be transmitted on the network to satisfy a group of users.

This future work will be reported in next deliverable D2.2 of WP2. The new energy models proposals will contribute to a smarter design of energy harvesting communication systems and networks. They will allow us to assess the full impact of including energy harvesting and new energy management techniques in wireless communication networks proposed by SCAVENGE.

References

[1] ITU, "ICT Facts and Figures." https://www.itu.int/en/ITU-D/Statistics/Documents/facts/ICTFactsFigures2013-e.pdf, 2013.

[2] IEA, *CO2 Emissions from Fuel Combustion 2016*. International Energy Agency, 2016.

[3] "SOLARGIS Maps." http://solargis.com/products/maps-and-gis-data/free/download/world.

[4] R. Amatya, F. Brushett, A. Campanella, G. Kavlak, J. Macko, A. Maurano, J. McNerney, T. Osedach, P. Rodilla, A. Rose, A. Sakti, E. Steinfeld, J. Trancik, H. Tuller, C. Atlamazoglou, K. Berkemeyer, R. Brandt, A. Gupta, A. McCree, R. O' Shea, P. Primard, J. Resvick, and J. Whittaker, *The Future of Solar Energy*. Massachusetts Institute of Technology, 2015.

[5] S. Kim, R. Vyas, J. Bito, K. Niotaki, A. Collado, A. Georgiadis, and M. M. Tentzeris, "Ambient RF Energy-Harvesting Technologies for Self-Sustainable Standalone Wireless Sensor Platforms," *Proceedings of the IEEE*, vol. 102, pp. 1649–1666, Nov. 2014.

[6] "PN junction – solar Cell Central." http://solarcellcentral.com/junction_page.html.

[7] "How Solar Works." http://www.solarconnexion.com/how-solar-works/.

[8] R. V. Prasad, S. Devasenapathy, V. S. Rao, and J. Vazifehdan, "Reincarnation in the Ambiance: Devices and Networks with Energy Harvesting," *IEEE Communications Surveys & Tutorials*, vol. 16, no. 1, pp. 195–213, 2014.

[9] H. Müller-Steinhagen and F. Trieb, "Concentrating solar power," *A review of the technology. Ingenia Inform QR Acad Eng*, vol. 18, pp. 43–50, 2004.

[10] M. Falchetta, "Concentrating solar power," tech. rep., Energy Research Knowledge Centre (ERKC), 2013.

[11] W. Zeng, Y. Cao, Y. Bai, Y. Wang, Y. Shi, M. Zhang, F. Wang, C. Pan, and P. Wang, "Efficient Dye-Sensitized Solar Cells with an Organic Photosensitizer Featuring Orderly Conjugated Ethylenedioxythiophene and Dithienosilole Blocks," *Chemistry of Materials*, vol. 22, pp. 1915–1925, Mar. 2010.

[12] M. Grätzel, "Mesoscopic Solar Cells for Electricity and Hydrogen Production from Sunlight," *Chemistry Letters*, vol. 34, pp. 8–13, Jan. 2005.

[13] B. Lee, D. B. Buchholz, and R. P. H. Chang, "An all carbon counter electrode for dye sensitized solar cells," *Energy & Environmental Science*, vol. 5, no. 5, p. 6941, 2012.

[14] Q. Qin, J. Tao, and Y. Yang, "Preparation and characterization of polyaniline film on stainless steel by electrochemical polymerization as a counter electrode of DSSC," *Synthetic Metals*, vol. 160, pp. 1167–1172, June 2010.

[15] R. M. Ambrosi and et al., "Development and Testing of Americum-241 Radioisotope Thermoelectric Generator: Concept Design and Breadboard System," *Nuclear and Emerging Technologies for Space*, 2012.

[16] T. Khatib, A. Mohamed, and K. Sopian, "A review of solar energy modeling techniques," *Renewable and Sustainable Energy Reviews*, pp. 2864–2869, June 2012.

[17] Z. Sen and E. Tan, "Simple models of solar radiation data for northwestern part of Turkey," *Energy Conversion and Management*, pp. 587–598, Mar. 2001.

[18] J. K. Yohanna, I. N. Itodo, and V. I. Umogbai, "A model for determining the global solar radiation for Makurdi, Nigeria," *Renewable Energy*, July 2011.

[19] A. A. El Sebaii, F. S. Al Hazmi, A. A. Al Ghamdi, and S. J. Yaghmour, "Global, direct and diffuse solar radiation on horizontal and tilted surfaces in Jeddah, Saudi Arabia," *Applied Energy*, pp. 568–576, Feb. 2010.

[20] M. Mohandes, S. Rehman, and T. O. Halawani, "Estimation of global solar radiation using artificial neural networks," *Renewable Energy*, pp. 179–184, Aug. 1998.

[21] S. M. Al Alawi and H. A. Al Hinai, "An ANN-based approach for predicting global radiation in locations with no direct measurement instrumentation," *Renewable Energy*, pp. 199–204, Aug. 1998.

[22] G. Mihalakakou, M. Santamouris, and D. N. Asimakopoulos, "The total solar radiation time series simulation in Athens, using neural networks," *Theoretical and Applied Climatology*, pp. 185–197, 2000.

[23] A. Sozen, E. Arcaklioglu, M. Ozalp, and E. G. Kanit, "Use of artificial neural networks for mapping of solar potential in Turkey," *Applied Energy*, pp. 273–286, Mar. 2004.

[24] A. Sozen, E. Arcaklioglu, and M. Ozalp, "Estimation of solar potential in Turkey by artificial neural networks using meteorological and geographical data," *Energy Conversion and Management*, pp. 3033–3052, Nov. 2004.

[25] D. A. Fadare, "Modelling of solar energy potential in Nigeria using an artificial neural network model," *Applied Energy*, pp. 1410–1422, Sept. 2009.

[26] K. S. Reddy and M. Ranjan, "Solar resource estimation using artificial neural networks and comparison with other correlation models," *Energy Conversion and Management*, pp. 2519–2530, Sept. 2003.

[27] M. Benghanem and A. Mellit, "Radial Basis Function Network-based prediction of global solar radiation data: Application for sizing of a stand-alone photovoltaic system at Al-Madinah, Saudi Arabia," *Energy*, pp. 3751–3762, July 2010.

[28] S. Rehman and M. Mohandes, "Artificial neural network estimation of global solar radiation using air temperature and relative humidity," *Energy Policy*, pp. 571–576, Feb. 2008.

[29] T. Khatib, A. Mohamed, K. Sopian, and M. Mahmoud, "Modeling of Solar Energy for Malaysia Using Artificial Neural Networks," pp. 82–87.

[30] A. Mellit, M. Benghanem, A. H. Arab, and A. Guessoum, "A simplified model for generating sequences of global solar radiation data for isolated sites: Using artificial neural network and a library of Markov transition matrices approach," *Solar Energy*, pp. 469–482, Nov. 2005.

[31] M. Miozzo, D. Zordan, P. Dini, and M. Rossi, "SolarStat: Modeling photovoltaic sources through stochastic Markov processes," pp. 688–695, IEEE, May 2014.

[32] D. A. S. Mohamed Hamid Elsheikh, S. B. M. S. Mohd Faizul Mohd Sabri, M. B. A. B. Masjuki Haji Hassan, and M. Mohamad, "A review on thermoelectric renewable energy: Principle parameters that affect their performance," *Renewable and Sustainable Energy Reviews*, vol. 30, pp. 337–355, 2014.

[33] J. Chen, *Design and analysis of a thermoelectric energy harvesting system for powering sensing nodes in nuclear power plant*. Master of Science In Mechanical Engineering, Virginia Polytechnic Institute, Blacksburg, VA, Dec. 2015.

[34] L.-D. Z. Xiao Zhang, "Thermoelectric materials: Energy conversion between heat and electricity," *Journal of Materiomics*, vol. 1, no. 2, pp. 92–105, 2015.

[35] B. E F Thacher and C. J. R. M A Karri, "Testing of an automobile exhaust thermoelectric generator in a light truck," *Proc. IMechE, Part D: J. Automobile Engineering*, vol. 221, pp. 95–107, 2007.

[36] X. Y. Weishu Liu and Z. R. Gang Chen, "Recent advances in thermoelectric nanocomposites," *Nano Energy*, vol. 1, no. 1, pp. 42–56, 2012.

[37] H. Kleinke, "New bulk materials for thermoelectric power generation: clathrates and complex antimonides," *Chemistry Materials*, vol. 22, no. 3, pp. 604–611, 2009.

[38] J. T. Jyrki Tervo and H. H. Risto Ilola, "State-of-the-art of thermoelectric materials processing," *VTT Working Papers*, pp. 1–29.

[39] "40-Channel Single-Module ROADM for the Cisco ONS 15454 Multiservice Transport Platform," tech. rep., Cisco.

[40] "Maximizing the Output Power from Thermoelectric Harvesters," Feb. 2014.

[41] W. Xu, *Experimental and Numerical Analysis of Thermoelectric Magnetohydrodynamic Driven Liquid Lithium Flow in Open Channels for Fusion Applications*. 2015. Google-Books-ID: E3g3jwEACAAJ.

[42] Y. K. Ramadass and A. P. Chandrakasan, "A Battery-Less Thermoelectric Energy Harvesting Interface Circuit With 35 mV Startup Voltage," *IEEE Journal of Solid-State Circuits*, vol. 46, pp. 333–341, Jan. 2011.

[43] J. G. Haidar and J. I. Ghojel, "Waste heat recovery from the exhaust of low-power diesel engine using thermoelectric generators," in *Proceedings ICT2001. 20 International Conference on Thermoelectrics (Cat. No.01TH8589)*, pp. 413–418, 2001.

[44] K. Ikoma, M. Munekiyo, K. Furuya, M. Kobayashi, T. Izumi, and K. Shinohara, "Thermoelectric module and generator for gasoline engine vehicles," in *Seventeenth International Conference on Thermoelectrics. Proceedings ICT98 (Cat. No.98TH8365)*, pp. 464–467, May 1998.

[45] R. Dell, R. Unnthorsson, C. S. Wei, G. W. Sidebotham, M. T. Jonsson, W. Foley, E. Ginzburg, S. Paul, S. Kim, and A. Morris, "Thermoelectric-Based Power Generator for Powering Microcontroller Based Security Camera," pp. 635–642, Nov. 2012.

[46] M. Remeli, A. Date, B. Bhathal Singh, L. Tan, and A. Akbarzadeh, "Power generation and heat recovery using heat pipe thermoelectric generator (HPTEG)," pp. 1–9, Australian Solar Council, 2014.

[47] G. J. Snyder, "Small thermoelectric generators," *Electrochemical Society Interface*, vol. 17, pp. 54–56, Sept. 2008.

[48] M. Hirota, Y. Nakajima, M. Saito, and M. Uchiyama, "120 ÃŮ 90 element thermoelectric infrared focal plane array with precisely patterned Au-black absorber," *Sensors and Actuators A: Physical*, vol. 135, pp. 146–151, Mar. 2007.

[49] N. Youn, H. Lee, D. Wee, M. Gomez, R. Reid, and B. Ohara, "Achieving Maximum Power in Thermoelectric Generation with Simple Power Electronics," *Journal of Elec Materi*, vol. 43, pp. 1597–1602, June 2014.

[50] K. Pietrzyk, J. Soares, B. Ohara, and H. Lee, "Power generation modeling for a wearable thermoelectric energy harvester with practical limitations," *Applied Energy*, vol. 183, pp. 218–228, Dec. 2016.

[51] Jennie Jorgenson, Paul Gilman, and Aron Dobos, *Technical Manual for the SAM Biomass Power Generation Model*. National Renewable Energy Laboratory.

[52] A. Dementyev, S. Hodges, S. Taylor, and J. Smith, "Power consumption analysis of Bluetooth Low Energy, ZigBee and ANT sensor nodes in a cyclic sleep scenario," in *2013 IEEE International Wireless Symposium (IWS)*, pp. 1–4, Apr. 2013.

[53] "Waste Heat Recovery Technology Assessment," tech. rep., U.S. Department of Energy, 2015.

[54] BCS Incorporated, "Waste heat recovery: Technology and Opportunities in U.S industry," tech. rep., U.S Department of Energy, March 2008.

[55] Y. Zhou, S. Paul, and S. Bhunia, "Harvesting Wasted Heat in a Microprocessor Using Thermoelectric Generators: Modeling, Analysis and Measurement," in *2008 Design, Automation and Test in Europe*, pp. 98–103, Mar. 2008.

[56] J.-H. Bahk, H. Fang, K. Yazawa, and A. Shakouri, "Flexible thermoelectric materials and device optimization for wearable energy harvesting," *Journal of Materials Chemistry C*, vol. 3, p. 10362, July 2015.

[57] V. Leonov and R. Vullers, "Thermoelectric generators on living beings," *Proceedings - 5th European Conference on Thermoelectrics*, p. 47, Sept. 2007.

[58] G. P. Meisner, "Thermoelectric conversion of exhaust gas waste heat into usable electricity," in *Proc. 2011 Directions in Engine-Efficiency and Emissions Research (DEER) Conference, Detroit, Michigan*, 2011.

[59] T.-M. Jeng, S.-C. Tzeng, B.-J. Yang, and Y.-C. Li, "Design, Manufacture and Performance Test of the Thermoelectric Generator System for Waste Heat Recovery of Engine Exhaust," *Inventions*, vol. 1, p. 2, Jan. 2016.

[60] Y. Wang, C. Dai, and S. Wang, "Theoretical analysis of a thermoelectric generator using exhaust gas of vehicles as heat source," *Applied Energy*, vol. 112, pp. 1171–1180, Dec. 2013.

[61] W. K. Seah, Z. A. Eu, and H.-P. Tan, "Wireless sensor networks powered by ambient energy harvesting (WSN-HEAP) - Survey and challenges," pp. 1–5, IEEE, May 2009.

[62] P. D. Mitcheson, "Vibration Energy Harvesting Basics." NIPS workshop – Imperial College London, 2014.

[63] A. Erturk and D. Inman, "Broadband piezoelectric power generation on high-energy orbits of the bistable Duffing oscillator with electromechanical coupling," *Journal of Sound and Vibration*, vol. 330, pp. 2339–2353, May 2011.

[64] "Cerametrics." http://www.advancedcerametrics.com.

[65] "Ambiosystems." http://www.ambiosystems.com.

[66] "Microstrain." http://www.microstrain.com.

[67] "EnOcean." http://www.enocean.com.

[68] REI, "nPower PEG Personal Energy Generator – REI.com." https://www.rei.com/product/849998/npower-peg-personal-energy-generator.

[69] L. Wang and F. G. Yuan, "Vibration energy harvesting by magnetostrictive material," *Smart Mater. Struct.*, vol. 17, no. 4, p. 045009, 2008.

[70] F. Cottone, "Introduction to Vibration Energy Harvesting," NiPS Energy Harvesting Summer School, Aug. 2011.

[71] M.-L. Ku, W. Li, Y. Chen, and K. R. Liu, "Advances in energy harvesting communications: Past, present, and future challenges," *IEEE Communications Surveys & Tutorials*, vol. 18, no. 2, pp. 1384–1412, 2016.

[72] S. Kundu and H. B. Nemade, "Modeling and Simulation of a Piezoelectric Vibration Energy Harvester," *Procedia Engineering*, vol. 144, pp. 568–575, Jan. 2016.

[73] E. Hau and H. Von Renouard, *The wind resource*. Springer, 2006.

[74] "Sea breeze." https://en.wikipedia.org/w/index.php?title=Sea_breeze&oldid=809341167, Nov. 2017.

[75] Governor's School for Agriculture, "What's Up With Wind Turbines?." https://govschoolagriculture.com/2015/07/24/whats-up-with-wind-turbines/, July 2015.

[76] T. Burton, N. Jenkins, D. Sharpe, and E. Bossanyi, *Wind Energy Handbook*. John Wiley & Sons, May 2011. Google-Books-ID: dip2LwCRCscC.

[77] A. Betz, . Grissmer, David W. (David Waltz), J. S. Morse, R. A. United States. Office of the Assistant Secretary of Defense (Manpower, and Logistics), *Introduction to the theory of flow machines*. Oxford : Pergamon Press, [1st english ed.] ed., 1966.

[78] M. Islam, D. S. K. Ting, and A. Fartaj, "Aerodynamic models for Darrieus-type straight-bladed vertical axis wind turbines," *Renewable and Sustainable Energy Reviews*, vol. 12, pp. 1087–1109, May 2008.

[79] T. Petru and T. Thiringer, "Modeling of wind turbines for power system studies," *IEEE Transactions on Power Systems*, vol. 17, pp. 1132–1139, Nov. 2002.

[80] J. G. Slootweg, S. W. H. d. Haan, H. Polinder, and W. L. Kling, "General model for representing variable speed wind turbines in power system dynamics simulations," *IEEE Transactions on Power Systems*, vol. 18, pp. 144–151, Feb. 2003.

[81] R. Karki and R. Billinton, "Cost-effective wind energy utilization for reliable power supply," *IEEE Transactions on Energy Conversion*, vol. 19, pp. 435–440, June 2004.

[82] S. Li, D. C. Wunsch, E. A. O'Hair, and M. G. Giesselmann, "Using neural networks to estimate wind turbine power generation," *IEEE Transactions on Energy Conversion*, vol. 16, pp. 276–282, Sept. 2001.

[83] B. Zhu, M.-y. Chen, N. Wade, and L. Ran, "A prediction model for wind farm power generation based on fuzzy modeling," *Procedia Environmental Sciences*, vol. 12, pp. 122–129, Jan. 2012.

[84] C. Morlaas, M. Fares, and B. Souny, "Wind turbine effects on VOR system performance," *IEEE Transactions on Aerospace and Electronic Systems*, vol. 44, pp. 1464–1476, Oct. 2008.

[85] D. L. Sengupta and T. B. A. Senior, *Electromagnetic Interference from Wind Turbines*. ASME Press, 2009.

[86] C. R. Valenta and G. D. Durgin, "Harvesting Wireless Power: Survey of Energy-Harvester Conversion Efficiency in Far-Field, Wireless Power Transfer Systems," *IEEE Microwave Magazine*, vol. 15, pp. 108–120, June 2014.

[87] M. M. Anshoo Tandon and L. R. Varshney, "Real-time simultaneous energy and information transfer," (Hong Kong), June 2015.

[88] T. Perera, D. Jayakody, S. De, and M. A. Ivanov, "A survey on simultaneous wireless information and power transfer," vol. 803, no. 1, p. 012113, 2017.

[89] I. Flint, X. Lu, N. Privault, D. Niyato, and P. Wang, "Performance analysis of ambient rf energy harvesting with repulsive point process modeling," *IEEE Transactions on Wireless Communications*, vol. 14, no. 10, pp. 5402–5416, 2015.

[90] A. Dekka, R. Ghaffari, B. Venkatesh, and B. Wu, "A survey on energy storage technologies in power systems," in *2015 IEEE Electrical Power and Energy Conference (EPEC)*, pp. 105–111, Oct. 2015.

[91] RWE Power AG, "Adele – adiabatic compressed-air energy storage for electricity supply," 2010.

[92] E. Jannelli, M. Minutillo, A. Lubrano Lavadera, and G. Falcucci, "A small-scale CAES (compressed air energy storage) system for stand-alone renewable energy power plant for a radio base station: A sizing-design methodology," *Energy*, vol. 78, pp. 313–322, Dec. 2014.

[93] "Environmental Engineering (EE); The use of alternative energy solutions in telecommunication installations – ETSI TR 102.532," tech. rep., European Telecommunications Standards Institute.

[94] B. Bolund, H. Bernhoff, and M. Leijon, "Flywheel energy and power storage systems," *Renewable and Sustainable Energy Reviews*, vol. 11, no. 2, pp. 235–258, 2007.

[95] C.-T. Pham and D. Månsson, "On the physical system modelling of energy storages as equivalent circuits with parameter description for variable load demand (part i)," *Journal of Energy Storage*, vol. 13, pp. 73–84, 2017.

[96] K. L. Hrishikesh Jayakumar, A. R. Woo Suk Lee, and V. R. Younghyun Kim, "Powering the Internet of Things," *Proceedings of the 2014 international symposium on Low power electronics and design*, pp. 375–380, 2014.

[97] E. M. Yeatman, "Advances in Power Sources for Wireless Sensor Nodes," in *1st International Workshop on Body Sensor Networks*, (London), pp. 6–7, 2004.

[98] D. Porcarelli, D. Brunelli, and L. Benini, "Characterization of lithium-ion capacitors for low-power energy neutral wireless sensor networks," in *2012 Ninth International Conference on Networked Sensing (INSS)*, pp. 1–4, June 2012.

[99] D. S. Shad Roundy, P. W. Luc Frechette, and J. Rabaey, "Power Sources for Wireless Sensor Networks," vol. 2920, (Berlin, Heidelberg), pp. 1–17. Lecture Notes in Computer Science.

[100] "Comparison of commercial battery types." https://en.wikipedia.org/wiki/Comparison_of_commercial_battery_types#cite_note-AAB4-12, 2017.

[101] A. B. Guillaume Girardin and E. Mounier, "Technologies & Sensors for the Internet of Things. Businesses & Market Trends 2014–2024," MEMS Report, Yole Developpement, 2014.

[102] W. Rowe, "IoT battery outlook: Types of batteries for IoT devices,"

[103] RECHARGE aisbl, "Safety of lithium-ion batteries," tech. rep., The European Association for Advanced Rechargeable Batteries, Brussels. Belgium., 2013.

[104] N. W. Toby Litovitz, N. C. W. Lynn Clark, and M. Marsolek, "Emerging Battery-Ingestion Hazard:Clinical Implications," *Pediatrics*, vol. 125, no. 6, pp. 1168–1177, 2010.

[105] A. Somov and R. Giaffreda, "Powering iot devices: Technologies and opportunities," *Newsletter*, vol. 2014, 2014.

[106] A. Cultura II and Z. Salameh, "Modeling, evaluation and simulation of a supercapacitor module for energy storage application," *cell*, vol. 1, p. 1, 2015.

[107] D. Sutanto and K. Cheng, "Superconducting magnetic energy storage systems for power system applications," in *Applied Superconductivity and Electromagnetic Devices, 2009. ASEMD 2009. International Conference on*, pp. 377–380, IEEE, 2009.

[108] E. Salih, S. Lachowicz, O. Bass, and D. Habibi, "Superconducting Magnetic Energy Storage Unit for Damping Enhancement of a Wind Farm Generation System," 2015.

[109] N. A. Thong, *Application of Supercapacitor in Elecrical Energy Storage*. PhD thesis, 2011.

[110] D. Connolly, "A review of energy storage technologies: for the integration of fluctuating renewable energy," *University of Limerick*, 2010.

[111] Y. Parvini, A. Vahidi, and S. A. Fayazi, "Heuristic Versus Optimal Charging of Supercapacitors, Lithium-Ion, and Lead-Acid Batteries: An Efficiency Point of View," *IEEE Transactions on Control Systems Technology*, vol. PP, no. 99, pp. 1–14, 2017.

[112] "Nickel Cadmium Batteries Technical Handbook," tech. rep., Panasonic Batteries, 1999.

[113] "Nickel Cadmium Batteries Technical Handbook," tech. rep., GP Batteries, 2003.

[114] S. Sudevalayam and P. Kulkarni, "Energy Harvesting Sensor Nodes: Survey and Implications," *IEEE Communications Surveys & Tutorials*, vol. 13, no. 3, pp. 443–461, 2011.

[115] Battery University, "Nickel Based Batteries." http://batteryuniversity.com/learn/article/nickel_based_batteries, May 2016.

[116] V. Raghunathan, A. Kansal, J. Hsu, J. Friedman, and M. Srivastava, "Design considerations for solar energy harvesting wireless embedded systems," pp. 457–462, IEEE, 2005.

[117] K. Lahiri, A. Raghunathan, S. Dey, and D. Panigrahi, "Battery-driven system design: a new frontier in low power design," pp. 261–267, IEEE Comput. Soc, 2002.

[118] M. García-Plaza, D. Serrano-Jiménez, J. Eloy-García Carrasco, and J. Alonso-Martínez, "A Ni-Cd battery model considering state of charge and hysteresis effects," *Journal of Power Sources*, vol. 275, pp. 595–604, Feb. 2015.

[119] "Nickel Metal Hydride (NiMH) Handbook and Application Manual," tech. rep., Energizer, 2010.

[120] "Nickel Metal Hydride Handbook," tech. rep., Panasonic Batteries, 2003.

[121] "Charging Nickel-Metal Hydride Batteries," tech. rep., Atmel, 2007.

[122] Johnson Matthey Battery Systems, "Nickel Metal Hydride (NiMH)." http://www.jmbatterysystems.com/technology/cells/nickel-metal-hydride-(nimh).

[123] P. Notten and D. Danilov, "Battery modeling: A versatile tool to design advanced battery management systems," vol. 4, pp. 62–72, 01 2014.

[124] "Lithium-ion Batteries," tech. rep., Panasonic Batteries, 2007.

[125] Johnson Matthey Battery Systems, "Lithium-ion cells." http://www.jmbatterysystems.com/technology/cells/lithium-ion-cells.

[126] Battery University, "Lithium-ion Batteries." http://batteryuniversity.com/learn/article/lithium_based_batteries, 2017.

[127] Wind&Sun, "Lithium-ion Batteries." http://www.windandsun.co.uk/products/Batteries/Lithium-Ion-Batteries#.WPuo6aIlFPY.

[128] A. Rahmoun and H. Biechl, "Modelling of li-ion batteries using equivalent circuit diagrams," vol. 88, pp. 152–156, 01 2012.

[129] Matworks, "Battery." https://uk.mathworks.com/help/physmod/sps/powersys/ref/battery.html.

[130] O. Tremblay and L.-A. Dessaint, "Experimental validation of a battery dynamic model for EV applications," *World Electric Vehicle Journal*, vol. 3, no. 1, pp. 1–10, 2009.

[131] Z. F. Hussien, W. C. Lee, M. F. Siam, and A. B. Ismail, "Modeling of sodium sulfur battery for power system applications," *Elektrika Journal of Electrical Engineering*, vol. 9, no. 2, pp. 66–72, 2007.

[132] M. Musio and A. Damiano, "A non-linear dynamic electrical model of sodium-nickel chloride batteries," in *Renewable Energy Research and Applications (ICRERA), 2015 International Conference on*, pp. 872–878, IEEE, 2015.

[133] H. Zhang and M.-Y. Chow, "Comprehensive dynamic battery modeling for phev applications," in *Power and Energy Society General Meeting, 2010 IEEE*, pp. 1–6, IEEE, 2010.

[134] F. Chamran, H.-S. Min, B. Dunn, and C.-J. Kim, "Three-dimensional nickel-zinc microbatteries," in *19th IEEE International Conference on Micro Electro Mechanical Systems*, pp. 950–953, 2006.

[135] J. Bates, N. Dudney, B. Neudecker, A. Ueda, and C. Evans, "Thin-film lithium and lithium-ion batteries," *Solid State Ionics*, vol. 135, no. 1, pp. 33–45, 2000.

[136] R. W. Hart, H. S. White, B. Dunn, and D. R. Rolison, "3-d microbatteries," *Electrochemistry Communications*, vol. 5, no. 2, pp. 120–123, 2003.

[137] M. Roberts, P. Johns, J. Owen, D. Brandell, K. Edstrom, G. E. Enany, C. Guery, D. Golodnitsky, M. Lacey, C. Lecoeur, H. Mazor, E. Peled, E. Perre, M. M. Shaijumon, P. Simon, and P.-L. Taberna, "3d lithium ion batteries from fundamentals to fabrication," *J. Mater. Chem.*, vol. 21, pp. 9876–9890, June 2011.

[138] V. Zadin, D. Brandell, H. Kasemägi, J. Lellep, and A. Aabloo, "Designing the 3d-microbattery geometry using the level-set method," *Journal of Power Sources*, vol. 244, pp. 417–428, Dec. 2013.

[139] L. T., P. Giman, and P. Lilienthal, "Micropower System Modeling with HOMER," tech. rep.

[140] L. W. Weiss, "Resonant operation and cycle work from a MEMS-based micro-heat engine," *Microsyst Technol*, vol. 15, pp. 485–492, Mar. 2009.

[141] D. P. Scamman, G. W. Reade, and E. P. Roberts, "Numerical modelling of a bromide-polysulphide redox flow battery: Part 1: Modelling approach and validation for a pilot-scale system," *Journal of Power Sources*, vol. 189, no. 2, pp. 1220–1230, 2009.

[142] D. You, H. Zhang, and J. Chen, "A simple model for the vanadium redox battery," *Electrochimica Acta*, vol. 54, no. 27, pp. 6827–6836, 2009.

[143] M. Vynnycky, "Analysis of a model for the operation of a vanadium redox battery," *Energy*, vol. 36, no. 4, pp. 2242–2256, 2011.

[144] X. Zhou, T. Zhao, L. An, Y. Zeng, and X. Yan, "A vanadium redox flow battery model incorporating the effect of ion concentrations on ion mobility," *Applied Energy*, vol. 158, pp. 157–166, 2015.

[145] A. Kundu, J. Jang, J. Gil, C. Jung, H. Lee, S.-H. Kim, B. Ku, and Y. Oh, "Micro-fuel cells - current development and applications," *Journal of Power Sources*, vol. 170, no. 1, pp. 67–78, 2007.

[146] S. A. Jacobson and A. H. Epstein, "An informal survey of power MEMS :," *International Symposium on Micro-Mechanical Engineering : ISMME*, vol. 2003, pp. 513–520, 2003.

[147] K. Khu, L. Jiang, and T. Markvart, "Effect of finite heat input on the power performance of micro heat engines," *Energy*, vol. 36, pp. 2686–2692, May 2011.

[148] S. Whalen, M. Thompson, D. Bahr, C. Richards, and R. Richards, "Design, fabrication and testing of the P3 micro heat engine," *Sensors and Actuators A: Physical*, vol. 104, pp. 290–298, May 2003.

[149] K. Khu, L. Jiang, and T. Markvart, "Effect of finite heat input on the power performance of micro heat engines," *Energy*, vol. 36, pp. 2686–2692, May 2011.

[150] T. Huesgen, J. Ruhhammer, G. Biancuzzi, and P. Woias, "Detailed study of a micro heat engine for thermal energy harvesting," *J. Micromech. Microeng.*, vol. 20, no. 10, p. 104004, 2010.

[151] H. K. Bardaweel, M. J. Anderson, R. F. Richards, and C. D. Richards, "Optimization of the dynamic and thermal performance of a resonant micro heat engine," *J. Micromech. Microeng.*, vol. 18, no. 10, p. 104014, 2008.

[152] G. Auer, O. Blume, V. Giannini, I. G. ETH, M. A. Imran, Y. J. EAB, E. Katranaras, M. O. EAB, D. S. TI, P. S. EAB, and others, "INFSO-ICT-247733 EARTH,"

[153] C. Desset, B. Debaillie, V. Giannini, A. Fehske, G. Auer, H. Holtkamp, W. Wajda, D. Sabella, F. Richter, M. J. Gonzalez, and others, "Flexible power modeling of LTE base stations," in *Wireless Communications and Networking Conference (WCNC), 2012 IEEE*, pp. 2858–2862, IEEE, 2012.

[154] G. Auer, V. Giannini, C. Desset, I. Godor, P. Skillermark, M. Olsson, M. Imran, D. Sabella, M. Gonzalez, O. Blume, and A. Fehske, "How much energy is needed to run a wireless network?," *IEEE Wireless Communications*, vol. 18, pp. 40–49, Oct. 2011.

[155] e. a. Auer, Gunther, "D2.3: Energy efficiency analysis of the reference systems, areas of improvements and target breakdown.," 2010.

[156] R. Pothan, "Powering Cellular Base Stations – A Quantitative Analysis of Energy Options Solar PV, Diesel Generators, Batteries and Electrical Grid," Oct. 2012.

[157] G. Schmitt, "The Green Base Station," in *4th International Telecommunication - Energy special conference*, pp. 1–6, May 2009.

[158] K. Samdanis, P. Rost, A. Maeder, M. Meo, and C. Verikoukis, *Green Communications: Principles, Concepts and Practice*. John Wiley & Sons, 2015.

[159] O. Arnold, F. Richter, G. Fettweis, and O. Blume, "Power consumption modeling of different base station types in heterogeneous cellular networks," in *2010 Future Network Mobile Summit*, pp. 1–8, June 2010.

[160] M. Deruyck, W. Joseph, and L. Martens, "Power consumption model for macrocell and microcell base stations," *TRANSACTIONS ON EMERGING TELECOMMUNICATIONS TECHNOLOGIES*, vol. 25, no. 3, pp. 320–333, 2014.

[161] K. Liu, J. He, J. Ding, Y. Zhu, and Z. Liu, "Base station power model and application for energy efficient LTE," in *Communication Technology (ICCT), 2013 15th IEEE International Conference on*, pp. 86–92, IEEE, 2013.

[162] B. H. Jung, H. Leem, and D. K. Sung, "Modeling of power consumption for macro-, micro-, and RRH-based base station architectures," in *Vehicular Technology Conference (VTC Spring), 2014 IEEE 79th*, pp. 1–5, IEEE, 2014.

[163] J. Lorincz, T. Garma, and G. Petrovic, "Measurements and Modelling of Base Station Power Consumption under Real Traffic Loads," *Sensors*, vol. 12, pp. 4281–4310, Mar. 2012.

[164] S. Tombaz, P. Monti, F. Farias, M. Fiorani, L. Wosinska, and J. Zander, "Is backhaul becoming a bottleneck for green wireless access networks?," pp. 4029–4035, IEEE, 2014.

[165] P. Monti, S. Tombaz, L. Wosinska, and J. Zander, "Mobile backhaul in heterogeneous network deployments: Technology options and power consumption," in *2012 14th International Conference on Transparent Optical Networks (ICTON)*, pp. 1–7, July 2012.

[166] L. Suárez, M. A. Bouraoui, M. A. Mertah, M. Morvan, and L. Nuaymi, "Energy efficiency and cost issues in backhaul architectures for high data-rate green mobile heterogeneous networks," in *2015 IEEE 26th Annual International Symposium on Personal, Indoor, and Mobile Radio Communications (PIMRC)*, pp. 1563–1568, Aug. 2015.

[167] S. Sesia, M. Baker, and I. Toufik, *LTE-the UMTS long term evolution: from theory to practice*. John Wiley & Sons, 2011.

[168] T. Restorick, "An inefficient truth," *Global Action Plan Report*, vol. 1, 2007.

[169] W. Vereecken, L. Deboosere, D. Colle, B. Vermeulen, M. Pickavet, B. Dhoedt, and P. Demeester, "Energy efficiency in telecommunication networks," in *Proceedings of NOC2008, the 13th European Conference on Networks and Optical Communications*, pp. 44–51, 2008.

[170] J. Baliga, R. Ayre, K. Hinton, W. V. Sorin, and R. S. Tucker, "Energy Consumption in Optical IP Networks," *J. Lightwave Technol., JLT*, vol. 27, pp. 2391–2403, July 2009.

[171] J. Koomey, H. Chong, W. Loh, B. Nordman, and M. Blazek, "Network electricity use associated with wireless personal digital assistants," *Journal of infrastructure systems*, vol. 10, no. 3, pp. 131–137, 2004.

[172] M. Patel, B. Naughton, C. Chan, N. Sprecher, S. Abeta, A. Neal, and others, "Mobile-edge computing introductory technical white paper," *White Paper, Mobile-edge Computing (MEC) industry initiative*, 2014.

[173] K. M. S. Huq, S. Mumtaz, J. Bachmatiuk, J. Rodriguez, X. Wang, and R. L. Aguiar, "Green HetNet CoMP: Energy efficiency analysis and optimization," *IEEE Transactions on Vehicular Technology*, vol. 64, no. 10, pp. 4670–4683, 2015.

[174] K. Le, R. Bianchini, T. D. Nguyen, O. Bilgir, and M. Martonosi, "Capping the brown energy consumption of Internet services at low cost," in *International Conference on Green Computing*, pp. 3–14, Aug. 2010.

[175] J. Xu and S. Ren, "Online Learning for Offloading and Autoscaling in Renewable-Powered Mobile Edge Computing," in *2016 IEEE Global Communications Conference (GLOBECOM)*, pp. 1–6, Dec. 2016.

[176] A. Beloglazov, J. Abawajy, and R. Buyya, "Energy-aware resource allocation heuristics for efficient management of data centers for cloud computing," *Future generation computer systems*, vol. 28, no. 5, pp. 755–768, 2012.

[177] A. Kansal, F. Zhao, J. Liu, N. Kothari, and A. A. Bhattacharya, "Virtual machine power metering and provisioning," in *Proceedings of the 1st ACM symposium on Cloud computing*, pp. 39–50, ACM, 2010.

[178] Y. Bao, M. Chen, Y. Ruan, L. Liu, J. Fan, Q. Yuan, B. Song, and J. Xu, "HMTT: a platform independent full-system memory trace monitoring system," *ACM SIGMETRICS Performance Evaluation Review*, vol. 36, no. 1, pp. 229–240, 2008.

[179] H. Zeng, C. S. Ellis, A. R. Lebeck, and A. Vahdat, "ECOSystem: Managing energy as a first class operating system resource," in *ACM Sigplan Notices*, vol. 37, pp. 123–132, ACM, 2002.

[180] "Third Quarter 2017 SPEC SPECpower_ssj2008 Results." https://www.spec.org/power_ssj2008/results/res2017q3/, 2017.

[181] A. Caroll and G. Heiser, "An Analysis of Power Consumption in a Smartphone," *Proceeding USENIXATC'10 Proceedings of the 2010 USENIX conference on USENIX annual technical conference*, June 2010.

[182] L. Wang, A. Ukhanova, and E. Belyaev, "Power consumption analysis of constant bit rate data transmission over 3g mobile wireless networks," in *2011 11th International Conference on ITS Telecommunications*, pp. 217–223, Aug. 2011.

[183] E. Harjula, O. Kassinen, and M. Ylianttila, "Energy consumption model for mobile devices in 3g and WLAN networks," pp. 532–537, IEEE, Jan. 2012.

[184] A. R. Jensen, M. Lauridsen, P. Mogensen, T. B. Sørensen, and P. Jensen, "LTE UE Power Consumption Model: For System Level Energy and Performance Optimization," pp. 1–5, IEEE, Sept. 2012.

[185] B. Dusza, C. Ide, L. Cheng, and C. Wietfeld, "An accurate measurement-based power consumption model for LTE uplink transmissions," pp. 49–50, IEEE, Apr. 2013.

[186] N. Balasubramanian, A. Balasubramanian, and A. Venkataramani, "Energy consumption in mobile phones: a measurement study and implications for network applications," p. 280, ACM Press, 2009.

[187] J. Gubbi, R. Buyya, S. Marusic, and M. Palaniswami, "Internet of Things (IoT): A Vision, Architectural Elements, and Future Directions," *arXiv:1207.0203 [cs]*, July 2012. arXiv: 1207.0203.

[188] I. F. Akyildiz, W. Su, Y. Sankarasubramaniam, and E. Cayirci, "Wireless sensor networks: a survey," *Computer Networks*, vol. 38, pp. 393–422, 2002.

[189] M. A. M. Vieira, C. N. Coelho, D. C. d. Silva, and J. M. d. Mata, "Survey on wireless sensor network devices," in *EFTA 2003. 2003 IEEE Conference on Emerging Technologies and Factory Automation. Proceedings (Cat. No.03TH8696)*, vol. 1, pp. 537–544 vol.1, Sept. 2003.

[190] V. Potdar, A. Sharif, and E. Chang, "Wireless Sensor Networks: A Survey," in *2009 International Conference on Advanced Information Networking and Applications Workshops*, pp. 636–641, May 2009.

[191] L. Atzori, A. Iera, and G. Morabito, "The Internet of Things: A Survey," *Comput. Netw.*, vol. 54, pp. 2787–2805, Oct. 2010.

[192] A. Al-Fuqaha, M. Guizani, M. Mohammadi, M. Aledhari, and M. Ayyash, "Internet of Things: A Survey on Enabling Technologies, Protocols, and Applications," *IEEE Communications Surveys Tutorials*, vol. 17, no. 4, pp. 2347–2376, 2015.

[193] Z. Pei, Z. Deng, B. Yang, and X. Cheng, "Application-oriented wireless sensor network communication protocols and hardware platforms: A survey," in *2008 IEEE International Conference on Industrial Technology*, pp. 1–6, Apr. 2008.

[194] M. Healy, T. Newe, and E. Lewis, "Wireless Sensor Node hardware: A review," in *2008 IEEE Sensors*, pp. 621–624, Oct. 2008.

[195] S. D. T. Kelly, N. K. Suryadevara, and S. C. Mukhopadhyay, "Towards the Implementation of IoT for Environmental Condition Monitoring in Homes," *IEEE Sensors Journal*, vol. 13, pp. 3846–3853, Oct. 2013.

[196] P. Kamalinejad, C. Mahapatra, Z. Sheng, S. Mirabbasi, V. C. M. Leung, and Y. L. Guan, "Wireless energy harvesting for the Internet of Things," *IEEE Communications Magazine*, vol. 53, pp. 102–108, June 2015.

[197] Y. H. Chee, J. Rabaey, and A. M. Niknejad, "A class A/B low power amplifier for wireless sensor networks," in *2004 IEEE International Symposium on Circuits and Systems (IEEE Cat. No.04CH37512)*, vol. 4, pp. IV–409–12 Vol.4, May 2004.

[198] V. K. Sachan, S. A. Imam, and M. T. Beg, "Energy-Efficient Communication Methods in Wireless Sensor Networks: A Critical Review," *International Journal of Computer Applications*, vol. 39, Feb. 2012.

[199] A. Bonnabel and G. Girardin, "Technologies & Sensors for the Internet of Things: Businesses & Market Trends 2014-2024," tech. rep., YOLE Developpement.

[200] B. Martinez, M. Monton, I. Vilajosana, and X. Vilajosana, "Early Scavenger Dimensioning in Wireless Industrial Monitoring Applications," vol. 3, pp. 170–178, Apr. 2016.

[201] B. Martinez, X. Vilajosana, F. Chraim, I. Vilajosana, and K. S. J. Pister, "When Scavengers Meet Industrial Wireless," *IEEE Transactions on Industrial Electronics*, vol. 62, pp. 2994–3003, May 2015.

[202] M. Mahmoud and A. Mohamad, "A study of efficient power consumption wireless communication techniques/ modules for internet of things (iot) applications," vol. 06, pp. 19–29, 01 2016.

[203] F. Mahmood, E. Perrins, and L. Liu, "Modeling and Analysis of Energy Consumption for RF Transceivers in Wireless Cellular Systems." Dec. 2015.

[204] W. T. L.A.Da Silva and G. Jacquemod, "Hierarchical modelling of a 2.4-GHz power amplifier for energy consumption analysis at system level," *2009 Ph.D. Research in Microelectronics and Electronics*, July 2009.

[205] H.-Y. Zhou, D.-Y. Luo, Y. Gao, and D.-C. Zuo, "Modeling of Node Energy Consumption for Wireless Sensor Networks," *Wireless Sensor Network*, vol. 03, p. 18, Jan. 2011.

[206] M. M. B. Martinez and J. P. I. Vilajosana, "The Power of Models: Modeling Power Consumption for IoT Devices," *IEEE Sensors Journal*, vol. 15, Oct. 2015.

[207] Q. Wang, M. Hempstead, and W. Yang, "A Realistic Power Consumption Model for Wireless Sensor Network Devices," vol. 1, pp. 286–295, Sept. 2006.

[208] B. Martinez, M. Monton, I. Vilajosana, and J. D. Prades, "The Power of Models: Modeling Power Consumption for IoT Devices," *IEEE Sensors Journal*, vol. 15, pp. 5777–5789, Oct. 2015.

[209] E. Gindullina and L. Badia, "Towards self-control of service rate for battery management in energy harvesting devices," in *2017 IEEE International Conference on Communications Workshops (ICC Workshops)*, pp. 355–360, May 2017.

[210] N. Piovesan and P. Dini, "Optimal direct load control of renewable powered small cells: A shortest path approach," *Internet Technology Letters*, pp. n/a–n/a, 2017.

[211] L. Badia, E. Feltre, and E. Gindullina, "A Markov Model Accounting for Charge Recovery in Energy Harvesting Devices," in *2017 IEEE Wireless Communications and Networking Conference Workshops (WCNCW)*, pp. 1–6, Mar. 2017.

[212] I. Fawaz, P. Ciblat, and M. Sarkiss, "Energy minimization based Resource Scheduling for Strict Delay Constrained Wireless Communications,"

www.scavenge.eu